MODELING OF HIGH-SPEED MACHINE-TOOL SPINDLE SYSTEMS

by

YUZHONG CAO

B.Sc., Taiyuan University of Technology

M.A.Sc., Harbin Institute of Technology

A THESIS SUBMITTED IN PARTIAL FULFILLMENT OF

THE REQUIREMENTS FOR THE DEGREE OF

DOCTOR OF PHILOSOPHY

in

THE FACULTY OF GRADUATE STUDIES

(Mechanical Engineering)

THE UNIVERSITY OF BRITISH COLUMBIA

March 2006

Abstract

The successful application of high-speed machining technology is highly dependent on spindles operating free of chatter vibration without overloading the angular contact ball bearings. Unless avoided, vibration instability in the metal-cutting process leads to premature failure of the spindles, which have small shafts and bearing diameters and rotate at high speeds.

This thesis presents a general structural model of the machine-tool spindle assembly, consisting of the rotating shaft, tool holder, angular contact ball bearings, stationary housing, and the machine-tool mounting. The model enables performance testing and analysis of the spindles by specifying cutting conditions, tool geometry, and the work-piece material in a virtual machining environment that avoids the present, costly trial design and prototyping of the spindles.

A generalized finite element (FE) model of the spindle system is developed using Timeshenko's beam theory. The effects of bearing preload, axial cutting forces, gyroscopic and centrifugal forces are considered in the formulation. Bearing stiffness, which varies as a function of the preload, cutting force, and spindle speed, is the fundamental nonlinearity in the dynamics of high-speed spindles. A nonlinear finite element model of the angular contact ball bearing is formulated by considering both centrifugal forces and gyroscopic moments from the rolling elements of the bearing. The elastic deformation of the shaft, rolling elements, housing, and the inner and outer races of the bearings are considered in the bearing model.

The proposed model predicts stiffness changes in the bearing as a function of axial preloads. The model is experimentally verified on an instrumented spindle by comparing the predicted and measured static displacements in axial direction at the spindle nose as the preload is varied.

The general model of the spindle predicts the mode shapes, frequency response function (FRF), vibrations along the spindle shaft, and contact loads on the bearings, which are essential for assessing the performance of the spindle during high-speed machining. While the spindle dynamics is considered to be approximately linear at rest because of the constant

preload of the bearing, it becomes nonlinear in machining due to the dependency of the bearing stiffness on cutting forces and spindle speeds. The linear dynamic model is experimentally verified with impact modal tests on a spindle in free-free boundary conditions. The nonlinear model is verified by comparing the measured impact response of the spindle against predicted displacements under different preloads, which constitutes the fundamental nonlinearity in the spindles. It is shown that high preloads increase the bearing stiffness and the natural frequencies of the spindle system. However, excessive preloads also decrease modal damping, causing reduced dynamic stiffness of the spindles, which is not desirable in avoiding chatter vibrations.

Chatter vibration can be avoided either by having high dynamic stiffness on all structural modes, or by creating a stability pocket at a desired spindle speed where the tooth-passing frequency resonates the mode, thereby allowing large depths of cut. An optimization method, which identifies the most optimal bearing spacing along the spindle shaft, is presented by using either the dynamic stiffness or chatter-free depth of cut at a desired speed range as the objective. The number of teeth on the cutter and the influence of the work-piece material properties are considered in optimizing the bearing locations.

This thesis demonstrates that the dynamics of machine-tool structures may significantly affect the overall structural dynamics of spindle systems. A method of identifying the dynamics of the machine tool without the spindle is presented, and it is incorporated into the spindle model, which allows the simulation of the spindle systems under working conditions.

The proposed numerical model allows designers to optimize spindles and test the performance of the spindles in a virtual metal-cutting environment before they are manufactured. The static and dynamic deflections along the cutter and spindle shaft, as well as contact forces on the bearings, can be predicted with simulated cutting forces before physically building and testing the spindles. The proposed mathematical models are experimentally proven on a research spindle instrumented with non-contact displacement sensors along its shaft. The virtual testing of a complete, industrial-sized spindle is shown to agree well with the experimental results of the same spindle tested in actual metal-cutting operations.

Table of Contents

List of Tables

List of Figures

List of Nomenclature

$A =$ cross sectional area of the beam

$a =$ inner radius of the disk

$a_{C\lim} =$ critical depth of cut

$B =$ $f_o + f_i - 1$

$b =$ outer radius of the disk

$D =$ diameter of the bearing ball

$D_i =$ inner diameter of the beam

$D_m =$ pitch diameter of the bearing measured from the ball center

$D_o =$ outer diameter of the beam

$E =$ Young's modulus of material

$e =$ distance between mass center and the geometrical center of the disk

$E_a =$ Young's modulus of the bearing ball

$E_b =$ Young's modulus of inner or outer ring of the bearing

$F_c =$ centrifugal force

$f_i =$ $\frac{r_i}{D}$

$f_o =$ $\frac{r_o}{D}$

f_{ob} Objective function of optimization

$G =$ shear modulus of material

$I =$ diametral moment of inertia for the beam

I_D = diametral moment of inertia for the disk

J = polar moments of inertia for the beam

J_b = mass moment of inertia for the bearing ball

J_D = polar moment of inertia for the disk

k = index of bearing balls

$K_{d,i}$ dynamic stiffness for the i^{th} mode

K_i, K_o = contact constants between bearing balls and inner rings, outer rings, respectively, depending on the geometry and the material of the bearing balls and bearing rings

K_{tc} = cutting coefficient

k_s = transverse shear form factor, k_s is 0.9 for the circular cross-section beam

M_g = gyroscopic moment

m_D = mass of the disk

m_y, m_z = distributed moments per unit length about axes y and z, respectively

N = number of bearing balls for each bearing

N_t = number of flutes of the cutter

$\mathbf{P}$ = mode shape matrix

P_a axial force in the beam

Q_i = Inner-ring contact force

Q_o = Outer-ring contact force

q_x, q_y, q_z = distributed loads per unit length in the directions x, y and z,

respectively

R = radius of the cross-section of the beam

r = radius of the point P on disk

r_i, r_o = radii of the inner and outer ring grooves, respectively

t = thickness of the disc or time

u, v, w = translational displacements in directions x, y and z, respectively

W_i = weight function

$\mathbf{x}_k$ = current design variable vector

$\mathbf{x}_{k+1}$ = new design variable vector

α_k = angle between the vector of the bearing ball's angular velocity about its own center and shaft axis

$\boldsymbol{\delta}^{(1)}, \boldsymbol{\delta}^{(2)}, \boldsymbol{\delta}^{(3)}, \boldsymbol{\delta}^{(4)}$ = deformation vectors for the node on the spindle shaft, inner ring, outer ring, and the spindle housing, respectively

δ_{ik}, δ_{ok} = normal contact deformations between the centers of the ball and inner ring, and the ball and outer ring, respectively

$\delta_x^i, \delta_y^i, \delta_z^i, \gamma_y^i, \gamma_z^i$ = displacements of the inner ring

$\delta_x^o, \delta_y^o, \delta_z^o, \gamma_y^o, \gamma_z^o$ = displacements of the outer ring

γ_y, γ_z = Shear deformation due to the shear force in the beam cross-section.

$$\varphi_k = \frac{2\pi k}{N}$$

$$\lambda = \frac{D}{D_m}$$

μ_a = Poisson's ratio of the bearing ball

μ_b = Poisson's ratio of inner or outer ring of the bearing

ζ_i modal damping ratio for the i^{th} mode

Ω = rotational speed of the shaft

Ω_E = orbital speed of the bearing ball

Ω_B = angular speed of the bearing ball about its own center

$\omega_{n,i}$ = Natural frequency of the i^{th} mode

ρ = density of material

θ_{ik}, θ_{ok} = inner and outer ring contact angles of the bearing

θ_y, θ_z = rotations about axes y and z, respectively

$[\mathbf{C}]$ = damping matrix

$[\mathbf{K}]$ = stiffness matrix

$[\mathbf{M}]$ = mass matrix

$[C^s]$ = structural damping matrix

$[G^b]$ = gyroscopic matrix of the beam

$[G^d]$ = gyroscopic matrix of the disk

$[K^b]$ = stiffness matrix of the beam

$[K^b]_P$ = stiffness matrix of the beam due to the axial force

$[M^b]$ = mass matrix of the beam

$[M^b]_C$ = mass matrix used for computing the centrifugal forces

$[M^d]$ = mass matrix of the disk

$\overline{\mathbf{C}}$ = modal damping matrix

$\overline{\mathbf{K}}$ = modal stiffness matrix

$\overline{\mathbf{M}}$ = modal mass matrix

$\overline{\mathbf{F}}$ = modal force vector

$\{\mathbf{F}(t)\}$ = applied force vector

$\{\mathrm{R(x)}\}$ = internal force of the system

$\{\mathbf{x}\}$ = displacement vector including deflections and rotations

$\{F^b\}$ = force vector acting on the beam

$\{F^d\}$ = force vector due to the unbalance of the disk

Acknowledgements

I would like to sincerely express my gratitude and appreciation to my supervisor, Professor Altintas, who is a very knowledgeable, considerate, and caring professor. His support, guidance, and encouragement have been a highlight of my experience at UBC.

Many thanks go to my colleagues at the Manufacturing Automation Laboratory (MAL) for their friendship and great help. Professor Altintas and my colleagues have created a wonderful place for studying, working, and entertainment in MAL.

I would also like to take this opportunity to express my sincere appreciation to my parents, brother, and sisters for being a great source of encouragement to me.

Finally, I would like to thank my wife Shuxia and my son Chris for their understanding and encouragement, and especially my 3-year-old daughter Emily, who spent numerous evenings and weekends with me in the lab, sleeping or playing by herself while I was working.

Chapter 1
Introduction

With the new development of cutting-tool material technology, high-speed machining is widely accepted at present, especially in the aerospace and die/mold industry. High-speed machining can increase manufacturing efficiency, produce a better surface finish, and lead to smaller cutting forces and thermal distortion of the work-piece. Since the main objective of high-speed machining is to increase the metal removal rate (MRR) by adopting more aggressive cutting conditions that may cause chatter vibrations and spindle failure, the machine tools must have higher rigidity, stability, and reliability. Among all the components of a machine tool, the spindle system is the most critical part, since its dynamic properties directly affect the cutting ability of the whole machine tool.

A typical pulley-driven spindle system for milling is shown in Figure 1-1 and Figure 1-2. It consists of the tool, tool holder, spindle shaft, bearings, pulley, clamping unit, and the housing attached to the machine tool. For a very high-speed spindle, as illustrated in Figure 1-3, the motor is usually seated inside the spindle housing for better balance.

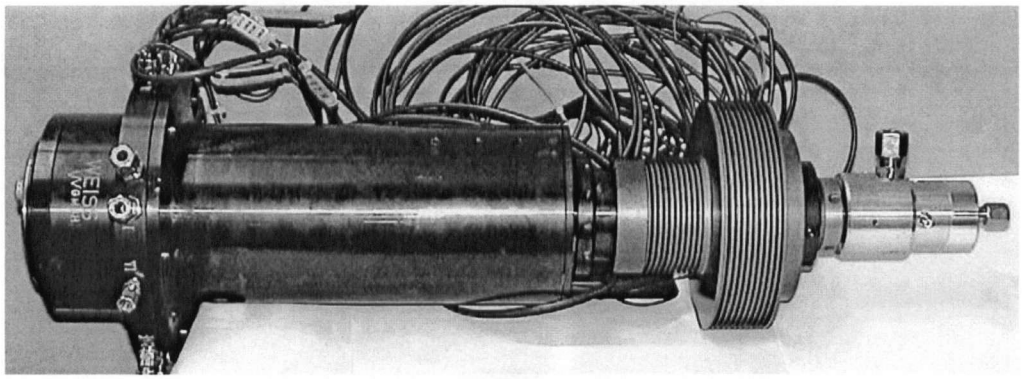

Figure 1-1: An instrumented spindle system

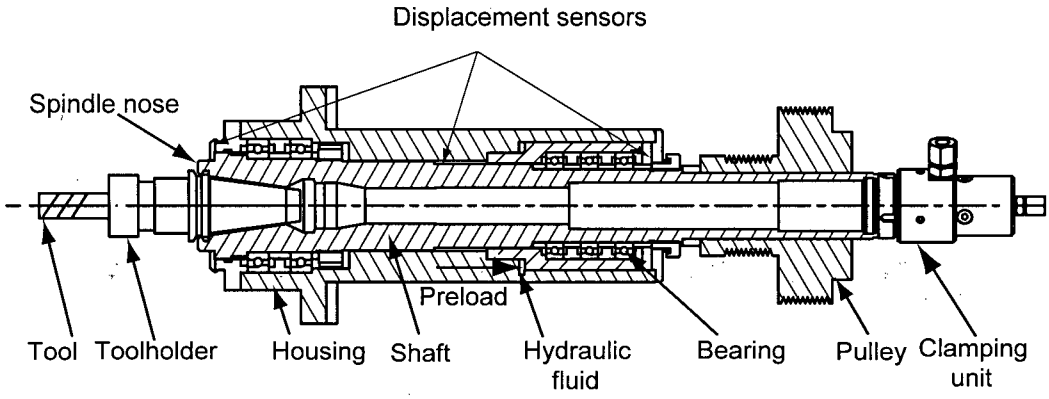

Figure 1-2: A spindle system

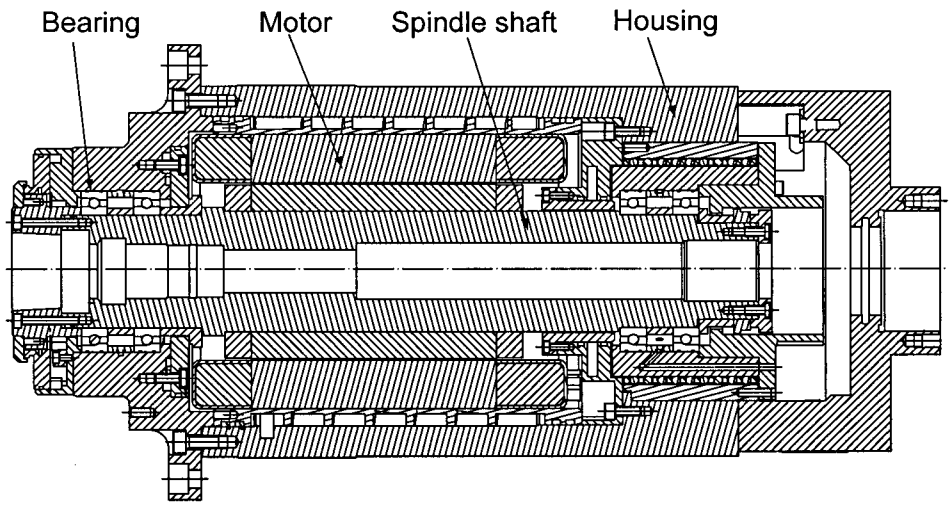

Figure 1-3: A motorized spindle

Spindles either carry cutting tools, as in milling operations, or work-pieces, as in turning. Milling operation is one of the most frequently used machining methods in industry, and can be classified as either conventional or high-speed milling.

Thermal-resistant materials, such as stainless steel, titanium and nickel alloys, are cut at low cutting speeds, typically under 100 m/min. The required spindle speed is about 5000 rev/min. However, high dynamic stiffness and torque are required from the spindle drive system for machining thermal-resistant materials. Materials of low yield strength, such as the aluminum alloys widely used in the aerospace industry, can be cut at very high speeds (i.e., 4000 m/min) without any thermal softening of the cutting tools. The spindle speed in milling

aluminum alloys can approach the physical constraints of the bearings, currently around 60,000 rev/min. High powers are required to deliver the required speed and torque at the high-speed range, and the speed effects have to be considered in the design of high-speed spindles.

When the machine is cutting, cutting forces are applied to the tool, and subsequently cause the spindle to vibrate. Vibrations induce the change of chip thickness, which in turn leads to variation in cutting forces. Under certain cutting conditions, self-excited vibration, which is also called chatter vibration, may occur. Chatter vibrations limit the depth of cut, produce a poor surface finish, reduce productivity, overload bearings, and shorten the spindle life [1]. In the worst case, chatter vibrations may chip the tool, damage the work-piece, and even destroy the spindle. In fact, a significant number of spindles are damaged in industry due to dynamic overloading of bearings resulting from chatter vibrations, especially in high-speed milling operations. The spindle, tool-holder, and tool are the main contributors to chatter vibrations. Therefore, in order to predict chatter vibrations, the dynamics of the spindle system has to be correctly obtained by either measurement or numerical simulation.

The most commonly used mathematical model for analyzing a spindle system is shown in Figure 1-4. The equation describing its dynamic behavior is as follows:

$$[\mathbf{M}]\{\ddot{x}\}+[\mathbf{C}]\{\dot{x}\}+[\mathbf{K}]\{x\}=\{\mathbf{F}(t)\} \tag{1.1}$$

where $[\mathbf{M}]$ is the mass matrix of the spindle system, $[\mathbf{C}]$ is the damping matrix, $[\mathbf{K}]$ is the stiffness matrix including stiffness of bearings and spindle shaft, $\{\mathbf{x}\}$ is the displacement vector including deflections and rotations, and $\{\mathbf{F}(t)\}$ is the applied force vector.

In this simple model, only the tool, tool-holder, spindle shaft, and bearings are included. The first three parts are assumed to be rigidly connected, and are modeled as beams with different cross-sectional areas. The bearings are simplified as linear springs, with stiffness in both the radial and axial directions. When the machine is cutting, the cutting forces in three directions, X, Y and Z, are applied at the tool tip. Deformations at the tool tip will directly affect the quality of the machined parts.

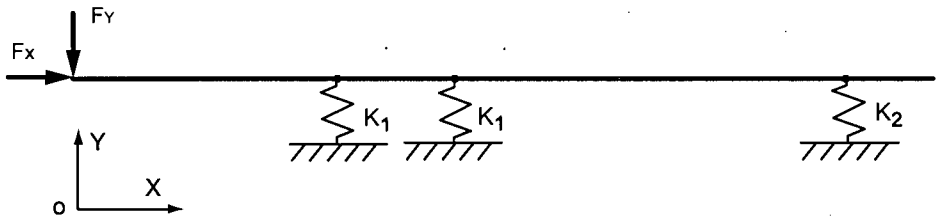

Figure 1-4: A typical model of a spindle system

However, in practice the results from the above model do not always match the actual measurements. The main reason is that the bearings and their coupling with the spindle system are not accurately modeled. Furthermore, the spindle housing and machine tool are not included in the model. During cutting, the spindle shaft is deformed by the forces and moments transmitted through the contact surface between the tool-holder and spindle shaft, which is supported by bearings. These forces are transferred to the spindle housing and cause the deformations of the housing and spindle head.

Bearing stiffness changes with the forces applied on the spindle, and these changes cannot be reflected in the simple linear model described above. For example, in Figure 1-5 the bearings are preloaded by the nut through the length difference of the spacers. In this bearing configuration, the inner spacer is a little shorter than the outer one, and the difference depends on the magnitude of the required preload. Before the spindle works, the two bearings have the same stiffness in both the radial and axial directions. However, when an axial force is applied on the spindle shaft, bearing no.1 becomes tight and bearing no. 2 gets loose. In other words, the two bearings will have different stiffness. The radial forces affect bearing stiffness more than the axial force does. In milling operations, the radial forces are stronger than the axial force, especially when the tool-holder and tool are long. The bending moments at the bearing locations produced by these forces therefore have a significant influence on bearing stiffness.

Bearing deflection contributes about 30-50% of the total spindle deflection [2]. Bearing stiffness depends on the structure of the bearing, such as size of the bearing balls, curvature of the bearing rings, contact angle, preload, deformation of the spindle shaft and housing, thermal expansion, and spindle speeds. At higher spindle speeds, the centrifugal force and

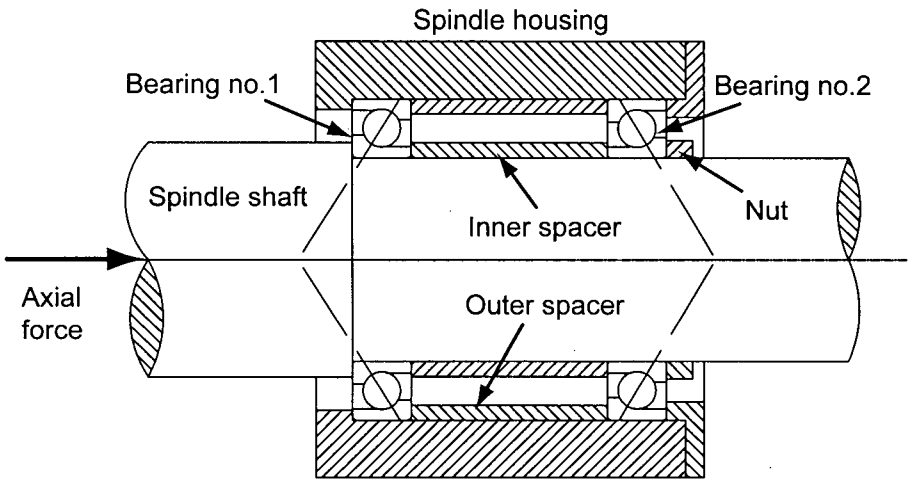

Figure 1-5: Back-back bearing configuration

gyroscopic moment have to be considered in the analysis and design of spindles. The dynamics of the spindle system changes with the cutting forces and spindle speeds, especially when the preload on bearings is low. All these elements lead to a non-linear problem for the spindle system.

Hence, accurately predicting the dynamics of the machine-tool spindle system is the key issue in designing spindles, enabling designers to predict the performance of spindles before they are manufactured.

The objective of this thesis is to develop a general method for simulating milling operations, so that designers can check the performance of the spindle system and improve the machine tool design before it is physically manufactured. This general model can be used to predict the stiffness of bearings, contact forces on bearing balls, natural frequencies, frequency response functions, and time history response under impact/cutting forces for a given preload. The thesis also presents a general method for obtaining either the maximum dynamic stiffness or the maximum chatter-free depth of cut by adjusting the dynamics of the spindle system.

The thesis is organized as follows:

The review of literature is presented in Chapter 2. In Chapter 3, system equations for general spindle systems are formulated. Dynamic equations for rotating disk and Timoshenko

beam with centrifugal force and gyroscopic moment are developed. The finite element method is used to establish the discrete system equations. A nonlinear element is formed based on Jones' bearing model and coupled to the system equations for spindle systems.

In Chapter 4, the model for the spindle system is verified by a benchmark and an instrumented spindle under free-free boundary conditions. The preload and tool-holder effects on the dynamics of the spindle are discussed. In Chapter 5, a general modeling method is presented for the spindle-machine tool systems. The cutting test for milling operation is performed to verify the proposed methods. The speed effects on the dynamics of the spindle-machine tool system are also discussed in this chapter. Chapter 6 describes a general method for optimizing the spindle. The conclusions and possible future research directions are pointed out in Chapter 7. Appendices clarifying some of the computational details are provided following the References.

Chapter 2

Literature Review

As mentioned in Chapter 1, the dynamics of spindle systems mainly depends on the characteristics of the bearings, tool-holder interface, spindle shaft, and housing. This review will give an overview of previous research work on modeling of spindle systems, with emphasis on the modeling of bearings and spindle shafts.

2.1 Bearings

The bearing system, one of the most critical components of high-speed spindles, must be able to provide high rotational speed and have a reasonable load capacity and life. The types of bearings available for high-speed spindles include angular-contact ball bearings, roller bearings, and taper roller bearings shown in Figure 2-1.

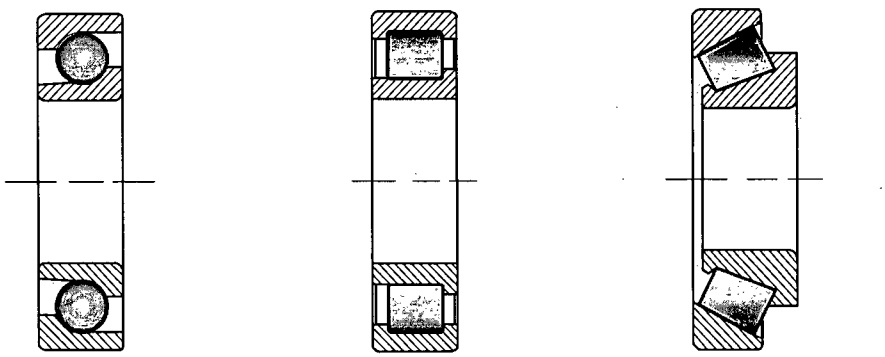

Figure 2-1: Three types of commonly used bearings in high-speed spindles

Angular contact ball bearings are most commonly used today in high-speed spindles. This is because angular contact ball bearings can provide the required precision, load carrying capacity, and spindle speeds. In addition, the costs are low compared to hydrostatic, aerostatic or magnetic bearings. Angular contact ball bearings are designed to provide the capabilities to withstand external loads from both axial and radial directions when they are properly preloaded. In some cases, taper roller bearings are also used because they can offer larger load-carrying capacity and higher stiffness than ball bearings. However, taper roller

bearings do not allow the high speeds required by high speed spindles. In this thesis, angular contact ball bearings are studied. Their basic terms are defined in Figure 2-2.

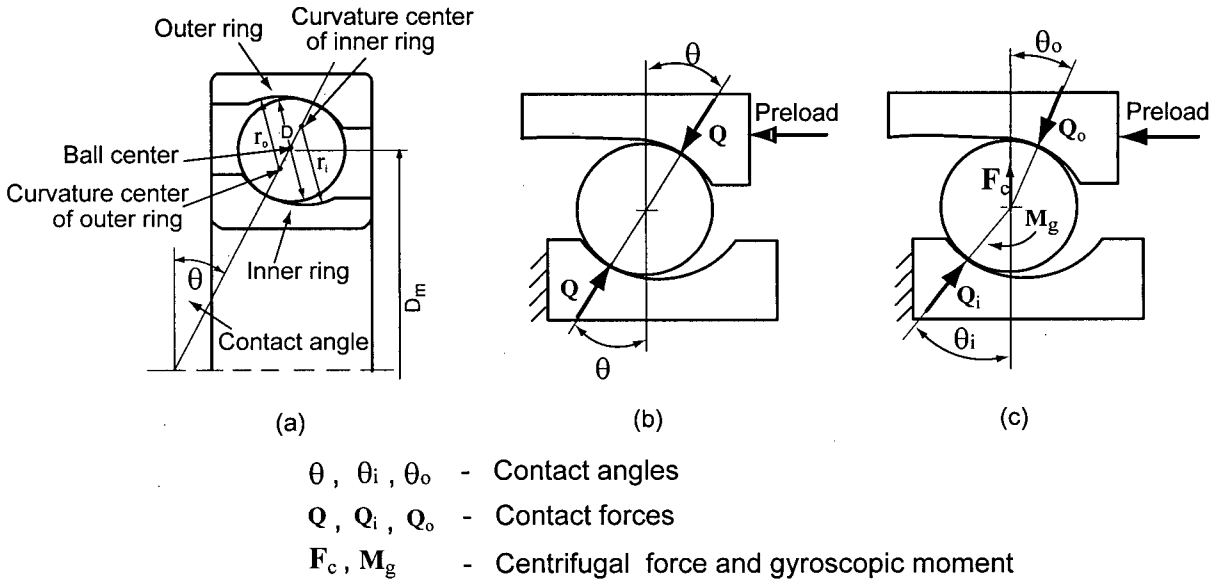

θ , θi , θo - Contact angles

Q , **Qi** , **Qo** - Contact forces

Fc , **Mg** - Centrifugal force and gyroscopic moment

Figure 2-2: Basic terms for angular ball bearings

One of the most important specifications for bearings is the maximum speed, which is theoretically determined by lubrication method, preload, and loading. However, in practice the DmN number is as a benchmark used to specify the bearing speed, and is calculated by multiplying the pitch diameter Dm, in millimeters, by the bearing speed, in rpm. The current DmN number is 2,000,000 for grease lubrication and 3,500,000 for oil-air lubrication [3].

Another specification for angular contact ball bearings is the contact angle (θ). For machine-tool spindles, the typical contact angles are 12, 15, 25, and 40 degrees. The contact angle determines the ratio of the radial and axial loading. The lower the contact angle, the greater the radial load capacity. Therefore, bearings with 25 or 40-degrees contact angles are suitable for spindles that are used primarily for drilling where the largest force is in the axial direction. Bearings with 15-degree contact angles are suitable for milling where the radial forces are dominant.

When the spindle is not rotating, the inner ring contact angle θ_i is equal to the outer ring contact angle θ_o , and the inner ring contact force Q_i is equal to the outer ring contact force Q_o. However, when the spindle is rotating, due to the centrifugal force F_c , gyroscopic

moment M_g, and cutting forces, the inner ring contact angle θ_i and contact force Q_i are no longer equal to the outer ring contact angle θ_o and contact force Q_o , respectively.

Angular contact ball bearings have to be preloaded in order to maintain rotational accuracy and enough stiffness in both the radial and axial directions. The magnitude of the preload is usually designated as light, medium, or heavy. Light preloaded bearings allow maximum speed but have less stiffness, and are usually used for very high speed spindles where cutting forces are small. Heavy preloading allows less speed but higher stiffness, and is usually used in lower speed spindles for roughing operations.

There are two ways of applying the preload to angular contact ball bearings. One is called fixed-position preload, as shown in Figure 1-5, wherein the inner bearing spacer is a little shorter than the outer bearing spacer. The advantage of this type of preload system is that the bearing stiffness can be set higher by adjusting the spacer length. However, the preload will increase due to centrifugal force and thermal expansion during spindle rotation. Excessive preload causes the bearings to seize, which may lead to spindle failure.

Another way of applying preload is so-called constant preload illustrated in Figure 2-3, wherein a spring is used instead of the outer bearing spacer. The spring absorbs the axial expansion of the spindle shaft that leads to increased preload due to temperature rise. The spring provides relatively constant preload, and over-preload can be avoided even in high-speed operations. The disadvantage of this method is that spindle stiffness decreases due to external forces, such as cutting forces. Therefore, this preload method is usually used in high-speed spindles where the speed exceeds 20,000 rpm.

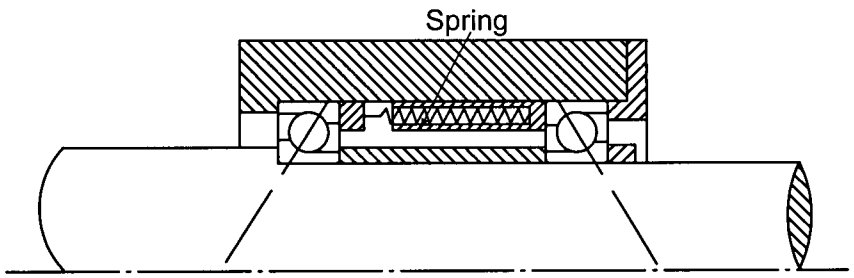

Figure 2-3: Constant preload mechanism

When the bearings are loaded only by preload, in other words the spindle is not rotating, it is possible to predict the bearing stiffness. However, when the spindle is cutting, especially when the spindle shaft is not rigid, the bearing will be in a very complex working condition, as shown in Figure 2-4. The forces acting on the bearing ring can be expressed as:

$$\mathbf{F} = \sum_{k=1}^{N} f\left(\delta_i, \delta_o, \boldsymbol{\delta}^{(2)}, \boldsymbol{\delta}^{(3)}, \theta_i, \theta_o, Q_i, Q_o, F_c, M_g, T\right) \tag{2.1}$$

where δ_i and δ_o are contact deformations between bearing balls and bearing rings; θ_i and θ_o are inner and outer bearing contact angles, respectively; $\boldsymbol{\delta}^{(1)}$, $\boldsymbol{\delta}^{(2)}$, $\boldsymbol{\delta}^{(3)}$ and $\boldsymbol{\delta}^{(4)}$ represent the deformation vectors for the nodes on the spindle shaft, inner ring, outer ring, and the spindle housing, respectively; $\boldsymbol{\delta}^{(2)}$ and $\boldsymbol{\delta}^{(3)}$ are the functions of $\boldsymbol{\delta}^{(1)}$, $\boldsymbol{\delta}^{(4)}$, respectively, depending on the configuration of bearing rings; Q_i and Q_o are contact forces; $\mathbf{F}_c$ and M_g are centrifugal force and gyroscopic moment depending on the spindle speed; and T is the temperature.

Establishing and solving the above equation (2.1) is the challenge in modeling angular contact ball bearings.

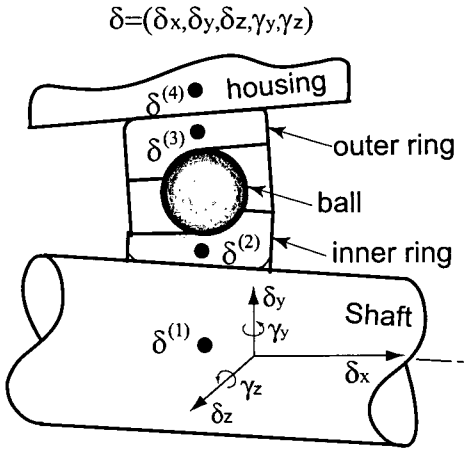

Figure 2-4: Bearing model

The simplest model for angular contact ball bearings is the conventional two-degrees-of-freedom model proposed by Palmgren [4]. This model considers only the axial and radial translations of the inner ring relative to the outer ring, which is usually suitable for most applications where misalignment and shaft bending effects are insignificant. The pioneering

work on mathematical models for angular-contact ball bearings was proposed by Jones [5], who developed a general theory for load-deflection analysis of bearings that considered centrifugal force and gyroscopic loading of the rolling elements under high-speed operation. In Jones' model, the inner ring has five degrees of freedom to describe the three translational deflections, two rotations, and the corresponding forces and moments. The outer ring is assumed to be rigid. The load-deflection relationship is established by examining the relative loading and motion at each ball in contact, including centrifugal forces and gyroscopic moments acting on the rolling elements. The inner ring loads at each ball are summed up to balance the inner ring loads from the shaft. DeMul et al. [6] established the dynamic equations in a matrix form that considered the centrifugal force but neglected the gyroscopic moment in the bearing. The advantage of DeMul's model is that the Jacobian matrix of the bearing is derived analytically, producing the bearing stiffness. Filiz and Gorur [7] conducted a load-deflection analysis of bearings under combined axial and radial loads. This analysis produced a simplified model for determining the incremental stiffness in axial and radial directions, as opposed to the differential stiffness obtained by Jones, DeMul et al., and Lim and Singh [8]. Ryan [9] developed a program called Rolling Element Bearing Analysis System (REBANS). This program operates in two modes. The primary mode accepts user-specified shaft/inner race displacements and calculates the resulting loads. The other mode accepts forces and moments as inputs and determines the corresponding shaft/inner race displacements. The bearing and shaft are analyzed independently in REBANS; hence, coupling effects are excluded. Houpert [10] and Hernot et al. [11] presented a stiffness matrix form with five degrees of freedom. Their model enables using the finite element method for solving the coupled problem of the spindle-bearing system, but the centrifugal forces and gyroscopic moments are not included. Harris [12] did a comprehensive analysis of different aspects of bearings, but his model is independent of the spindle or shaft.

Walford and Stone [13], [14] measured stiffness and damping for bearings under oscillating conditions. They used a two-degrees-of-freedom mathematical model to extract a representative stiffness value and found that the levels of damping obtained were considerably higher than expected. They concluded that this result was due to interaction among the races, housing, and shaft. Tiwari and Vyas [15] developed a technique for estimating nonlinear stiffness parameters for rolling bearings in rotor systems, based on an

analysis of the random response signals picked up from the bearing caps. The analysis uses a stochastic characteristic of the bearing excitation in conjunction with a single-degree-of-freedom model to estimate a representative stiffness. Marsh and Yantek [16] presented an experimental method for estimating the dynamic stiffness of precision bearings, based on measurements of the frequency response functions.

The effects of bearing rotation on stiffness were studied by Kraus et al. [17], who used an experimental method to determine the bearing stiffness and damping for a rotating spindle. Through modal analysis, they showed that spindle rotation changes the equivalent mass, stiffness, and damping of bearings. The equivalent mass increases with rotation speed. The stiffness, for the speed range tested, does not change, but damping decreases with increased speed. However, stiffness increases with the bearing preload. For example, by increasing bearing preload six times, stiffness increases by a factor of 1.5 in the transverse direction and 4.7 in the axial direction; damping decreases by 25 percent in the transverse direction, and increases by a factor of 1.7 in the axial direction. Wang et al. [18] and Shin [19] also built analytical models of high-speed spindle-bearing systems. Their results showed that bearing stiffness decreases with an increase in spindle speed.

Palmgren [4] conducted an early study of the thermal effect on bearing stiffness, and established the empirical relationships between rolling resistance and heat generation. Rolling resistance consists of viscous friction torque due to the lubrication and contact resistance resulting from the deformation of the elastic bodies. Harris [12] improved the prediction of heat generation in Palmgren's method by including the heat generation caused by the spin moments at bearing contact for the given operating speeds, loads, and lubricant properties. Gibson [20] presented a model of thermally induced bearing loads for machine-tool spindles. The model is built for angular contact bearings with a fixed preload that includes radial and axial thermal expansions. The importance of including radial and axial thermal expansion is shown when calculating thermally induced angular contact bearing loads.

In summary, Jones' bearing model is the most comprehensive and complete one for angular contact ball bearings. All other models are simplified versions of Jones' model that

neglect centrifugal force or gyroscopic moments, or both. In this thesis, Jones' bearing model is used, and it is extended to include the effects of deformation of the spindle housing.

2.2 Spindles

Spindles are the key components of all machine tools. Early spindle research focused mainly on static and quasi-static analysis, whereas current research is extended to optimal design by using dynamic analysis. Bollinger [21] analyzed the spindle for a lathe by using a finite difference model, in which the bearing is simulated as a simple radial spring and dashpot. Yang [22] conducted an in-depth analysis of the radial stiffness of machine-tool spindles. He concluded that shortening the overhang, and increasing the area moment of inertia of the spindle and the stiffness of the front bearing, can enhance the static stiffness of spindle systems. The addition of the third bearing may change the dynamics of the spindle, depending on the forces and moments exerted on it. Wardle et al. [23] examined the static and dynamic stiffness of a spindle-bearing system, and claimed that a hydraulically preloaded bearing arrangement can generate rigid spindles. Aini et al. [24] undertook an analysis of the spindle for a precision grinding machine tool supported with a pair of angular contact ball bearings by using a model with five degrees of freedom. In the model, the spindle is assumed to be a rigid shaft and the balls to be massless. Aini et al. [25] also carried out an experiment to investigate the frequency response of a grinding machine tool spindle, supported by preloaded angular contact ball bearings. Brandon and Shareef [26], [27] investigated the validity of several common assumptions used in analyzing machine-tool spindles, and discussed different types of differential equations for spindle models. El-Marhomy [28] presented an analytical method for determining the stability of elastic shaft-bearing systems using nonlinear bearing parameters.

All of the above-mentioned models use analytical methods for modeling simple structures, such as the continuous and lumped-mass models. These proposed models are only suitable for simple spindles, and are not practical for industrial applications. Moreover, many important factors for high-speed spindles, such as rotary inertia and gyroscopic moments, are not considered. However, with the popularization of computers, the finite element method has been widely used to analyze structures. It is more suitable for analyzing complex structures than the analytical methods are.

Ruhl and Booker [29] is one of the earliest researchers to use the finite element method for modeling of rotor systems. His model includes translational inertia and bending stiffness but neglects rotational inertia, gyroscopic moments, shear deformation, and axial load. Nelson [30], [31] used the Timoshenko beam theory to establish shape functions and formulate system matrices, including the effects of rotary inertia, gyroscopic moments, shear deformation, and axial load. Ozguven and Ozkan [32] developed a computer program that calculates the whirl speeds and dynamic response of multi-bearing rotor systems, including not only the effects of rotary inertia, gyroscopic moments, shear deformation, and axial load, but also of internal hysteretic and viscous damping. Reddy and Sharan [33], [34] added viscous damping to the simple bearing spring model to describe the bearing nonlinearities in his finite element analysis of spindles. This model was expanded by Wang and Chang [35] to include bearing axial stiffness using additional spring elements in the axial direction. There are many other papers [36]-[39] on the analysis of spindles using the finite element method. However, none of the above research considers the nonlinear bearing stiffness, which is related to external forces and rotational speeds for high-speed spindles.

In the past, little research has been conducted to model the coupling of bearings and spindles. The effects of preload and spindle speeds on bearing stiffness and the dynamics of the spindle system are seldom studied. Wardle et al. [23] presented a very simplified model for describing the dynamics of a spindle-bearing system with a constant preload. The theoretical maximum operating speed of the spindle system is increased by maintaining a constant preload, but Wardle neglected the softening of bearing stiffness due to rotational speeds. Aini et al. [24] combined a detailed angular contact ball bearing model with a spindle, but the spindle is assumed to be rigid. His model shows the importance of considering variations in bearing stiffness in spindle analysis. Chen et al. [40], [41] built a model for determining the response of a spindle-bearing system at high speeds by an analytical method. His model is a uniform Euler-Bernoulli beam supported by a pair of angular contact bearings. Using Jones' [5] bearing model, Chen analyzed the dynamic behavior of the spindle around the trivial equilibrium configuration with zero end loads. Only the axial preload is considered in this model. First, the Newton-Raphson iteration method is used to calculate the bearing stiffness matrix at a given spindle speed, then the dynamic behaviors are computed at this speed using the obtained bearing stiffness.

Jorgensen and Shin [42] used DeMul's bearing model and the Timoshenko beam to develop a model for a spindle supported by a pair of angular contact bearings, including cutting-load effects. The cutting load is divided into static and dynamic components. The dynamic loads are assumed to provide system excitation due to the dynamic motion of the cutting tool. Static load creates a deformed equilibrium in the bearing and spindle position. The influence coefficient matrix is formed on the base of the deformed equilibrium position by static loads, thus including bearing non-linearity. The coupling equations of the spindle and bearings are solved in the following manner. The spindle program calculates the reaction forces at the bearing locations. These loads provide input to the bearing subroutine, which returns the bearing deflections and reaction moments required for bearing compliance. Then the influence coefficient matrix, lumped masses, and inertia are computed to determine the eigen-pairs of the system. The problem with this method is whether the deformation under the static cutting forces really has influence on the coefficient matrix (i.e., stiffness matrix) for the new equilibrium position, since the deformation under the static cutting forces is negligible compared with the geometric dimensions of the spindle system.

Bossmanns et al. [43] and Lin et al. [44] proposed an integrated thermo-mechanical dynamic model for a motorized machine-tool spindle, using an empirical formula to calculate the stiffness of bearings. However, some constants need to be identified in order to use this model. Li and Shin [45], [46] presented a coupled spindle-bearing model that includes thermal effects to predict the bearing stiffness and natural frequencies of the spindle system, using DeMul's bearing model. The bearing configuration, however, is limited to several cases and the gyroscopic effect is not included. Only the natural frequencies are compared in these papers, not the FRF, which is most crucial in predicting the dynamic performance of the spindle during cutting.

All of the above models predict the natural vibration and frequency response for a specific spindle design, and consider only the spindle shaft and bearings. The effects of the machine tool on the spindle dynamics are neglected, leading to inaccurate predictions for most machine tools. Neither centrifugal force nor gyroscopic effect is included in modeling the spindle shaft. The bearings and spindle shaft are not systematically coupled. The contact forces on bearing balls and the time response of the spindle-bearing system under dynamic cutting forces have not been studied.

In this thesis, a general method has been developed for systematically modeling the bearings, spindle shaft, and housing by including the effects of preload and spindle speeds[47], [48]. This method can predict the bearing stiffness, frequency response functions, and time history of responses under impact or cutting forces. It can also simulate the milling operation to predict the cutting performance and contact forces on bearings. Jones' bearing model with both centrifugal forces and gyroscopic moments is used, and is extended to include the effects of deformation of the spindle housing. The model is verified by performing impact tests in free-free boundary conditions. The modal parameters of a vertical machining center (FADAL VMC2216) are identified, and a model for the spindle-machine tool system is developed. The effects of the machine tool on the spindle systems are studied. The cutting tests are conducted to verify the proposed methods. The studied model extends previous approaches by considering the influence of the machine tool structural dynamics.

2.3 Tool-holder

The tool-holder is a key component of the spindle system. The interface between the tool-holder and the spindle shaft plays a very important role in the dynamics of the spindle system. There are two main types of tool-holder interface, the CAT tool-holder and the HSK tool-holder. Both tool-holders are shown in Figure 2-5.

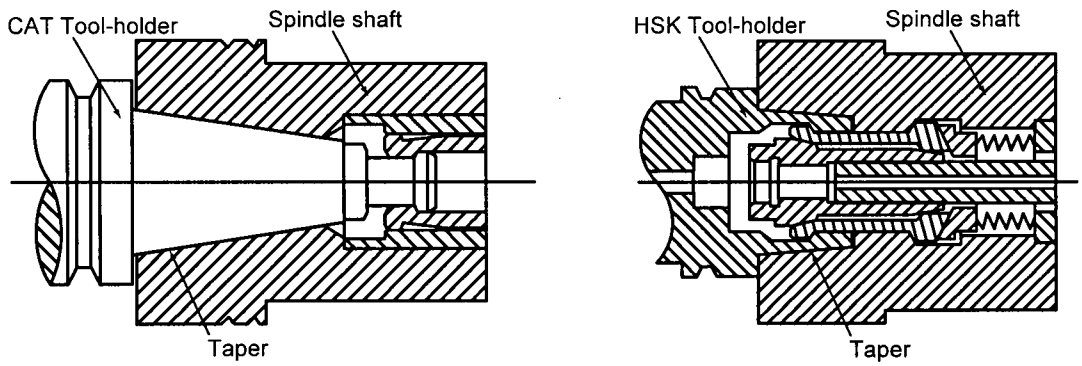

Figure 2-5: Two types of tool-holder

The shank of the CAT tool-holder is a solid structure and is stiffer than hollow-shank tool-holders like the HSK. The CAT tool-holder's overhang length from the spindle nose to the tool tip can be shorter than that of the HSK tool-holder. However, at high speeds the spindle taper expands and the tool-holder is pulled into the spindle, causing dimensional

errors of the work-piece in the direction of the spindle axis. Moreover, it is difficult to remove the tool-holder from the machine tool. HSK tool-holders overcome the high-speed shortcomings of CAT tool-holders. There are two contact surfaces: the tool-holder flange with the spindle nose, and the tool-holder taper with the spindle shaft taper. These two pairs of surfaces are always in contact, even at high speeds, due to the flexibilities of the hollow structure. Because of the shorter taper of the HSK tool-holder, the front bearings of the spindle can be placed closer to the spindle nose, so that spindle stiffness can be improved. However, the cutter overhang tends to be longer than the solid tool shank type because there is not enough space to put the cutter further into the taper.

This thesis does not include research on the tool-holder spindle interface, but results from other researchers are used to compare the effects of the tool-holder spindle interface on the dynamics of spindle systems.

2.4 Chatter Vibrations

Since one of the purposes of modeling the spindle system is to avoid chatter vibrations during machining process, chatter tests are conducted to verify the proposed models. In addition, chatter-free depth of cut is used as one of the objectives for optimization of the spindle. It is therefore necessary to briefly review chatter vibration theory here.

Chatter vibrations result from the self-excitation mechanism in the generation of chip thickness during the machining operation, which can be explained by a phenomenon called regeneration of waviness. Consider the example of simple turning shown in Figure 2-6. A wavy surface finish caused by the forced vibration of the spindle system is removed during the succeeding revolution, which also leaves a wavy surface due to spindle vibration. Depending on the phase shift between the two successive waves, the maximum chip thickness may exponentially grow while oscillating at a chatter frequency that is close to, but not equal to, a dominant structural mode in the system [53].

Extensive research has been conducted on establishing chatter-stability lobes [54]-[61]. The regeneration phenomenon was first explained by Tobias [54] and Tlusty and Polacek [55], who identified the main sources of self-excitation as being associated with the structural dynamics of the machine tool and the feedback between subsequent cuts. Tlusty and Polacek

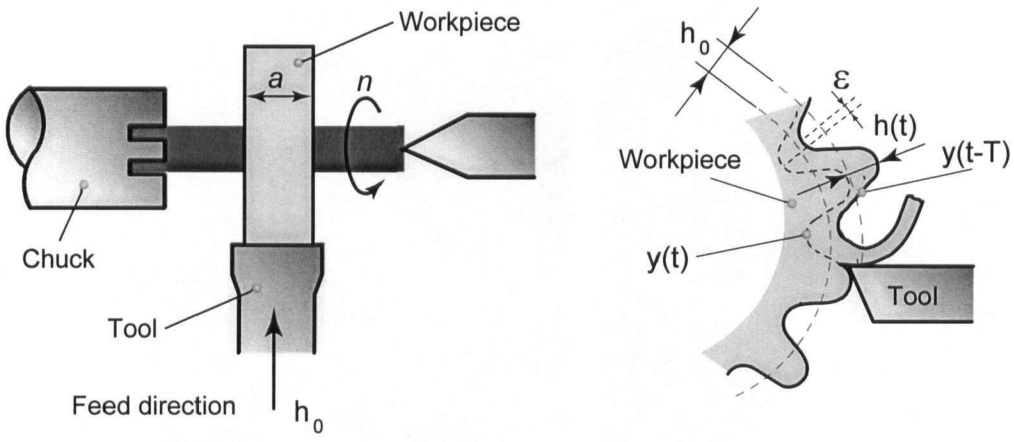

Figure 2-6: Chatter vibration mechanism in turning [53]

presented a practical stability law for orthogonal cutting systems, where the chatter-free axial depth of cut is expressed as a function of the real part of the dynamic compliance of the machine tool and work-piece. Tobias considered the effect of speed on stability and discovered the stability lobes. Later, Merrit [56] used feedback control theory to predict the same stability law proposed by Tlusty. These theories are applicable only to orthogonal cutting, where the direction of cutting force, chip thickness, and structural dynamics do not change with time. For 2D milling chatter problems, Tlusty applied his orthogonal cutting stability formulation to milling by using an average directional coefficient and an average number of flutes in the cut. Opitz and Bernardi [57] approximated the periodic coefficients with their average values. Instead of using a one-dimensional solution for milling stability like Tlusty[55] and Opitz[57], Minis and Yanushevsky[58], Altintas and Budak [59]-[61] developed two-dimensional approaches for milling-stability problems. Altintas' method is used in this thesis.

2.5 Optimization

Little research has been conducted on optimization of the spindle system. Yang [22] used an analytical method to optimize the bearing span for a spindle with only two bearings, which is not common in production spindles. Taylor et al. [49] developed a program to optimize the diameter of the spindle shaft for minimum static deflection. But the optimization for static stiffness does not guarantee that the design is also optimal for dynamic stiffness of

the spindle. Lee and Choi [50] conducted an optimization design in which the weight of the rotor-bearings system is minimized using the augmented Lagrange multiplier method.

All of the above work is based on simple spindles with only two bearings, in which the design variables and constraints are shaft diameter, bearing span, and bearing preload. The objectives are minimizing static deflection or weight of the spindles. Maeda et al. [51], [52] developed an expert spindle design system that can optimize bearing locations under the constraint of minimum depth of cut. Dynamics such as natural frequencies and chatter vibrations are included in the optimization. The proposed optimization method makes it possible to achieve the maximum depth of cut or dynamic stiffness by tuning the spindle modes through optimizing the locations of bearings and the motor for motorized spindles. However, this optimization method is only suitable for the specific spindle mainly used with one cutter.

In this thesis, the above optimization method is extended to multiple flute cutters.

2.6 Summary

In this chapter, an outline of the literature on the modeling of bearings and spindle systems has been presented. Jones' bearing model is the most comprehensive and complete one among all bearing models. All of the other models are simplified forms of Jones' model that neglect either centrifugal forces or gyroscopic moments, or both.

It has been shown that spindle dynamics is affected by a number of factors, such as tool-holder interface, spindle dimensions, bearings, preload, spindle speeds, thermal expansion, etc. Bearing stiffness is nonlinear and coupled with deformations of the spindle shaft and housing. All previous models have been developed only for a specific spindle, without considering either centrifugal force or gyroscopic moment from the rotating shaft and bearings, and include only bearings and the spindle shaft. The bearings and spindle shaft are not coupled systematically. The effects of the spindle housing and the machine tool on spindle dynamics are neglected, which is unacceptable for most machine-tool structures. There has been no research reported on the time-history response of the spindle system on machine tools under dynamic forces, such as cutting forces, in simulating the machining process.

Optimization design for machine-tool spindle systems has hardly been studied in the past. It is possible, however, to achieve maximum depth of cut or maximum dynamic stiffness by tuning the spindle modes through optimizing the locations of bearings.

In this thesis, Jones' bearing model is used and is extended to include the deformation of the spindle housing. The bearings, spindle shafts, housings, and machine tools are systematically modeled by including the effects of preload and spindle speeds.

Chapter 3

A General Mathematical Model for Bearing-Spindle Systems

A typical spindle system consists of tool, tool-holder, spindle shaft, housing, bearings, pulleys, sleeves and nuts, and the motor. The tool, tool-holder, spindle shaft, and housing can be modeled as Timoshenko beams; the pulley and nut as rigid disks; and the sleeve as a bar. The motor is modeled as a rigid mass. The commonly used elements in modeling spindle systems can be classified as the rigid disk, beam, bearing, and the bar, and are described below.

3.1 Equations of Motion for the Rigid Disk

A diagram of a rotor shaft with a disk is shown in Figure 3-1. $O-xyz$ is a fixed coordinate system, where the x-axis is coincident with the centerline of the shaft before the shaft is deformed. The coordinates of the point P on the disk are affected by the displacements u, v, w, θ_y, and θ_z shown in Figure 3-1.

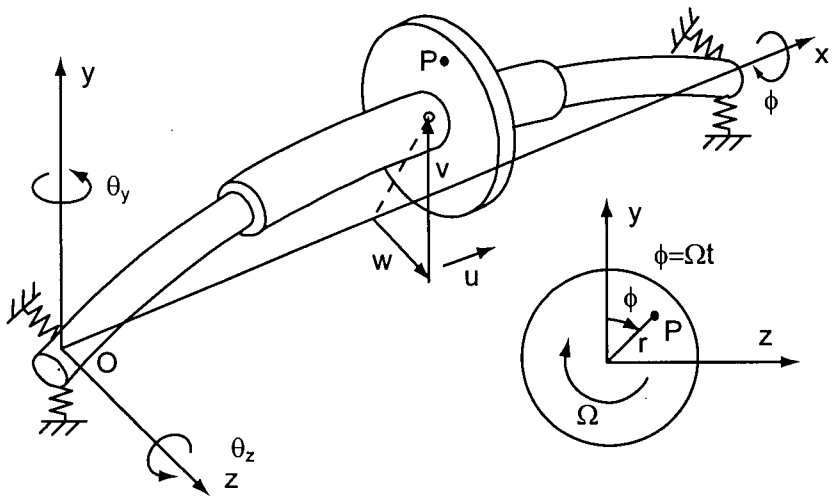

Figure 3-1: A rotor model

Assuming that the disk is fixed, the sequence of rotation of the axis of the coordinate system $O-xyz$ is not important, considering the small deformations. By rotating the coordinate system $O-xyz$ at an angle $-\theta_y$ about axis y, then $-\theta_z$ about axis z, the

coordinates of the point P in the $O-xyz$ system are changed due to the rotations θ_y and θ_z, and can be expressed as:

$$\begin{Bmatrix} x \\ y \\ z \end{Bmatrix} = \begin{Bmatrix} x_0 \\ 0 \\ 0 \end{Bmatrix} + [T] \begin{Bmatrix} 0 \\ r\cos\phi \\ r\sin\phi \end{Bmatrix} \tag{3.1}$$

where x_0 is the coordinate of the disk center, $\phi = \Omega t$, Ω is the rotational speed of the shaft, and the transformation matrix $[T]$ is:

$$[T] = [T_z][T_y] = \begin{bmatrix} \cos\theta_z & 0 & \sin\theta_z \\ 0 & 1 & 0 \\ -\sin\theta_z & 0 & \cos\theta_z \end{bmatrix} \begin{bmatrix} 1 & 0 & 0 \\ 0 & \cos\theta_y & -\sin\theta_y \\ 0 & \sin\theta_y & \cos\theta_y \end{bmatrix} \tag{3.2}$$

Substitute Eq.(3.2) into Eq.(3.1) and the coordinates of the point P become:

$$\begin{Bmatrix} x \\ y \\ z \end{Bmatrix} = \begin{Bmatrix} x_0 - r\cos\phi\sin\theta_z + r\sin\phi\sin\theta_y\cos\theta_z \\ r\cos\phi\cos\theta_z + r\sin\phi\sin\theta_y\sin\theta_z \\ r\sin\phi\cos\theta_y \end{Bmatrix} \tag{3.3}$$

By considering that the angular displacements θ_y and θ_z are very small, and using $\cos\theta_z \approx 1$ for x, and $\sin\theta_y \sin\theta_z \approx 0$ for y to ignore the higher-order rotational terms, Eq.(3.3) can be simplified as:

$$\begin{Bmatrix} x \\ y \\ z \end{Bmatrix} = \begin{Bmatrix} x_0 - r\cos\phi\sin\theta_z + r\sin\phi\sin\theta_y \\ r\cos\phi\cos\theta_z \\ r\sin\phi\cos\theta_y \end{Bmatrix} \tag{3.4}$$

The final position of the point P due to the displacements u, v, w, θ_y and θ_z is:

$$\begin{Bmatrix} x \\ y \\ z \end{Bmatrix} = \begin{Bmatrix} x_0 + u - r\cos\phi\sin\theta_z + r\sin\phi\sin\theta_y \\ v + r\cos\phi\cos\theta_z \\ w + r\sin\phi\cos\theta_y \end{Bmatrix} \tag{3.5}$$

Spindle shaft is a relative rigid shaft, the angular rotations are small. By assuming $\cos\theta_y \approx 1$, $\cos\theta_z \approx 1$, $\cos\theta_x \approx 1$, $\sin\theta_y \approx \theta_y$, and $\sin\theta_x \approx \theta_x$ for small displacements, the velocities of the point P are obtained as:

$$\begin{aligned}\dot{x} &= \dot{u} + \Omega r\theta_z \sin\phi + \Omega r\theta_y \cos\phi - r\dot{\theta}_z \cos\phi + r\dot{\theta}_y \sin\phi \\ \dot{y} &= \dot{v} - \Omega r \sin\phi - r\theta_z\dot{\theta}_z \cos\phi \\ \dot{z} &= \dot{w} + \Omega r \cos\phi - r\theta_y\dot{\theta}_y \sin\phi\end{aligned} \tag{3.6}$$

If the point P has a differential mass of dm, its kinetic energy is:

$$dT = \frac{1}{2} dm(\dot{x}^2 + \dot{y}^2 + \dot{z}^2) \tag{3.7}$$

where $dm = h\rho r dr d\phi$, h is the thickness of the disk, ρ is the density of the disk material.

The kinetic energy of the whole disk is:

$$T = \int_b^a \int_0^{2\pi} \frac{1}{2} t\rho r(\dot{x}^2 + \dot{y}^2 + \dot{z}^2) dr d\phi \tag{3.8}$$

where a and b are the inner and outer radii of the disk, respectively. By substituting Eq. (3.6) into Eq.(3.8), and neglecting the second order terms like ${\theta_y}^2$, ${\theta_z}^2$, and $\theta_y\theta_z$, the kinetic energy of the disk becomes:

$$T = \frac{1}{2} J_D \Omega^2 + \frac{1}{2} m_D \left(\dot{u}^2 + \dot{v}^2 + \dot{w}^2\right) + \frac{1}{2} I_D \left(\dot{\theta}_y^2 + \dot{\theta}_z^2\right) + \frac{1}{2} \Omega J_D \left(\dot{\theta}_y \theta_z - \theta_y \dot{\theta}_z\right) \tag{3.9}$$

where $I_D = (1/4) m_D (b^2 - a^2)$ is the diametral moment of inertia about axis y or z, $J_D = (1/2) m_D (b^2 - a^2)$ is the polar moment of inertia about axis x, and m_D is the mass of the disk.

If the center of the disk mass is not on the geometrical center of the disk, and the distance between these two centers is e, the virtual work done by unbalanced force is

$$\delta W = \delta v m_D e\Omega^2 \cos\Omega t + \delta w m_D e\Omega^2 \sin\Omega t \tag{3.10}$$

The generalized forces in the directions y and z are:

$$\begin{aligned}F_y &= m_D e\Omega^2 \cos\Omega t \\ F_z &= m_D e\Omega^2 \sin\Omega t\end{aligned} \tag{3.11}$$

By ignoring the damping and using the Lagrangian equation, the equation of motion for the rigid disk can be expressed as follows:

$$\left[M^d\right]\{\ddot{q}\} - \Omega\left[G^d\right]\{\dot{q}\} = \{F^d\} \tag{3.12}$$

where mass matrix $[M^d]$, gyroscopic matrix $[G^d]$, external force vector $\{F^d\}$ due to the unbalance of the disk, and displacement vector $\{q\}$ are as follows:

$$[M^d]=\begin{bmatrix} m_D & 0 & 0 & 0 & 0 \\ 0 & m_D & 0 & 0 & 0 \\ 0 & 0 & m_D & 0 & 0 \\ 0 & 0 & 0 & I_D & 0 \\ 0 & 0 & 0 & 0 & I_D \end{bmatrix} \qquad [G^d]=\begin{bmatrix} 0 & 0 & 0 & 0 & 0 \\ 0 & 0 & 0 & 0 & 0 \\ 0 & 0 & 0 & 0 & 0 \\ 0 & 0 & 0 & 0 & -J_D \\ 0 & 0 & 0 & J_D & 0 \end{bmatrix}$$

$$\{F^d\}=\begin{Bmatrix} 0 \\ m_D e\Omega^2 \cos\Omega t \\ m_D e\Omega^2 \sin\Omega t \\ 0 \\ 0 \end{Bmatrix} \qquad \{q\}=\begin{Bmatrix} u \\ v \\ w \\ \theta_y \\ \theta_z \end{Bmatrix}$$

Note that there is no stiffness matrix term in Eq. (3.12). It will be derived from the flexible shaft later.

3.2 Equations of Motion for Timoshenko Beam with Speed Effects

A section of the shaft, which is treated as a Timoshenko beam, is shown in Figure 3-2. A Cartesian coordinate system named $O-xyz$ is defined on the beam where the x-axis is coincident with the centroidal axis before the beam is deformed.

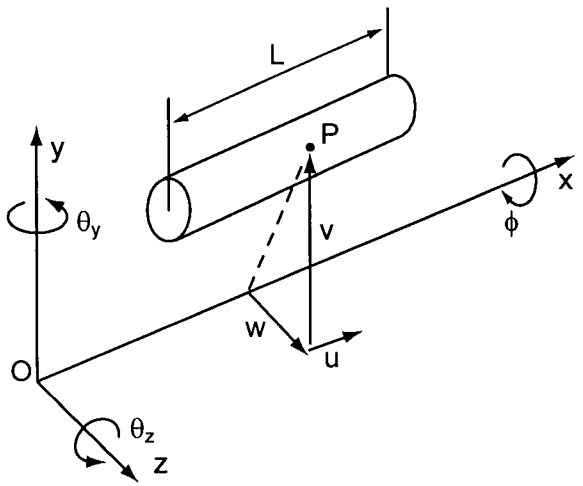

Figure 3-2: A section of shaft

3.2.1 Kinetic Energy

Similar to the rigid disk, the kinetic energy for a section of beam with a length L is:

$$T = \int_0^L \frac{1}{2} J\rho\Omega^2 dx + \int_0^L \frac{1}{2} \rho A\left(\dot{u}^2 + \dot{v}^2 + \dot{w}^2\right)dx + \int_0^L \frac{1}{2} I\rho\left(\dot{\theta}_y^2 + \dot{\theta}_z^2\right)dx + \int_0^L \frac{1}{2} \Omega J\rho\left(\dot{\theta}_y\theta_z - \theta_y\dot{\theta}_z\right)dx \quad (3.13)$$

where $I = (1/4)\pi R^4$, $J = (1/2)\pi R^4$, R is the radius of cross-section of the beam, A is the cross-sectional area, ρ is the density of the material, and Ω is the rotational speed of the beam. The first term is the energy of rotation about the axis x. The second term is the energy of translational movement. The third term is the energy of rotation about the axis y and z. The last term is the energy due to the gyroscopic moment. The torsional degree of freedom is considered, the torsional energy is not included.

3.2.2 Potential Energy

The deformed and undeformed beams in the $x-y$ plane are illustrated in Figure 3-3. Due to the shear deformation γ_y and γ_z of the beam cross-section, the tangent to the beam center curve differs from the normal to the beam cross-section.

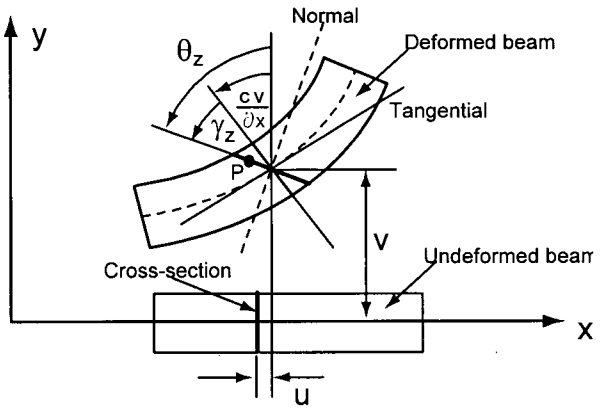

Figure 3-3: Deformed and undeformed beams in $x-y$ plane

The rotations of the beam cross-section can be expressed in the $x-y$ plane as:

$$\theta_z = \gamma_z + \frac{\partial v}{\partial x} \quad (3.14)$$

and in the $x-z$ plane as:

$$\theta_y = \gamma_y - \frac{\partial w}{\partial x} \tag{3.15}$$

where γ_y and γ_z are shear deformations due to the shear forces in beam cross-section.

By assuming that the beam cross-section remains plane after deformation, the displacements of the point P on the cross-section can be written as:

$$\begin{aligned} u(x,y,z,t) &= u(x,t) + \theta_y z - \theta_z y \\ v(x,y,z,t) &= v(x,t) \\ w(x,y,z,t) &= w(x,t) \end{aligned} \tag{3.16}$$

If the second-order strains are considered for the axial direction, the strains at the point P can be expressed as:

$$\begin{aligned} \gamma_{yx} &= \frac{\partial v}{\partial x} + \frac{\partial u}{\partial y} = -\gamma_z \\ \gamma_{zx} &= \frac{\partial w}{\partial x} + \frac{\partial u}{\partial z} = \gamma_y \\ \varepsilon_{xx} &= \frac{\partial u}{\partial x} + \frac{\partial \theta_y}{\partial x} z - \frac{\partial \theta_z}{\partial x} y + \frac{1}{2}\left(\frac{\partial v}{\partial x}\right)^2 + \frac{1}{2}\left(\frac{\partial w}{\partial x}\right)^2 \end{aligned} \tag{3.17}$$

The potential energy of the beam is:

$$V = \int \frac{1}{2} E \varepsilon_{xx}^2 dV + \int \frac{1}{2} k_s A G \gamma_{yx}^2 dV + \int \frac{1}{2} k_s A G \gamma_{zx}^2 dV \tag{3.18}$$

where E and G are the Young's modulus and shear modulus of the material, respectively, A is the area of cross-section and k_s is the transverse-shear form factor. For the circular cross-section beam [69]:

$$k_s = 9/10 \text{ or } k_s = \frac{6(1+\upsilon)(1+p^2)^2}{(7+6\upsilon)(1+p^2)^2 + (20+12\upsilon)p^2}, \text{ where } p = \frac{D_i}{D_o}$$

By substituting Eq.(3.17) into Eq.(3.18) and canceling the third-order terms, the potential energy of the beam is obtained:

$$V = \int_0^L \frac{1}{2} EA\left(\frac{\partial u}{\partial x}\right)^2 dx + \int_0^L \frac{1}{2} EI\left[\left(\frac{\partial \theta_y}{\partial x}\right)^2 + \left(\frac{\partial \theta_z}{\partial x}\right)^2\right] dx$$
$$+ \int_0^L \frac{1}{2} k_s AG\left[\left(\theta_y + \frac{\partial w}{\partial x}\right)^2 + \left(\theta_z - \frac{\partial v}{\partial x}\right)^2\right] dx \tag{3.19}$$
$$+ \int_0^L \frac{1}{2} EA\left[\left(\frac{1}{2}\left(\frac{\partial v}{\partial x}\right)^2\right)^2 + \left(\frac{1}{2}\left(\frac{\partial w}{\partial x}\right)^2\right)^2\right] dx$$

3.2.3 External Work

The work done by external forces is:

$$W = \int_0^L \left(q_x u + q_y v + q_z w + m_y \theta_y + m_z \theta_z\right) dx + \int_0^L \frac{1}{2} \Omega^2 v^2 \rho A dx + \int_0^L \frac{1}{2} \Omega^2 w^2 \rho A dx \tag{3.20}$$

where q_x, q_y *and* q_z are distributed load per unit length in directions x, y, and z, respectively, and m_y *and* m_z are distributed moment per unit length about axis y and z, respectively.

3.2.4 Equations of Motion

By using Hamilton's Principle,

$$\delta I = \delta \int_{t_1}^{t_2} \left(T - V + W\right) dt = 0 \tag{3.21}$$

the following equations of motion for the beam are obtained:

$$\rho A \frac{d^2 u}{dt^2} - EA \frac{\partial^2 u}{\partial x^2} - q_x = 0$$
$$\rho A \frac{d^2 v}{dt^2} - \frac{\partial}{\partial x}\left[k_s AG\left(\frac{\partial v}{\partial x} - \theta_z\right) - P_a \frac{\partial v}{\partial x}\right] - q_y - \Omega^2 \rho A v = 0$$
$$\rho A \frac{d^2 w}{dt^2} - \frac{\partial}{\partial x}\left[k_s AG\left(\frac{\partial w}{\partial x} + \theta_y\right) - P_a \frac{\partial w}{\partial x}\right] - q_z - \Omega^2 \rho A w = 0 \tag{3.22}$$
$$\rho I \frac{d^2 \theta_y}{dt^2} + \Omega \rho J \frac{d\theta_z}{dt} - EI \frac{\partial^2 \theta_y}{\partial x^2} + k_s AG\left(\frac{\partial w}{\partial x} + \theta_y\right) - m_y = 0$$
$$\rho I \frac{d^2 \theta_z}{dt^2} - \Omega \rho J \frac{d\theta_y}{dt} - EI \frac{\partial^2 \theta_z}{\partial x^2} - k_s AG\left(\frac{\partial v}{\partial x} - \theta_z\right) - m_z = 0$$

where the first equation is the force equilibrium along axis x. The second and third equations are the force equilibrium along axis y and z. The fourth and fifth equations are the moment equilibrium about axis y and z. $P_a = 1/2\,EA(\partial v/\partial x)^2$ or $P_a = 1/2\,EA(\partial w/\partial x)^2$ is the axial force contributing to the bending deformation.

3.2.5 Finite Element Equations

The following equations of the beam in matrix forms can be obtained by using the finite element method:

$$[M^b]\{\ddot{q}\} - \Omega[G^b]\{\dot{q}\} + ([K^b] + [K^b]_P - \Omega^2[M^b]_C)\{q\} = \{F^b\} \tag{3.23}$$

where $[M^b]$ is the mass matrix, $[M^b]_C$ is the mass matrix used for computing the centrifugal forces, $[G^b]$ is the gyroscopic matrix which is skew-symmetric, $[K^b]$ is the stiffness matrix, $[K^b]_P$ is the stiffness matrix due to the axial force, and $\{F^b\}$ is the force vector, including distributed and concentrated forces. The superscript b represents the beam. The details of the matrices are shown in Appendix A. The damping matrix is not included here, and is estimated from modal damping identified experimentally.

The bar element is a special case of the beam element. It takes only the axial stiffness of the beam element, and will not be presented in this thesis.

3.3 Mathematical Model for Angular Contact Ball Bearings

The Jones' bearing model [5] is used in this thesis, because this model is the most complete one and includes both centrifugal forces and gyroscopic moments from the rolling elements of the bearing. It is, however, the most complex model to implement. All bearing models developed subsequently are simplified by neglecting either the centrifugal forces or the gyroscopic moments. The Jones' bearing model is extended in this thesis to include the deformations of the spindle housing.

Some assumptions for the model of the angular contact ball bearing include the following:

- Lubrication does not change the dynamic characteristics of the bearings significantly

- Friction between bearing balls and rings is ignored
- Thermal expansion is not considered
- Hertzian contact theory is used to compute the contact deformation between bearing balls and bearing rings

3.3.1 Contact Force and Deformation for Angular Contact Ball Bearings

The geometry of an angular contact ball bearing and coordinate system are shown in Figure 3-4.

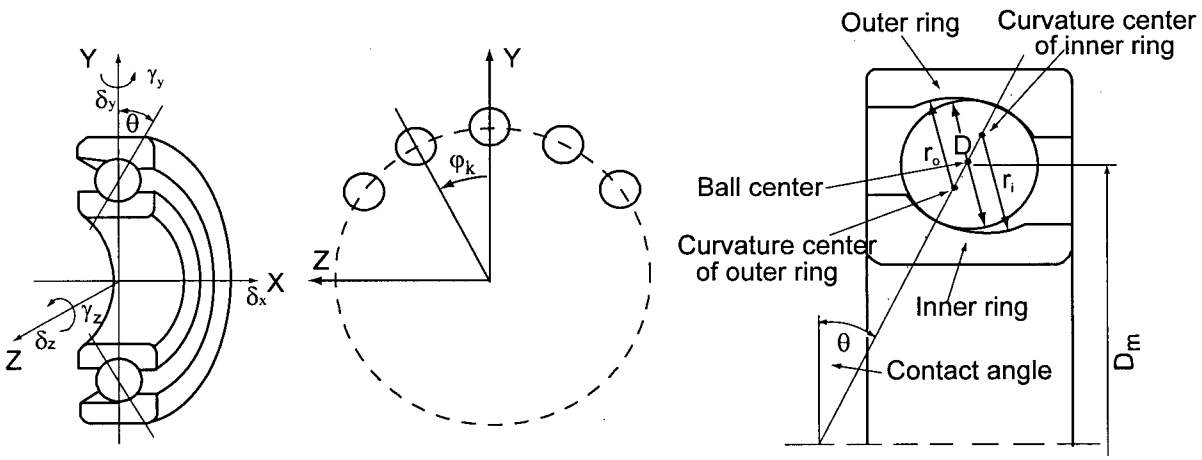

Figure 3-4: Geometry of an angular contact ball bearing

Hertzian contact forces between the inner ring and the balls, and the outer ring and the balls, are expressed by [12]:

$$\begin{aligned} Q_{ik} &= K_i \delta_{ik}^{3/2} \\ Q_{ok} &= K_o \delta_{ok}^{3/2} \end{aligned} \tag{3.24}$$

where δ_{ik} and δ_{ok} are the relative normal contact displacements between ball and inner ring, and ball and outer ring, respectively. Lowercase k is the index of bearing balls. K_i and K_o can be obtained from the following formulas [62][63]:

$$
\begin{aligned}
Q &= K\delta^{3/2} \\
K &= \frac{\pi\kappa E'}{3\mathbf{F}}\sqrt{\frac{2\mathbf{E}R_{xy}}{\mathbf{F}}} \\
\kappa &= 1.0339\left(\frac{R_y}{R_x}\right)^{0.6360} \\
\mathbf{F} &= 1.5277 + 0.6023\ln\left(\frac{R_y}{R_x}\right) \\
\mathbf{E} &= 1.0003 + 0.5968\left(\frac{R_x}{R_y}\right)
\end{aligned}
\tag{3.25}
$$

and $E' = 2/\left(\left(1-\mu_a^2\right)/E_a + \left(1-\mu_b^2\right)/E_b\right)$, $R_{xy} = R_x R_y/\left(R_x + R_y\right)$. For the inner-ring contact, R_x and R_y are:

$$
\begin{aligned}
R_x &= \frac{D}{2}(1-\gamma_i) \\
R_y &= D\frac{f_i}{2f_i - 1}
\end{aligned}
\tag{3.26}
$$

where $\gamma_i = D\cos\theta_{ik}/D_m$

For the outer ring contact, R_x and R_y are:

$$
\begin{aligned}
R_x &= D\frac{f_o}{2f_o - 1} \\
R_y &= \frac{D}{2}(1+\gamma_o)
\end{aligned}
\tag{3.27}
$$

where $\gamma_o = D\cos\theta_{ok}/D_m$.

For an elliptical contact area, the stress at the geometrical center is:

$$
\sigma = \frac{3Q}{2\pi ab} \tag{3.28}
$$

where $a = \left(6\kappa^2\mathbf{E}R_{xy}Q/\pi E'\right)^{1/3}$, $b = \left(6\mathbf{E}R_{xy}Q/\pi\kappa E'\right)^{1/3}$

3.3.2 Geometry and Force Relationship of the Bearings

When the forces are applied to the bearings, the distance between the curvature centers of the bearing rings changes, as shown in Figure 3-5.

Assume that $\delta_x^i, \delta_y^i, \delta_z^i, \gamma_y^i, \gamma_z^i$ are displacements of the inner ring, and $\delta_x^o, \delta_y^o, \delta_z^o, \gamma_y^o, \gamma_z^o$ are displacements of the outer ring. The relative displacements between the inner ring and the outer ring are:

$$\begin{aligned} \Delta\delta_x &= \delta_x^i - \delta_x^o \\ \Delta\delta_y &= \delta_y^i - \delta_y^o \\ \Delta\delta_z &= \delta_z^i - \delta_z^o \\ \Delta\gamma_y &= \gamma_y^i - \gamma_y^o \\ \Delta\gamma_z &= \gamma_z^i - \gamma_z^o \end{aligned} \tag{3.29}$$

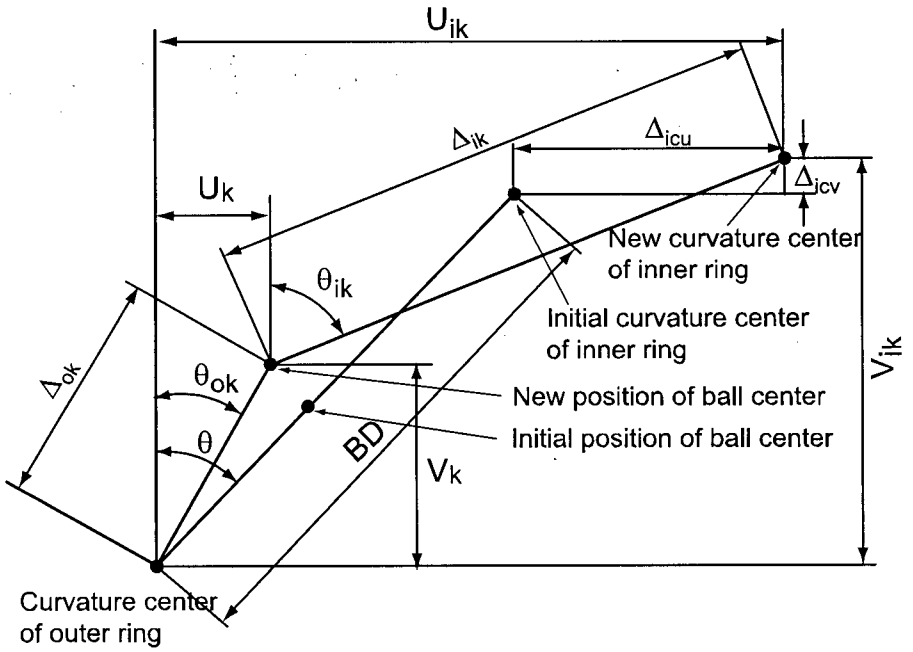

Figure 3-5: Displacement relationships between curvature centers of bearing rings

Due to the use of relative motion of the inner ring with respect to the outer ring, the curvature center of the outer ring groove can be regarded as being fixed. The distance between the curvature centers of the inner and outers ring before deformation of the bearing is:

$$B_d = BD = (f_o + f_i - 1)D \tag{3.30}$$

When the bearing is deformed under the load, the distances between the curvature center of the inner-ring groove and the new position of the ball center, and the center of the outer-ring groove and the new position of the ball center are, respectively:

$$\begin{aligned} \Delta_{ik} &= r_i - D/2 + \delta_{ik} = (f_i - 0.5)D + \delta_{ik} \\ \Delta_{ok} &= r_o - D/2 + \delta_{ok} = (f_o - 0.5)D + \delta_{ok} \end{aligned} \tag{3.31}$$

The changes to the curvature center of the inner ring are:

$$\begin{aligned} \Delta_{icu} &= \Delta\delta_x - \Delta\gamma_z r_{ic}\cos\varphi_k + \Delta\gamma_y r_{ic}\sin\varphi_k \\ \Delta_{icv} &= \Delta\delta_y\cos\varphi_k + \Delta\delta_z\sin\varphi_k \end{aligned} \tag{3.32}$$

The following relations are derived from Figure 3-5:

$$\begin{aligned} \sin\theta_{ok} &= \frac{U_k}{(f_o - 0.5)D + \delta_{ok}} \\ \cos\theta_{ok} &= \frac{V_k}{(f_o - 0.5)D + \delta_{ok}} \\ \sin\theta_{ik} &= \frac{U_{ik} - U_k}{(f_i - 0.5)D + \delta_{ik}} \\ \cos\theta_{ik} &= \frac{V_{ik} - V_k}{(f_i - 0.5)D + \delta_{ik}} \end{aligned} \tag{3.33}$$

where $\varphi_k = 2\pi k/N$, and N is the total number of balls for each bearing.

$$\begin{aligned} U_{ik} &= BD\sin\theta + \Delta\delta_x - \Delta\gamma_z r_{ic}\cos\varphi_k + \Delta\gamma_y r_{ic}\sin\varphi_k \\ V_{ik} &= BD\cos\theta + \Delta\delta_y\cos\varphi_k + \Delta\delta_z\sin\varphi_k \end{aligned} \tag{3.34}$$

where $r_{ic} = D_m/2 + (f_i - 0.5)D\cos\theta$. If $r_{ic} = D_m/2$, the tangential stiffness matrix of the bearing is symmetric. θ is the initial contact angle of the bearing.

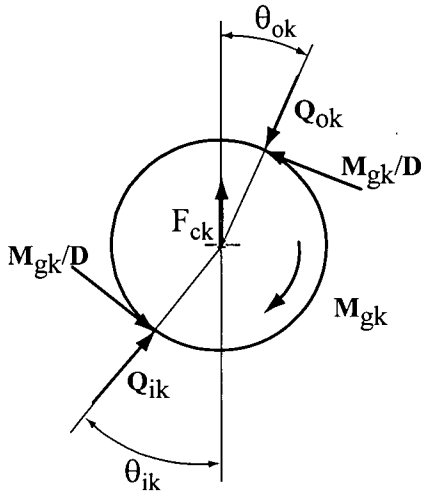

Figure 3-6: The forces acting on the bearing ball

From Figure 3-5 and Figure 3-6, the following equations can be obtained.

Displacement equations:

$$\begin{aligned} &(U_{ik}-U_k)^2+(V_{ik}-V_k)^2-\Delta_{ik}^2=0 \\ &U_k{}^2+V_k{}^2-\Delta_{ok}^2=0 \end{aligned} \tag{3.35}$$

Equilibrium equations for the bearing ball:

$$\begin{aligned} &Q_{ok}\cos\theta_{ok}-\frac{M_{gk}}{D}\sin\theta_{ok}-Q_{ik}\cos\theta_{ik}+\frac{M_{gk}}{D}\sin\theta_{ik}-F_{ck}=0 \\ &Q_{ok}\sin\theta_{ok}+\frac{M_{gk}}{D}\cos\theta_{ok}-Q_{ik}\sin\theta_{ik}-\frac{M_{gk}}{D}\cos\theta_{ik}=0 \end{aligned} \tag{3.36}$$

The four parameters $U_k, V_k, \delta_{ok}, \delta_{ik}$ can be obtained by solving Eq.(3.35) and Eq.(3.36) through the iteration method. For the given initial estimates of variables $\{\delta_k^0\}=\{U_k, V_k, \delta_{ok}, \delta_{ik}\}^T$, the errors $\{\varepsilon_k^0\}=\{\varepsilon_1, \varepsilon_2, \varepsilon_3, \varepsilon_4\}^T$ are represented by the following equations:

$$
\begin{aligned}
&(U_{ik}-U_k)^2+(V_{ik}-V_k)^2-\Delta_{ik}^2=\varepsilon_1\\
&U_k{}^2+V_k{}^2-\Delta_{ok}^2=\varepsilon_2\\
&Q_{ok}\cos\theta_{ok}-\frac{M_{gk}}{D}\sin\theta_{ok}-Q_{ik}\cos\theta_{ik}+\frac{M_{gk}}{D}\sin\theta_{ik}-F_{ck}=\varepsilon_3\\
&Q_{ok}\sin\theta_{ok}+\frac{M_{gk}}{D}\cos\theta_{ok}-Q_{ik}\sin\theta_{ik}-\frac{M_{gk}}{D}\cos\theta_{ik}=\varepsilon_4
\end{aligned}
\tag{3.37}
$$

The Eq. (3.35) and Eq.(3.36) can be solved by applying the following iteration format:

$$
\left\{\delta_k^{(n+1)}\right\}=\left\{\delta_k^{(n)}\right\}-\left[a_{ij}\right]^{-1}\left\{\varepsilon_k^n\right\}\quad(n=0,1,2,\ldots;i,j=1,2,3,4)
\tag{3.38}
$$

a_{ij} is shown in Appendix B.

3.3.3 Centrifugal Force and Gyroscopic Moment

The centrifugal force and gyroscopic moment on the bearing ball can be expressed as [4]:

$$
F_{ck}=\frac{1}{2}mD_m\Omega^2\left(\frac{\Omega_E}{\Omega}\right)_k^2
\tag{3.39}
$$

$$
\mathrm{M_{gk}}=J_b\Omega^2\left(\frac{\Omega_\mathrm{B}}{\Omega}\right)_\mathrm{k}\left(\frac{\Omega_\mathrm{E}}{\Omega}\right)_\mathrm{k}\sin\alpha_\mathrm{k}
\tag{3.40}
$$

The values of $\left(\frac{\Omega_E}{\Omega}\right)_k$ and $\tan\alpha_k$ are given in Table 3-1[5].

Table 3-1: The ratio of orbital speed and spindle speed[5]

Control type	Outer-ring control	Inner-ring control
$\frac{\Omega_E}{\Omega}$	$\frac{1-\lambda\cos\theta_{ik}}{1+\cos(\theta_{ik}-\theta_{ok})}$	$\frac{\cos(\theta_{ik}-\theta_{ok})-\lambda\cos\theta_{ok}}{1+\cos(\theta_{ik}-\theta_{ok})}$
$\tan\alpha_k$	$\frac{\sin\theta_{ok}}{\cos\theta_{ok}+\lambda}$	$\frac{\sin\theta_{ik}}{\cos\theta_{ik}-\lambda}$

$$\left(\frac{\Omega_B}{\Omega}\right)_k = \frac{-1}{\left(\frac{\cos\theta_{ok} + \tan\alpha_k \sin\theta_{ok}}{1+\lambda\cos\theta_{ok}} + \frac{\cos\theta_{ik} + \tan\alpha_k \sin\theta_{ik}}{1-\lambda\cos\theta_{ik}}\right)\lambda\cos\alpha_k}$$

Whether outer-ring control or inner-ring control exists depends on the following conditions listed in Table 3-2 [5].

Table 3-2: Criterion of outer ring control or inner ring control [5]

Outer-ring control	$Q_{ok} a_{ok} \mathbf{E}_{ok} \cos(\theta_{ik} - \theta_{ok}) > Q_{ik} a_{ik} \mathbf{E}_{ik}$
Inner-ring control	$Q_{ik} a_{ik} \mathbf{E}_{ik} \cos(\theta_{ik} - \theta_{ok}) > Q_{ok} a_{ok} \mathbf{E}_{ok}$

Under certain conditions of operation, a ball may be completely out of contact with the inner ring. As a result, the outer ring contact angle θ_{ok} and gyroscopic moment M_{gk} are zero. The force Q_{ok} is then equal to the centrifugal force F_{ck}.

Loss of inner-ring contact will occur when the following condition is satisfied:

$$U_{ik}^{\ 2} + \left[V_{ik} - (f_o - 0.5D) - K_o^{-2/3} F_{ck}^{2/3}\right]^2 \le \left[(f_i - 0.5)D\right]^2$$

3.3.4 Forces Acting on the Bearing Rings

In order to obtain the bearing stiffness, the relationship between the forces acting on the bearing rings and the displacement of the bearing rings has to be established. The forces acting on the inner ring of the bearing are:

$$
\begin{aligned}
F_{xi} &= \sum_{k=1}^{N}\left(Q_{ik}\sin\theta_{ik} + \frac{M_{gk}}{D}\cos\theta_{ik}\right)\\
F_{yi} &= \sum_{k=1}^{N}\left(Q_{ik}\cos\theta_{ik} - \frac{M_{gk}}{D}\sin\theta_{ik}\right)\cos\varphi_k\\
F_{zi} &= \sum_{k=1}^{N}\left(Q_{ik}\cos\theta_{ik} - \frac{M_{gk}}{D}\sin\theta_{ik}\right)\sin\varphi_k\\
M_{yi} &= +\sum_{k=1}^{N}\left\{r_{ic}\left(Q_{ik}\sin\theta_{ik} + \frac{M_{gk}}{D}\cos\theta_{ik}\right) - f_i M_{gk}\right\}\sin\varphi_k\\
M_{zi} &= -\sum_{k=1}^{N}\left\{r_{ic}\left(Q_{ik}\sin\theta_{ik} + \frac{M_{gk}}{D}\cos\theta_{ik}\right) - f_i M_{gk}\right\}\cos\varphi_k
\end{aligned}
\tag{3.41}
$$

The forces acting on the outer ring of the bearing are:

$$
\begin{aligned}
F_{xo} &= -\sum_{k=1}^{N}\left(Q_{ok}\sin\theta_{ok} + \frac{M_{gk}}{D}\cos\theta_{ok}\right)\\
F_{yo} &= \sum_{k=1}^{N}\left(-Q_{ok}\cos\theta_{ok} + \frac{M_{gk}}{D}\sin\theta_{ok}\right)\cos\varphi_k\\
F_{zo} &= \sum_{k=1}^{N}\left(-Q_{ok}\cos\theta_{ok} + \frac{M_{gk}}{D}\sin\theta_{ok}\right)\sin\varphi_k\\
M_{yo} &= -\sum_{k=1}^{N}\left\{r_{oc}\left(Q_{ok}\sin\theta_{ok} + \frac{M_{gk}}{D}\cos\theta_{ok}\right) + f_o M_{gk}\right\}\sin\varphi_k\\
M_{zo} &= +\sum_{k=1}^{N}\left\{r_{oc}\left(Q_{ok}\sin\theta_{ok} + \frac{M_{gk}}{D}\cos\theta_{ok}\right) + f_o M_{gk}\right\}\cos\varphi_k
\end{aligned}
\tag{3.42}
$$

where $r_{oc} = D_m/2 - (f_o - 0.5)D\cos\theta$

All these forces are finally and implicitly expressed as functions of displacements of bearing rings, which are linked to the displacement of the spindle shaft and housing at the corresponding bearing locations.

3.3.5 Stiffness Matrix of Bearings

The following stiffness matrix of the bearing is obtained by finding the derivatives of forces with respect to displacement. The details of the derivations are presented in Appendix C.

$$\left[K_B^T\right]=\begin{bmatrix} K_{II}^T & K_{IO}^T \\ K_{IO}^T & K_{OO}^T \end{bmatrix}=\begin{bmatrix} K_I^T & -K_I^T \\ -K_O^T & K_O^T \end{bmatrix} \tag{3.43}$$

3.4 System Equations of the Spindle System

By assembling equations of the disk, spindle shaft/housing, and bearings, the following general non-linear dynamic equation for the spindle-bearing system is established:

$$[M]\{\ddot{x}\}+[C]\{\dot{x}\}+\{R(x)\}=\{F(t)\} \tag{3.44}$$

where $[M]=[M^b]+[M^d]$, $[C]=[G^b]+[G^d]+[C^s]$, $\{F(t)\}=\{F^b\}+\{F^d\}$, $[C^s]$ is the structural damping, which can be obtained from experimental modal analysis, and $\{R(x)\}$ is the internal force of the system, which depends on displacement $\{x\}$. The equivalent stiffness term implicitly included in the term $\{R(x)\}$ depends on displacement $\{x\}$, which is in turn affected by stiffness. The dependency of the stiffness matrix contained in $\{R(x)\}$ on displacement is the root cause of the nonlinearity in the spindle system.

The Newton-Raphson method is used to solve Eq.(3.44). The incremental finite element equilibrium equation is obtained as follows [70]:

$$[M]^{t+\Delta t}\{\ddot{x}\}^{(i)}+[C]^{t+\Delta t}\{\dot{x}\}^{(i)}+[K]\{\Delta x\}^{(i)}={}^{t+\Delta t}\{F(t)\}-{}^{t+\Delta t}\{R\}^{(i-1)} \tag{3.45}$$

where $[K]=[K^b]+[K^b]_P+[K_B^T]-\Omega^2[M^b]_C$, ${}^{t+\Delta t}\{\ddot{x}\}^{(i)}$, ${}^{t+\Delta t}\{\dot{x}\}^{(i)}$, and ${}^{t+\Delta t}\{x\}^{(i-1)}+\{\Delta x\}^{(i)}$ are the approximations of the accelerations, velocities, and displacements obtained in the i^{th} iteration, respectively. $\{\Delta x\}^{(i)}$ is the displacement increment at the i^{th} iteration. ${}^{t+\Delta t}\{F(t)\}$ is the force at the time $t+\Delta t$. ${}^{t+\Delta t}\{R\}^{(i-1)}$ is the internal force corresponding to the displacement ${}^{t+\Delta t}\{x\}^{(i-1)}$.

3.5 Summary

In this chapter, general mathematical models are developed for the rigid disk, rotating shaft, angular contact ball bearing, and the spindle-bearing system. The equations of motion for the rotating disk and Timoshenko beam with centrifugal forces, gyroscopic moments, and axial force are established in a simple way that has not been reported in the literature. The

finite element method is used to discretize the continuous beam equations. A nonlinear finite element is formulated for angular contact ball bearings by using the most complete bearing model, i.e., Jones' bearing model, which leads to the standard nonlinear equations in matrix form for the spindle-bearing system.

Chapter 4

Verification of the Spindle-Bearing Model

Two examples are given in this chapter to verify the proposed methods. One is a simple rotor supported by two angular contact ball bearings, analyzed by Edmund with the programs NASBBAN [64] and BEACON [65] developed by SKF for analyzing flexible bearing shaft systems. The other is an instrumented spindle, on which the experiment is conducted for both static deformation and dynamic response, such as time history of displacement and frequency response functions (FRF) under different preloads.

4.1 A Rotor Supported by Two Bearings

4.1.1 Problem Specifications

Figure 4-1 shows a rotor supported by two angular contact ball bearings preloaded with a force of 500N. An external static force of 600N is applied at the middle of the rotor in the radial direction. The deflections, bearing stiffness, and distribution of the contact forces on the bearing balls are simulated and compared with results in the literature [64]. The materials and geometry of the rotor and bearings are listed in Table 4-1.

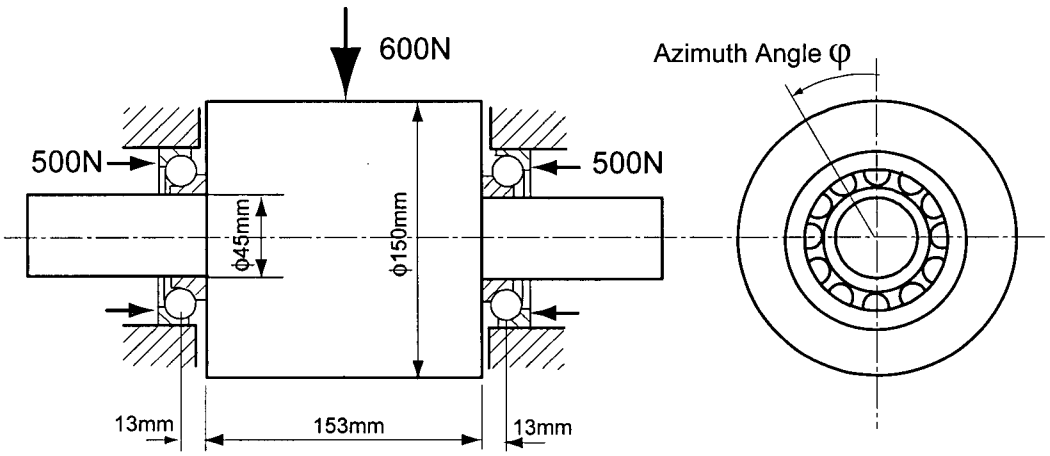

Figure 4-1: A rotor supported by two angular contact ball bearings.

4.1.2 Model Description

The finite element model is shown in Figure 4-2. In order to compare the results with those in literature [64], the same number of elements, i.e., four elements between the two

bearings, is used for the rotor. The model proposed in this thesis can include the deformation of the bearing housings. The bearing housings are therefore also modeled here, but they are fixed in the finite element model. The inner ring of the bearing is fixed to the rotor, which is represented by a square box, while the outer ring can slide along the bearing housing, which is marked by a circle. The diagonal lines on the bearings indicate the directions of contact angles.

Table 4-1: Material and geometric data for the rotor and bearings

Modulus of elasticity for the rotor and bearings	206 GPa
Poisson ratio for the rotor and bearings	0.3
Number of balls for each bearing	12
Bearing ball diameter	17.7 mm
Bearing pitch diameter	72.5 mm
Contact angle	40°
Curvature radius of the inner ring	9.16 mm
Curvature radius of the outer ring	9.38 mm

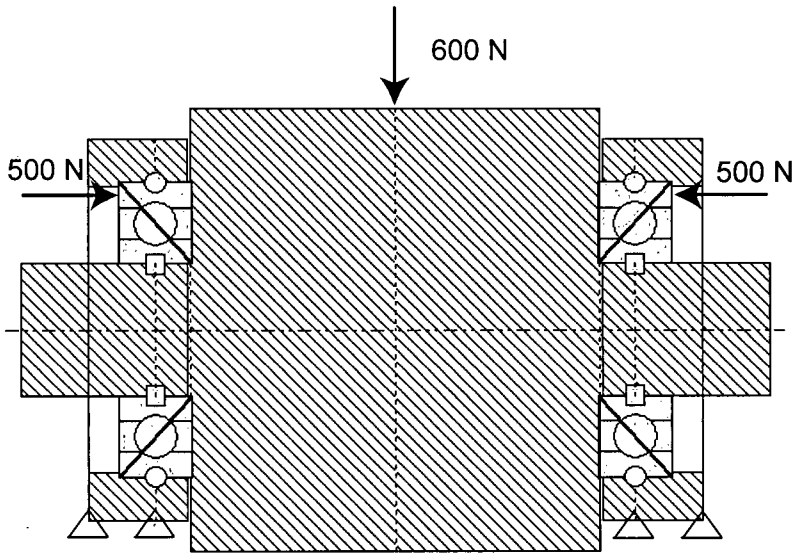

Figure 4-2: FE model of the rotor presented in SpindlePro®

4.1.3 Simulation Results

Due to the symmetry of the structures and applied forces, both bearings have the same deformation, stiffness, and contact forces. The comparison between the calculated bearing displacements is given in Table 4-2. Contact angles and contact forces are listed in Table 4-3 and Table 4-4, respectively. The simulated results in this thesis are in good agreement with those in the literature.

Table 4-2: Comparison of bearing displacements

	Bearing displacement [μm]		
	Thesis result	NASBBAN [64]	BEACON [65]
Axial displacement	4.179	4.2	4.0
Radial displacement at the middle of the rotor	2.797	2.8	3.0

Table 4-3: Comparison of bearing contact angles

Ball position angle [deg]*	Contact angles [deg]		
	Thesis result	NASBBAN [64]	BEACON[65]
0	40.341	40.34	40.3
30	40.324	40.33	40.3
60	40.279	40.28	40.3
90	40.216	40.22	40.2
120	40.154	40.15	40.2
150	40.108	40.11	40.1
180	40.092	40.09	40.1
210	40.108	40.11	40.1
240	40.154	40.15	40.2
270	40.216	40.22	40.2
300	40.279	40.28	40.3
330	40.324	40.33	40.3

* The ball position is defined in Figure 4-1.

Table 4-4: Comparison of bearing contact force [N]

Ball position angle [deg]	Thesis result	NASBBAN [64]	BEACON[65]
0	6.556	6.6	7
30	11.312	11.3	11
60	28.082	28.1	28
90	57.982	58.0	58
120	94.370	94.4	94
150	124.541	124.5	125
180	136.269	136.3	136
210	124.541	124.5	125
240	94.370	94.4	94
270	57.982	58.0	58
300	28.082	28.1	28
330	11.312	11.3	11

4.2 Spindle Analysis

Figure 4.3 shows an experimental spindle designed and built by the research partner Siemens-Weiss Spindle GmbH. The spindle has a standard CAT 40 tool-holder interface, and is designed to operate up to 15,000 rev/min with a 15kW motor connected to the shaft by a pulley-belt system. The axial displacements relative to the spindle housing at the spindle nose are simulated and measured by both the displacement sensors integrated to the spindle and an external laser displacement sensor. The natural frequencies and frequency response functions under different preloads are predicted and measured by performing impact-hammer tests when the spindle is at rest. The influence of the tool-holder interface on the dynamics of the spindle system is also discussed in this section.

4.2.1 Description of the Spindle

The spindle has five bearings in overall back-to-back configuration. Three bearings are placed in a floating bearing housing, which can be moved by a hydraulic preload unit. The preload mechanism works as follows. Through a hydraulic pump, the preload is applied to the rear bearings by the floating bearing housing. At the same time, the force is transmitted to

the spindle shaft by the nut, then the spindle shaft moves towards the rear. As a result, the force is applied to the front bearings through step A of the spindle shaft. The spindle housing prevents the spindle shaft from moving further to the rear by step B of the spindle housing. The whole spindle is self-balanced in the axial direction under the preload.

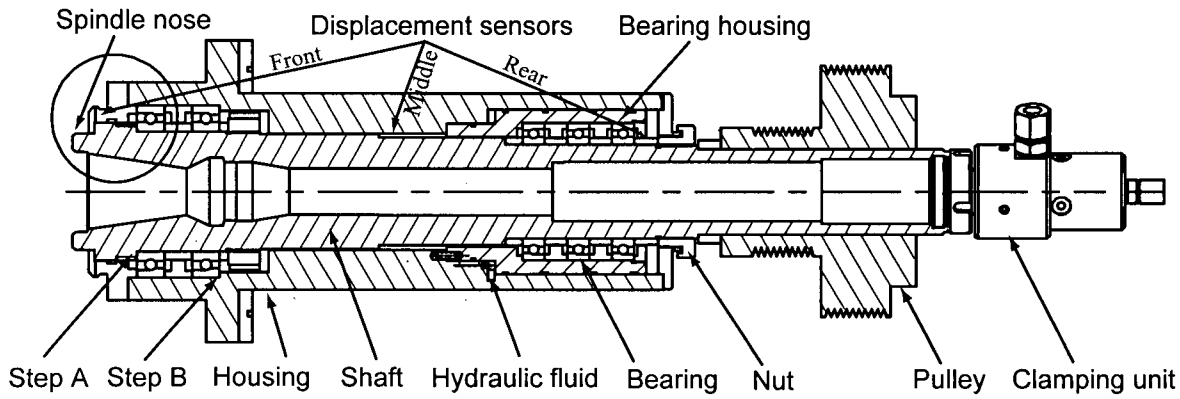

Figure 4-3: A spindle system with adjustable preload mechanism

The spindle is equipped with six inductive displacement sensors in two radial directions 90 degrees to one another at three locations (i.e., the front, middle, and the rear), and two sensors in axial directions in the front. The details for the front displacement sensors in both the axial and radial directions are illustrated in Figure 4-4.

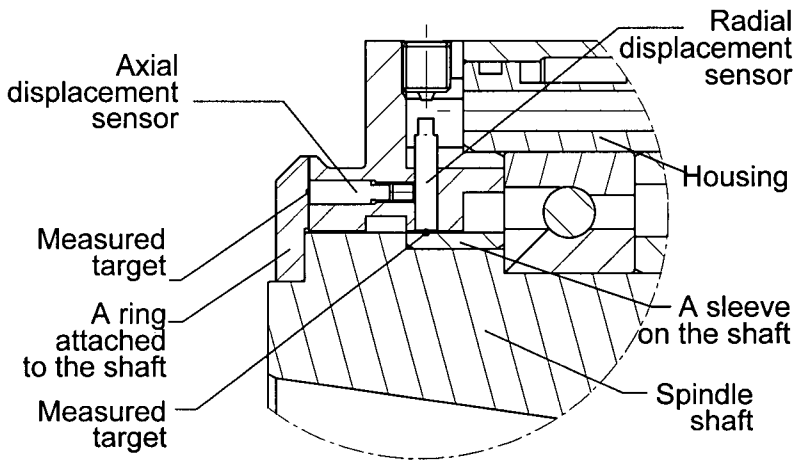

Figure 4-4: Front displacement sensor setup

4.2.2 Finite Element Model

A general finite element model of the spindle-bearing system is presented in Figure 4-5. The Timoshenko beam is used to model the spindle shaft and housing. It would be better if solid elements are used for the housing, but this would make the model much more complex. Because strength is not the concern in spindle design, and the beam element is still accurate for the dynamic analysis of thick beams, the Timoshenko beam is a suitable element to be used in spindle analysis. In the FE model, the black dots represent nodes, and each node has three translational displacements in the X, Y, and Z axes, and two rotations about the Y and Z axes. The pulley is modeled as a rigid disk, the bearing spacer as a bar element, and the nut and sleeve as a lumped mass. The spindle has two front bearings (no.1 and no.2) in tandem and three bearings (no.3 to no.5) in tandem at the rear. The preload is applied on the outer ring defined as node A3, which can move along the spindle housing with nodes A4 and A5. The forces are transmitted to inner rings B3 to B5 through bearing balls, then to the spindle shaft through inner ring B5, which is fixed to the spindle shaft. Finally, the forces are transferred to the front bearings by inner ring B1, which is also fixed to the spindle shaft, then to the housing by outer ring A2, which is fixed to the housing. As a result, the whole spindle is self-balanced in the axial direction under the preload. An initial preload is applied during the assembly, and can be adjusted later through the hydraulic unit. The inner ring and outer ring of the bearing are related by nonlinear bearing equations, from which bearing stiffness is obtained by solving equations of the system. The overall system is represented in FE software developed in-house and registered under SpindlePro® by UBC.

The finite element model presented in SpindlePro® [66] is shown in Figure 4-6.

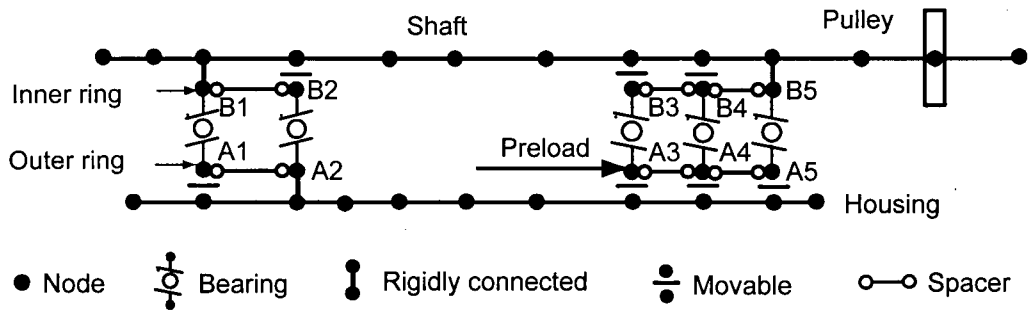

Figure 4-5: Finite element model for spindle-bearing system

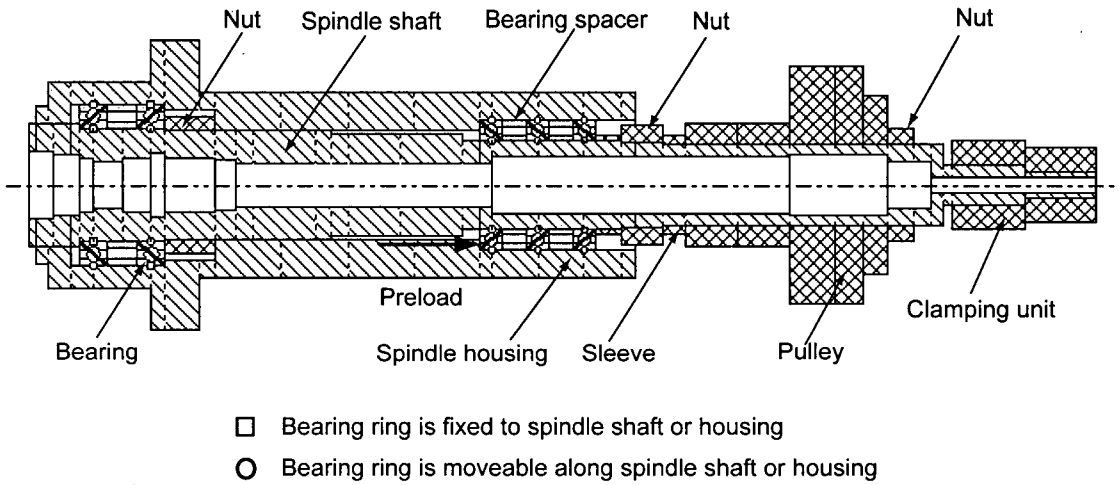

Figure 4-6: Finite element model presented in SpindlePro®

4.2.3 Axial Displacements at the Spindle Nose

The axial displacements relative to the spindle housing at the spindle nose are measured by the inductive displacement sensor integrated into the spindle, and an external laser displacement sensor. The experimental setup is shown in Figure 4-7 and Figure 4-8. As mentioned in Section 4.2.1, the whole spindle is self-balanced in the axial direction under the preload. Therefore, the displacement of the spindle shaft in the axial direction can be measured by simply fixing the spindle housing on a table so that it cannot move under the preload. The preload is applied by a hydraulic unit as shown in Figure 4-7. The spindle already has an initial preload produced during assembly, and it is estimated as follows. First, the axial deformations of the spindle nose are measured under different preloads. Then, the preloads plus the same estimated initial preload are applied to the finite element model to obtain the simulated displacements. By trying to match the two curves from both measurement and simulation, the initial preload is predicted as 300N.

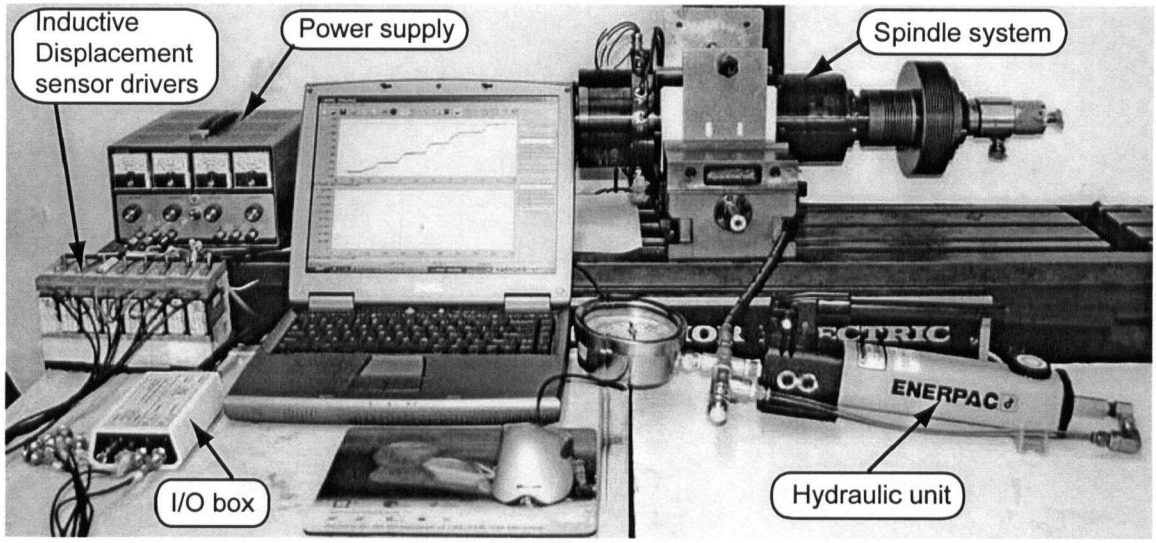

Figure 4-7: Displacement measurement setup with inductive displacement sensors

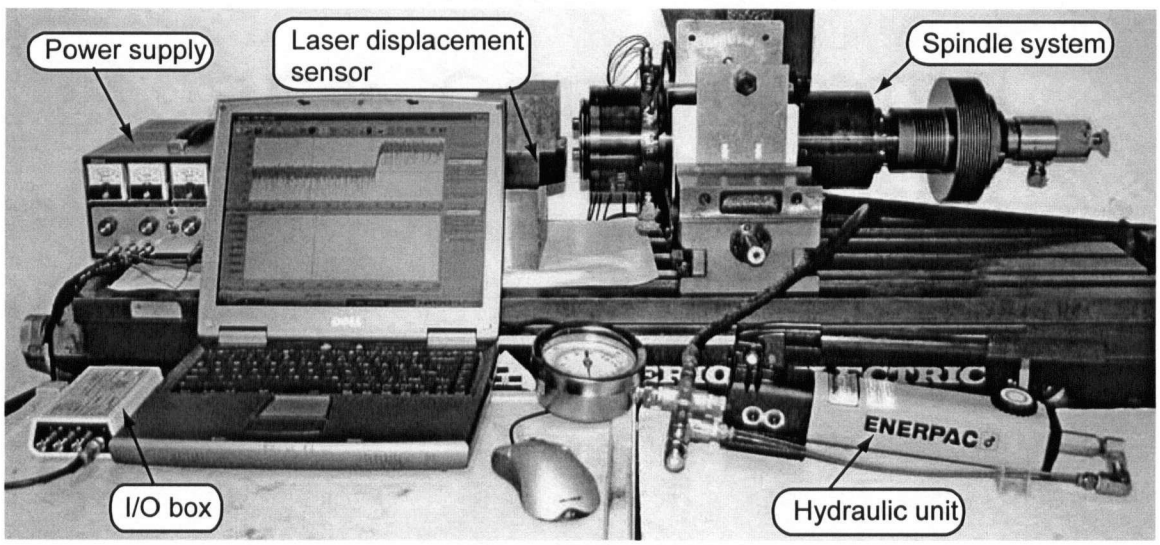

Figure 4-8: Displacement measurement setup with the laser displacement sensor

Figure 4-9 and Figure 4-10 show the measured axial deformations of the spindle nose under different preloads. The deformations are mainly from the front bearings, because the deformations are the relative displacements between the spindle nose and the housing, which can be explained through Figure 4-3 and Figure 4-4.

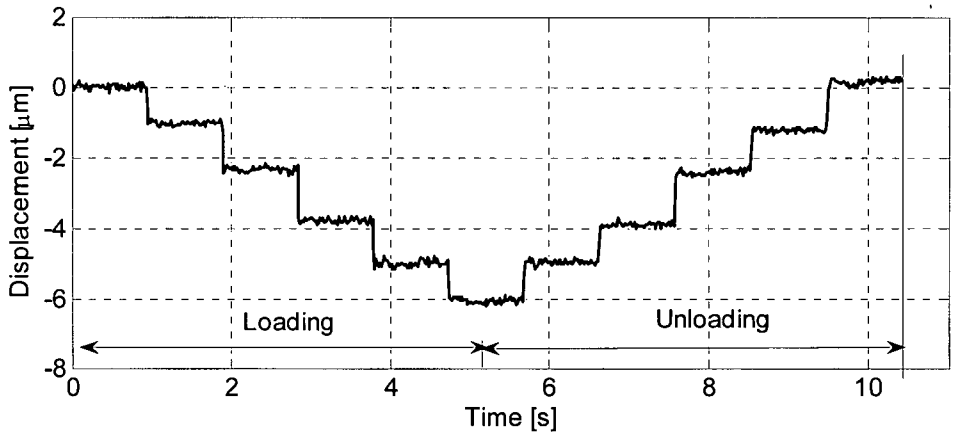

Figure 4-9: Axial displacement history at the spindle nose under different preloads measured by the external laser displacement sensor (displacement transition between loads is removed)

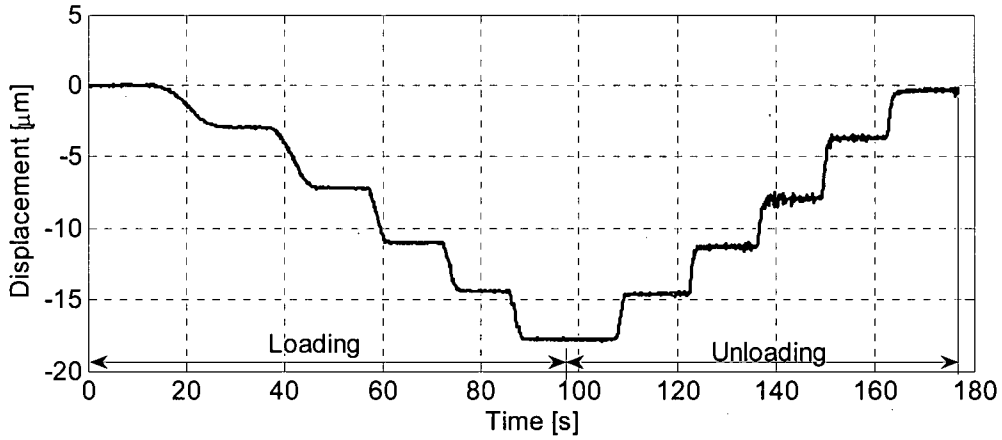

Figure 4-10: Axial displacement history at the spindle nose under different preloads measured by inductive displacement sensor (Lion sensor) inside the spindle

It is shown that the axial displacement measured by the external laser-displacement sensor is very similar to that measured by the inductive displacement sensor, except for the magnitude. The laser-displacement sensor was already calibrated, and the measured displacement values matched the simulation quite well. Therefore, the inductive displacement sensor was calibrated through the laser sensor. The axial displacements from both simulation and measurement are plotted in Figure 4-11 and Figure 4-12. Since accurate calculation of displacement requires correct computation of contact angles, contact forces,

stiffness matrix of bearings, and a correct solution algorithm, the agreement in displacements is a good overall check for the model.

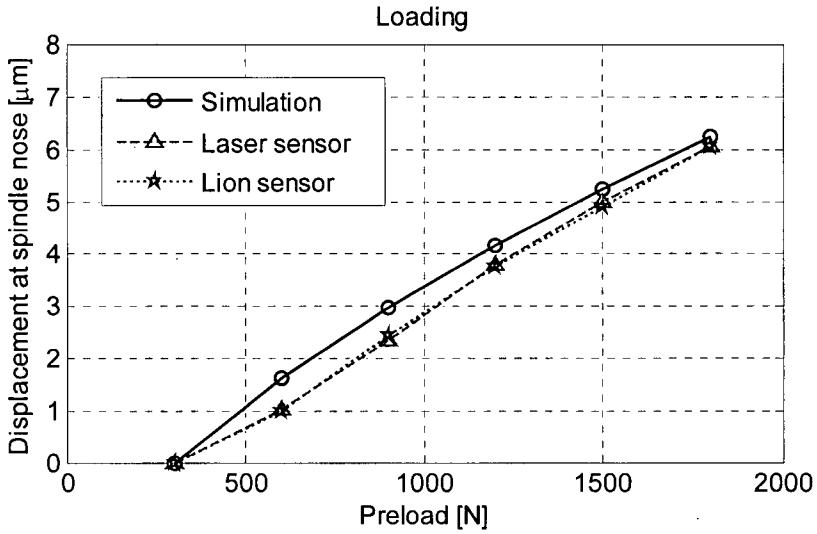

Figure 4-11: Axial displacements at the spindle nose under different preloads (loading)

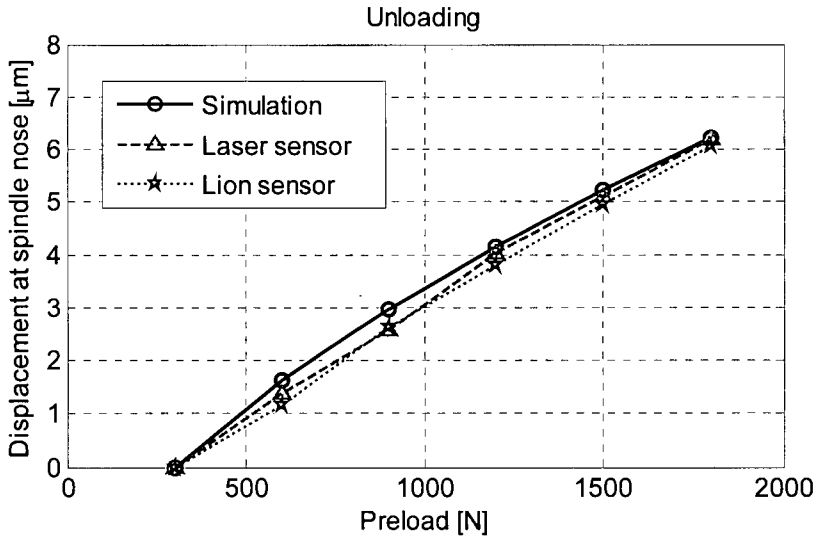

Figure 4-12: Axial displacements at the spindle nose under different preloads (unloading)

4.2.4 Prediction of Bearing Stiffness, Contact Angles, and Contact Forces

Two types of FAG bearings are used in this spindle, the XCS71914E in the front of the spindle close to spindle nose end, and the XCS71911E in the rear. The bearings are

numbered from the first front bearing to the last rear one close to the pulley wheel end, starting with No.1. The changes of the bearing stiffness as a function of preload are shown in Figure 4-13. Bearing stiffness cannot be measured directly, but if the static and dynamic simulations (e.g., displacement of the spindle nose, natural frequencies, frequency response functions, and time history response) match those from experiments, the bearing stiffness estimations should be correct. The bearing stiffness, displacements, and dynamics of the spindle are all coupled as a system, and the boundary conditions are also reasonably modeled.

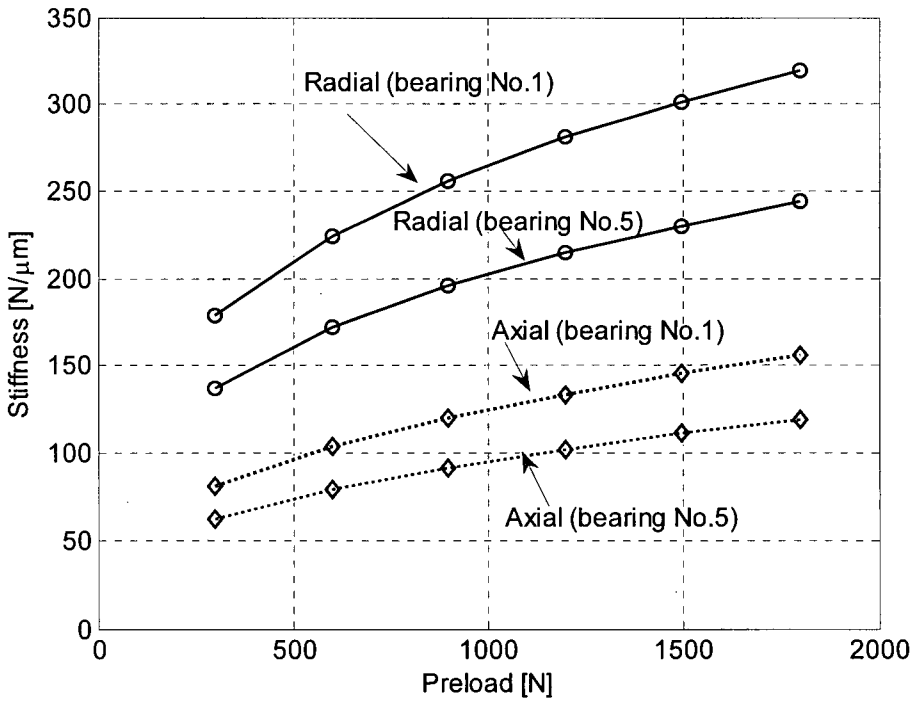

Figure 4-13: The influence of bearing preload on bearing stiffness

Figure 4-14 and Figure 4-15 demonstrate the simulated contact angles and contact forces under different preloads when the spindle is not rotating. When only the preload is applied, the contact angles and forces are the same for all balls in the same bearing. The simulation results show that the contact forces on bearing balls change linearly with the preload. At lower preloads, the stiffness and contact angles are nonlinear, but they become more linear as the preload increases.

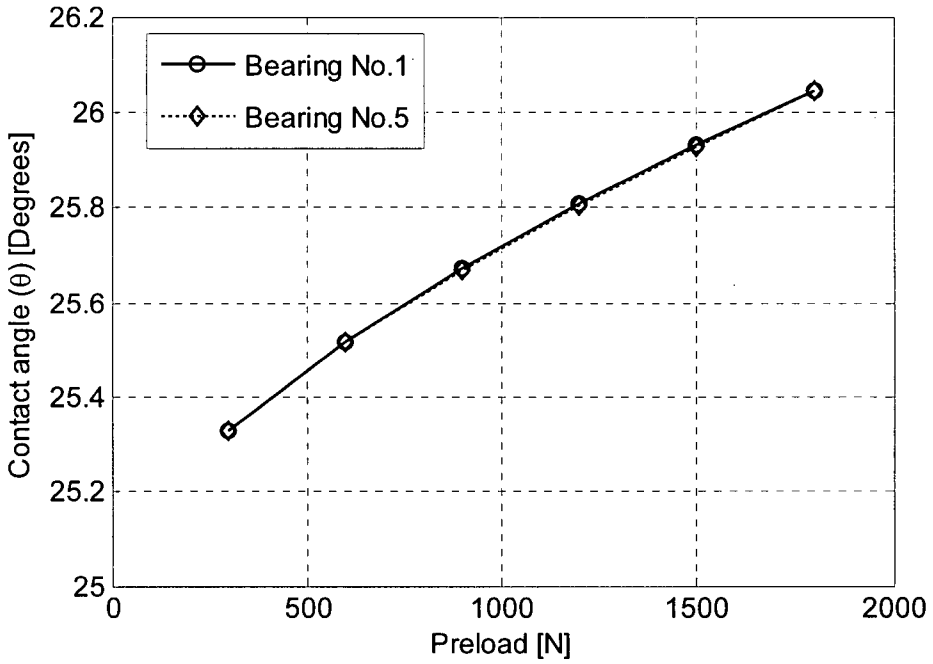

Figure 4-14: The influence of bearing preload on bearing contact angles

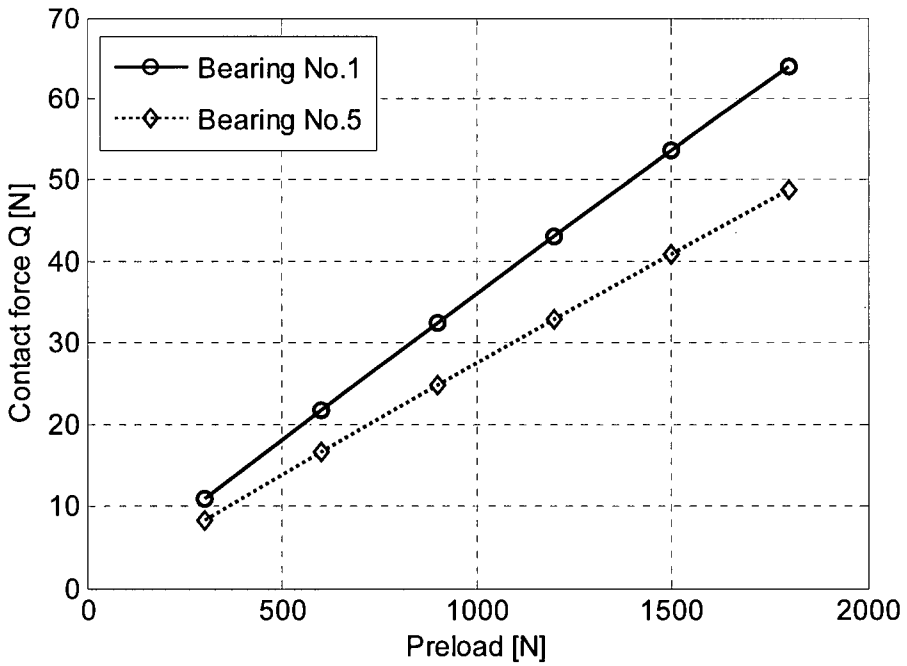

Figure 4-15: The influence of bearing preload on bearing contact forces

4.2.5 Time and Frequency Response Test

The acceleration response, natural frequencies, and frequency response functions were measured by performing the impact-hammer test. The spindle was suspended on the crane using elastic strings as a free-free system, illustrated in Figure 4-16. An impact force was applied at one key of the spindle nose, while the accelerometer is attached to the other key of the nose, as shown in Figure 4-17.

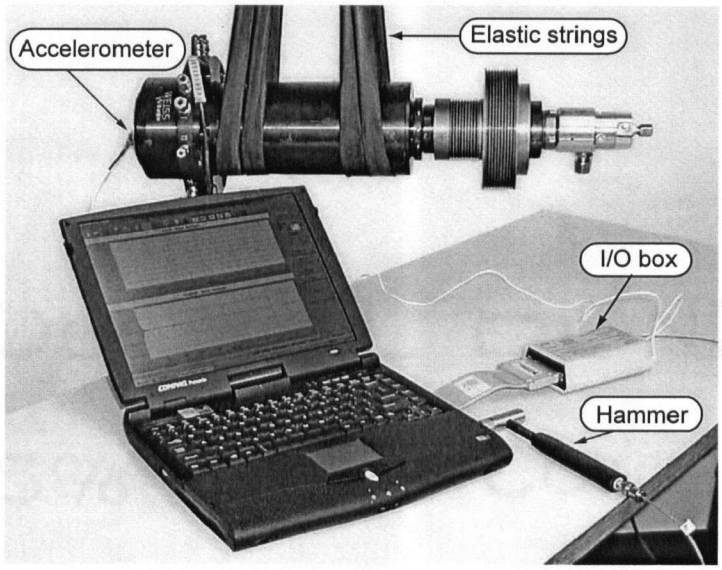

Figure 4-16: Experimental setup

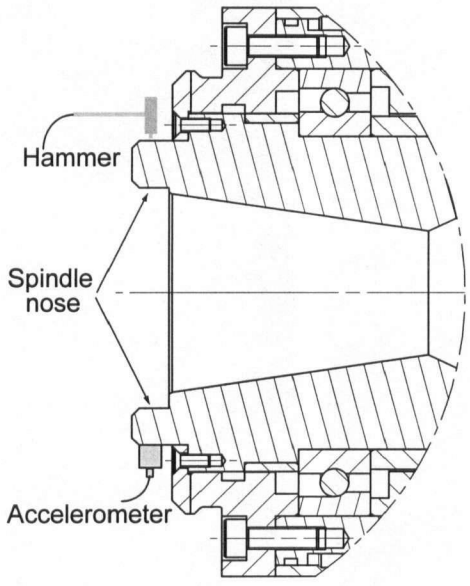

Figure 4-17: Locations of impact force and accelerometer

Figure 4-18 shows the measured time history of an impact force applied at the spindle nose in the radial direction while the bearings are preloaded with a force at 900N. The same impact force is used in the simulation.

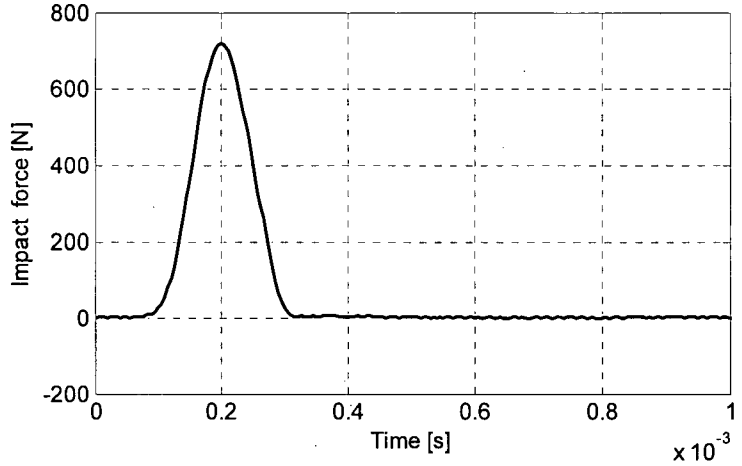

Figure 4-18: Impact force in radial direction applied at the spindle nose

The time response histories of radial acceleration from both simulation and experiment are shown in Figure 4-19, are in good agreement. Experimentally identified modal damping ratios of 1.87 % and 1.90% are used for the first and fourth modes, respectively (i.e., the two dominant modes), and 3% is used for the rest. The measured and predicted frequency response functions (FRF) are shown in Figure 4-20, and are also in good agreement.

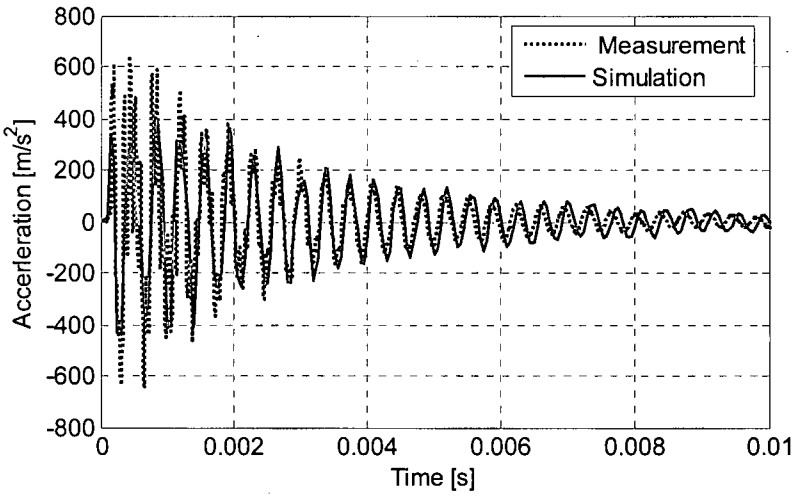

Figure 4-19: Measured and simulated acceleration response in radial direction at the spindle nose under an impact force

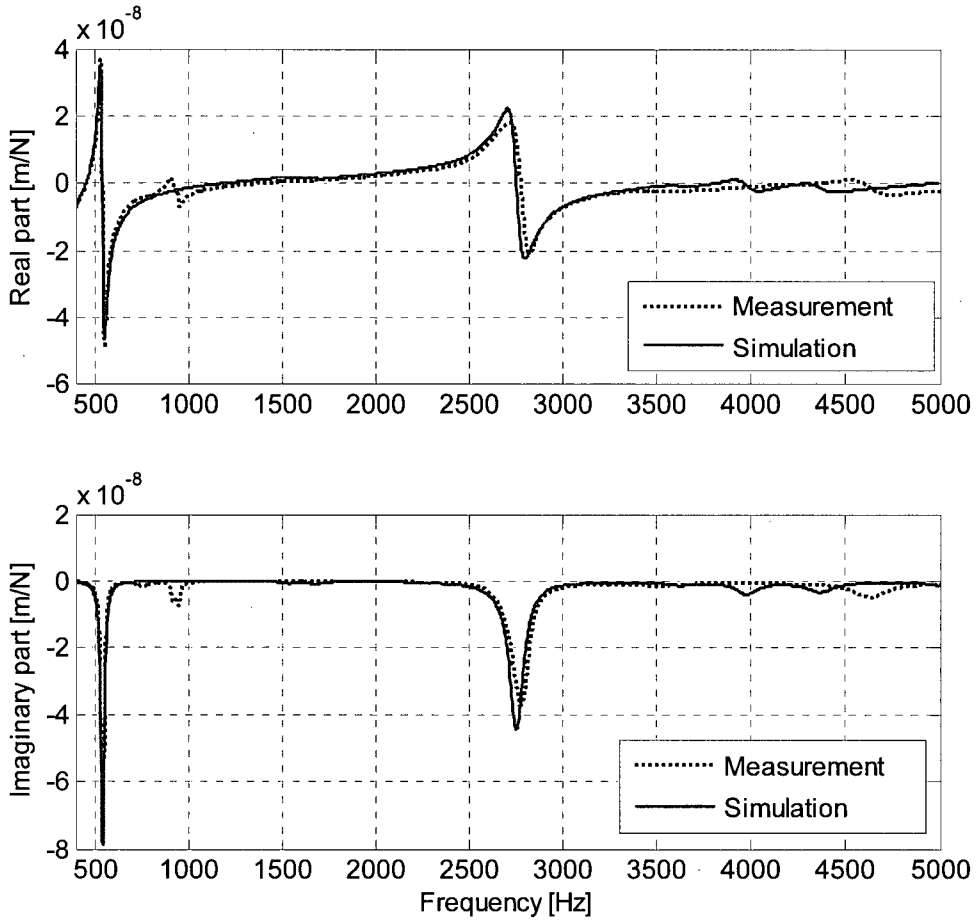

Figure 4-20: Measured and simulated frequency response function in the radial direction at the spindle node

The FRF below 400Hz is not shown in the plot, because there are no other modes except for the rigid body mode for the free-free structure.

4.2.6 The Influence of Bearing Preload on Natural Frequencies and FRF

The influence of preload on the measured FRF of the spindle system is illustrated in Figure 4-21. Figure 4-22 shows the influence of bearing preload on the natural frequencies. The natural frequency increases from 2610 Hz to 2960 Hz as the preload is increased from 300 N to 1800 N, respectively.

The results indicate that the preload barely affects the first mode, while shifting the higher mode upward. The biggest simulation error occurs at the lowest preload case for the

second dominant mode. These two modes are most dominant at the spindle nose, which has the greatest influence on machining stability. The proposed model is able to accurately predict the influence of preload, which is quite important in designing and operating the spindle at chatter-vibration-free spindle speeds.

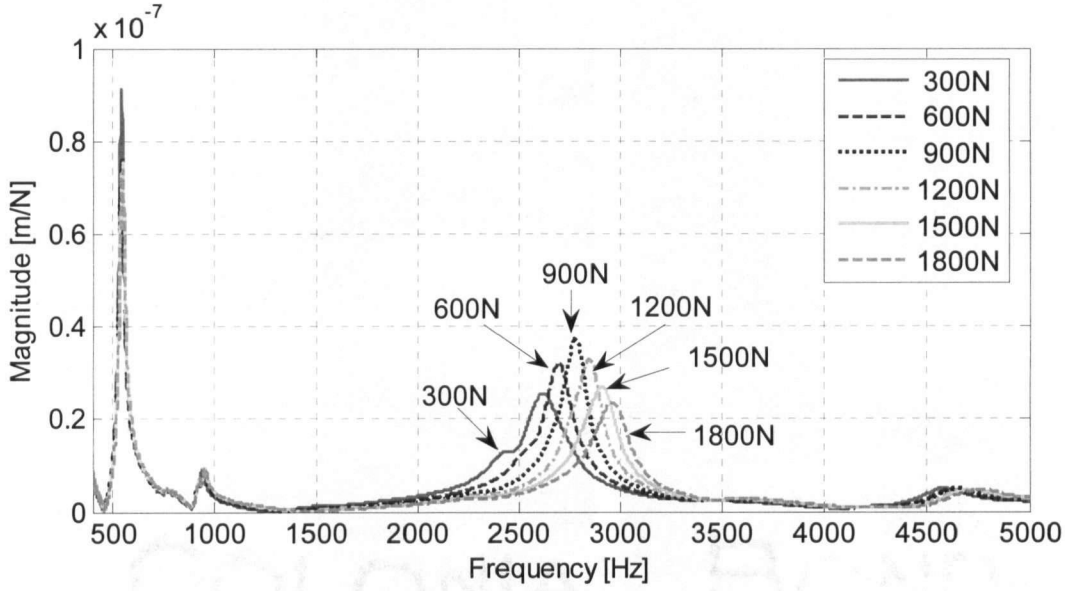

Figure 4-21: Measured FRF under different bearing preloads

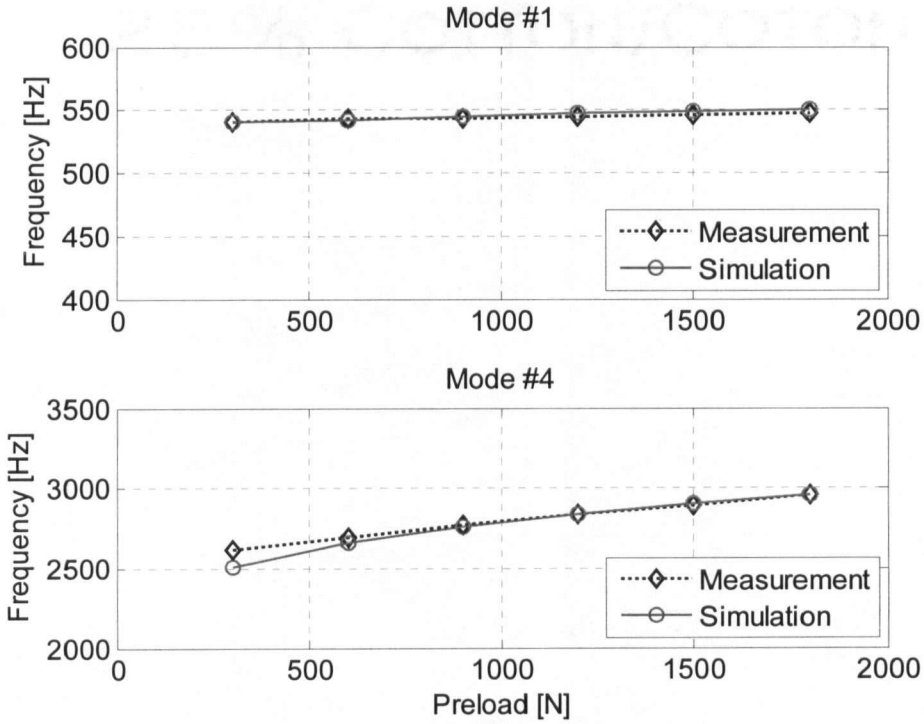

Figure 4-22: The influence of bearing preload on natural frequencies

4.2.7 The Influence of the Tool-holder on Spindle Dynamics

In practice, the interface of the tool-holder and the spindle shaft is usually the main source of vibrations. In this section, a shrink-fit tool-holder, CV40TT20M400 (see Figure 4-23), is used to study its influence on spindle dynamics. The tool-holder is rigidly connected to the spindle shaft, and the spindle is under free-free boundary conditions in simulation. An initial preload of 300N is used in this analysis. As shown in Figure 4-22, the simulation error for this preload is the biggest in the whole range of the applied preload. The simulation and measurement are conducted in two scenarios, without the tool-holder and with the tool-holder on the spindle.

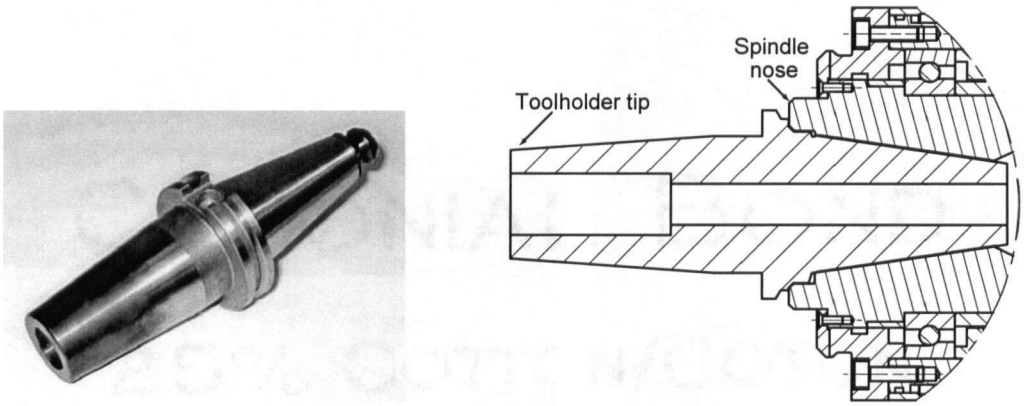

Figure 4-23: A shrink fit tool-holder and its connection to the spindle

The FRFs at the spindle nose are plotted in Figure 4-24. When the tool-holder is not on the spindle, the errors for the first and second dominant frequencies are 0.5% and 3%, respectively. The frequency errors increase to 2% and 5%, respectively, with the tool-holder on the spindle. The simulated results are smaller than the experimental results for both cases.

The tool-holder adds extra mass and makes the spindle longer, which leads to a more flexible spindle. Frequencies therefore drop, but not due to the interface of the tool-holder and the spindle shaft. The first dominant frequency drops very little, since it comes from the rear part of the spindle, i.e., the pulley, while the second mode drops from 2610 Hz to 1827 Hz, since it comes from the front part of the whole spindle. The simulated mode shapes are shown in Figure 4-26.

In conclusion, rigid connection between the tool-holder and the spindle shaft can be used in spindle analysis, which is further demonstrated in chapter 5.

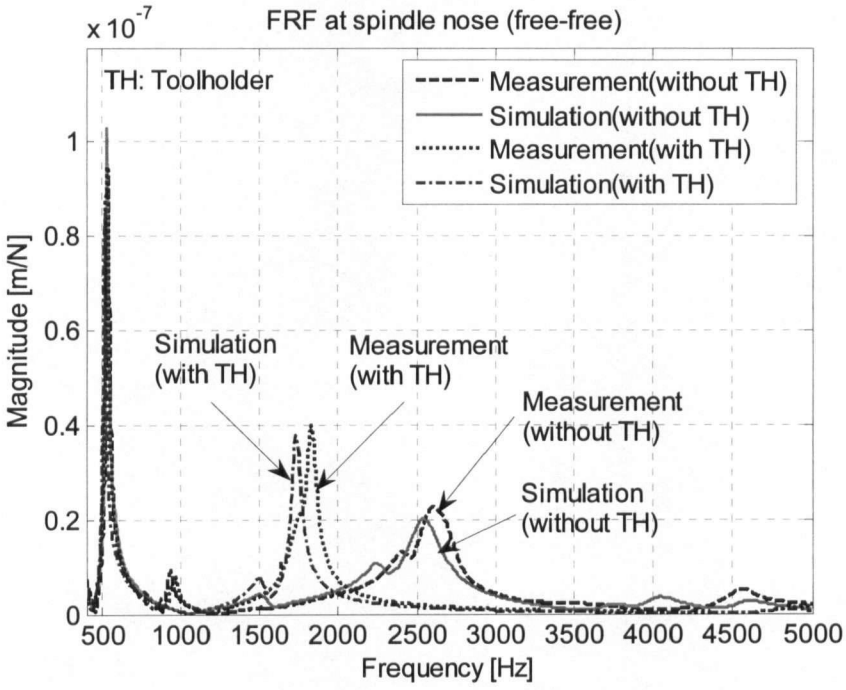

Figure 4-24: FRF at the spindle nose under free-free boundary conditions

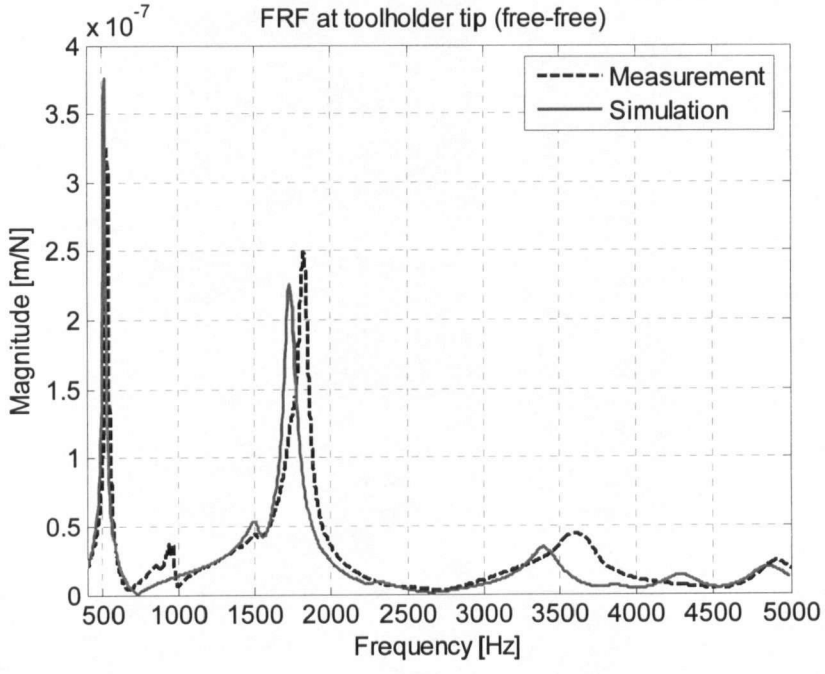

Figure 4-25: FRF at the tool-holder tip under free-free boundary conditions

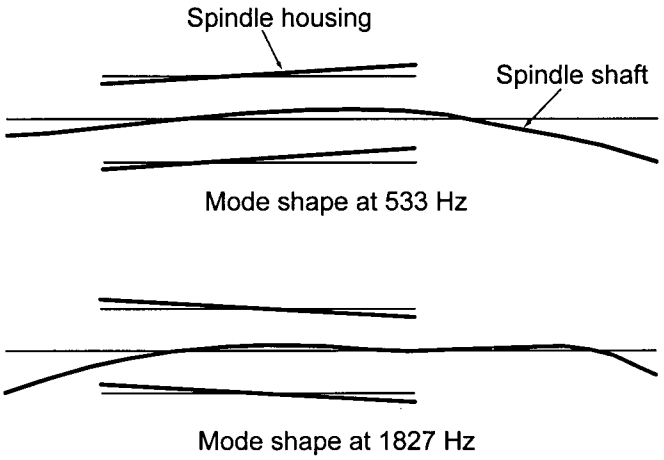

Figure 4-26: Mode shapes for two dominant modes with the tool-hold on the spindle

4.3 Summary

In this chapter, models for the angular contact ball bearing and spindle-bearing system are verified by a standard benchmark simulation and by experiments conducted on an industrial-sized spindle designed for this research. The time history of acceleration response, natural frequencies, and frequency response functions are accurately predicted under impact forces, and are in good agreement with the experiments. These results also indirectly validate the bearing model. Both simulation and experimental results show that bearing stiffness and natural frequencies increase with the preload. The influence of tool-holder interface on the spindle dynamics is also discussed. Results show that the rigid connection between the shrink-fit tool-holder and the spindle shaft can be adopted in modeling the spindle system.

Chapter 5
Modeling of Spindle Machine Tool Systems

5.1 Overview

In chapter 4, the proposed model is verified on the spindle under the free-free boundary conditions. The dynamics of the spindle changes, however, once the spindle is installed on the machine tool. In order to simulate cutting operations, the effects of the machine tool on the spindle system must be included in the model. Figure 5-1 shows a vertical milling center FADAL VMC2216 with an experimental spindle on it. The spindle moves vertically with the spindle head, which travels on the guideway attached to the machine column. The spindle head acts like a cantilever beam elastically supported on the column due to the contact with the guideway. Therefore, the flexibility of the spindle mounting has to be reflected in the model of the spindle-machine system.

In this chapter, a model is established for the spindle machine tool as follows. First, the modal parameters are identified for the spindle head before the spindle is installed on it. Then, two dominant modes from modal analysis are used to configure a simplified model for the spindle head by using springs and the mass of the spindle head. The stiffness of the springs is estimated through the mass and natural frequencies of the spindle head. Springs are also used between the spindle housing and spindle head, whose stiffness is obtained from experience. The frequency response functions at both the spindle nose and the cutter tip are simulated, and verified by performing impact and chatter tests. Finally, the speed effects on the dynamics of the spindle machine tool system are discussed.

5.2 Modal Analysis of the Spindle Head without the Spindle

In order to avoid complex modeling of the whole machine tool, a simplified model is used to simulate the dominant vibration of the machine tool without the spindle system. The spindle head is a casting connecting the spindle to the machine tool; therefore, the spindle head is used to represent the dynamics of the whole machine tool without the spindle on it. The dynamics is different in the X and Y directions because of the asymmetry of the spindle head and machine column. The modal analysis in the X direction is presented here; however,

the same method is applied in the Y direction. Because stiffness in Z direction is much higher than in X and Y directions, and the vibration in Z direction has little influence on the chatter vibration prediction, the vibration in Z direction is not discussed in this thesis.

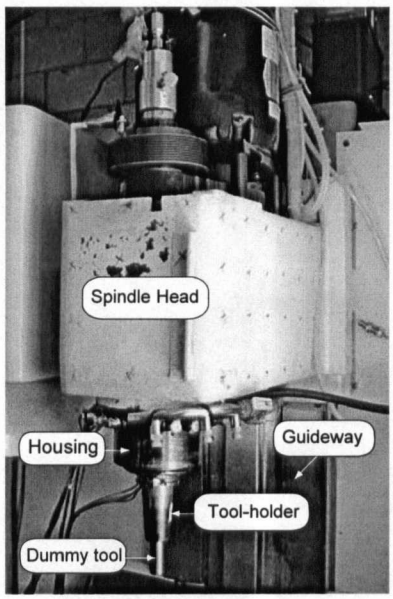

Figure 5-1: The machine tool with a spindle

The modal analysis is performed along the line (1-2-3-4) shown in Figure 5-2, which is parallel to the center-line of the spindle shaft in the X-Z plane, where axis Z stands for the center-line of the spindle shaft. This approach is taken because the final model of the spindle machine tool system is based on the model of the spindle system. The accelerometer is attached to node 1, and the impact force is applied at nodes 1 to 4.

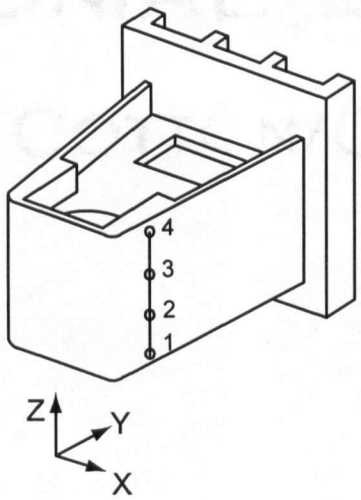

Figure 5-2: The spindle head

The magnitudes of measured FRF for all four nodes are shown in Figure 5-3. The mode shapes are demonstrated in Figure 5-4. The mode at 134 Hz is bending, and the mode at 580 Hz is torsional. These two modes dominate the vibration of the spindle head and have the most effect on the vibration of the spindle system.

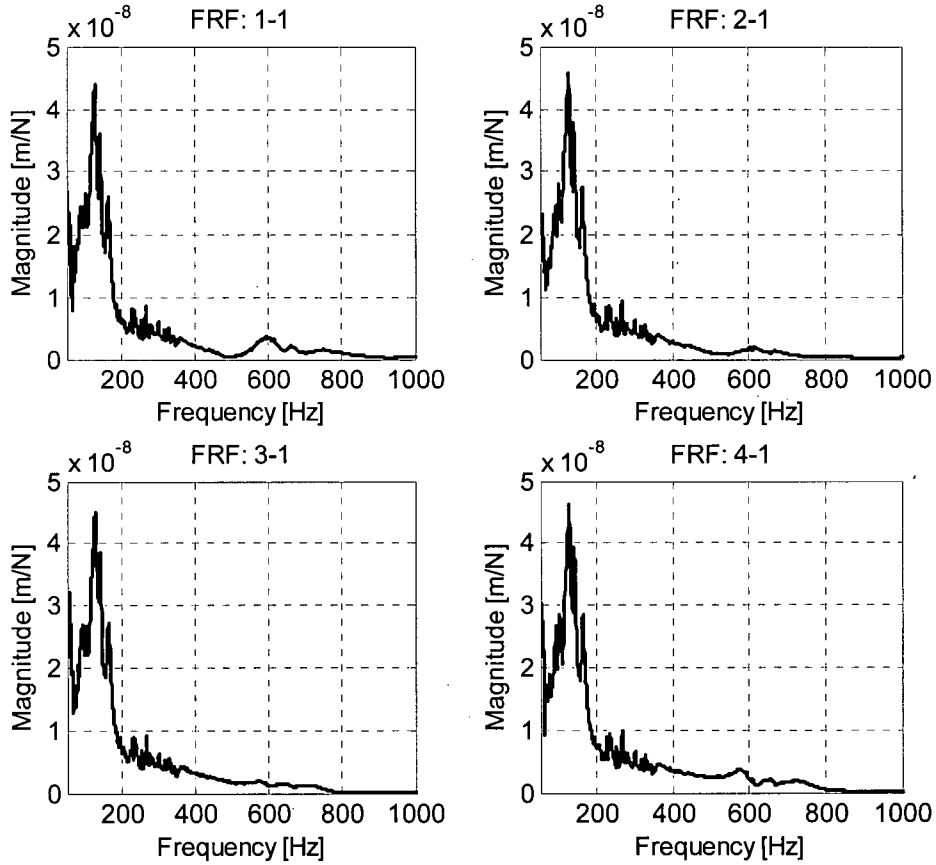

Figure 5-3: FRF in X direction for nodes 1 to 4 on the spindle head without the spindle

Figure 5-4: Mode shapes of the spindle head without the spindle in X direction

5.3 Modeling of the Spindle Head without the Spindle

Because beam theory is used in the finite element formulation, an equivalent cylinder is used to represent the spindle head. Both translational and rotational stiffness of the springs supporting the spindle head is estimated by using two dominant modes from the modal analysis.

As mentioned in section 5.2, the dynamics of the spindle head is different in the X and Y directions. The same equivalent cylinder is used for both directions, but the stiffness of the springs is different. Figure 5-5 shows the model of the spindle head in the X direction. The simulated and measured FRF at node 1 are illustrated in Figure 5-6, which shows that the simplified model can reasonably represent the dynamics of the whole machine tool without the spindle on it.

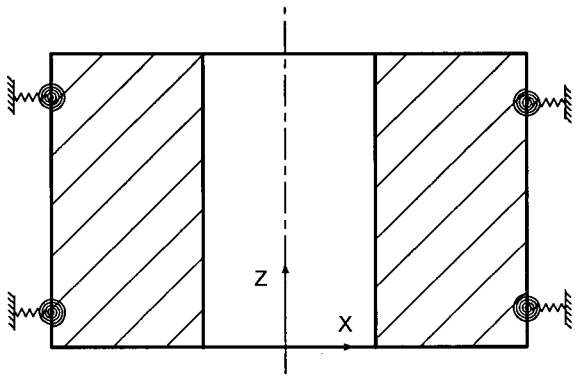

Figure 5-5: The simplified model of the spindle head in the X direction

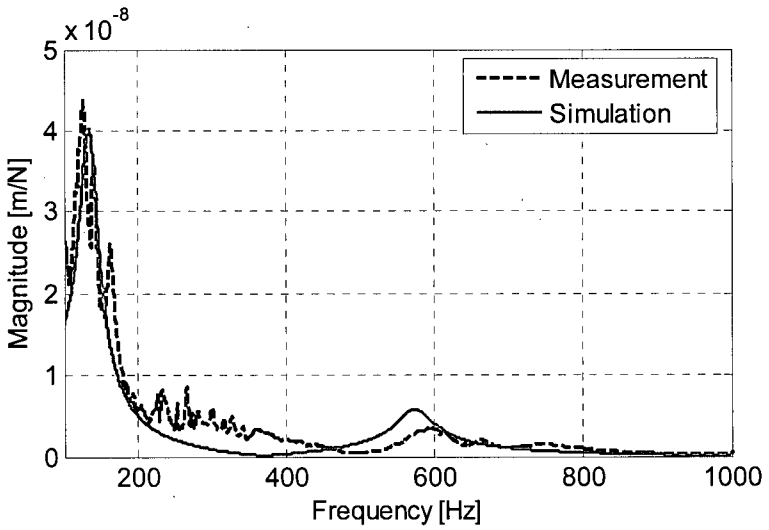

Figure 5-6: The FRF at node 1 on the spindle head without the spindle for X direction

5.4 Modeling of the Spindle Machine Tool System

The spindle is usually fixed on the spindle head through two contact areas, labeled A and B in Figure 5-7. Area A has a large contact surface that can be modeled as relatively rigid connection, i.e., high values are used for both translational stiffness and rotational stiffness of the springs. A fastening ring is used between the rear part of the spindle housing and the spindle head, where the contact area is small, so only a translational spring with small stiffness is used for both X and Y directions. The model for the connection between the spindle housing and the spindle head is shown in Figure 5-8.

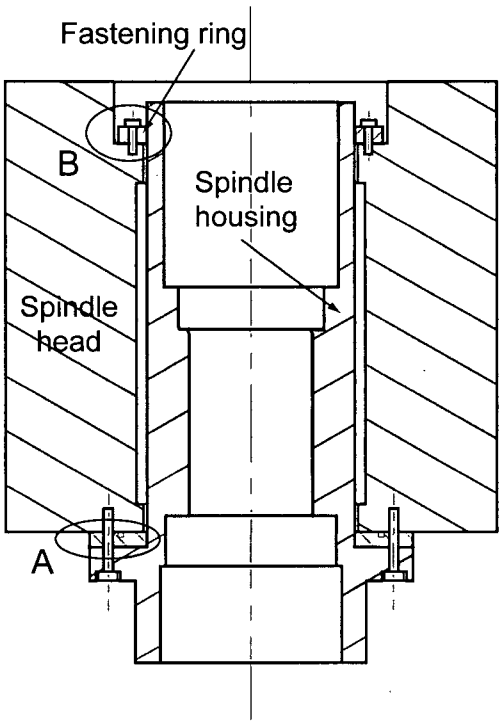

Figure 5-7: Illustration for connection between the spindle head and spindle

The finite element model for the spindle machine tool system not including the tool and tool-holder is displayed in Figure 5-9. Both simulation and impact tests are conducted at the spindle nose. The preload is 300N. The magnitudes of FRF are shown in Figure 5-10, demonstrating that the proposed method can correctly predict the influence of the machine-tool mounting on the dynamics of the spindle system; this should not be neglected. Most researchers, however, do not consider this influence in their work and simply fix the outer rings of the bearings, assuming that the machine tool is rigid, which is not true for most

industrial machine tools. Figure 5-11 demonstrates the influence of the machine tool on spindle dynamics. If the dynamics of the machine tool is not included in the model, in this example, the housing is fixed, which is equivalent to the fixing of the outer rings of bearings because the housing is very rigid, the lower frequencies of the spindle machine tool system cannot be captured, and the high frequencies shift higher.

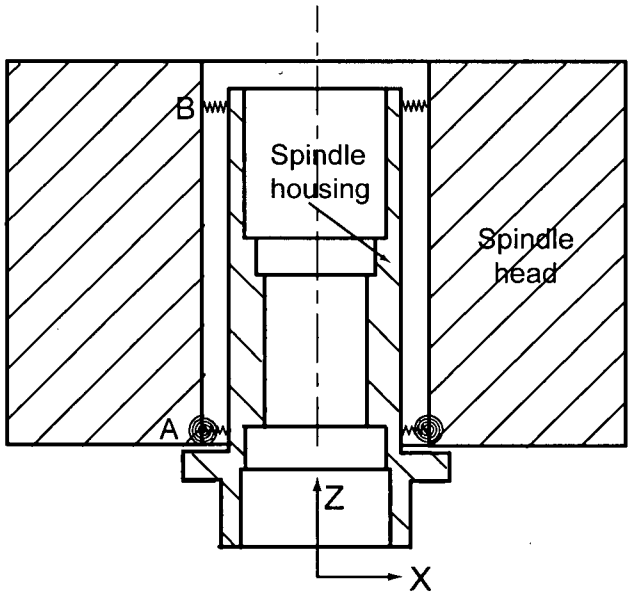

Figure 5-8: Model for connection between the spindle head and spindle

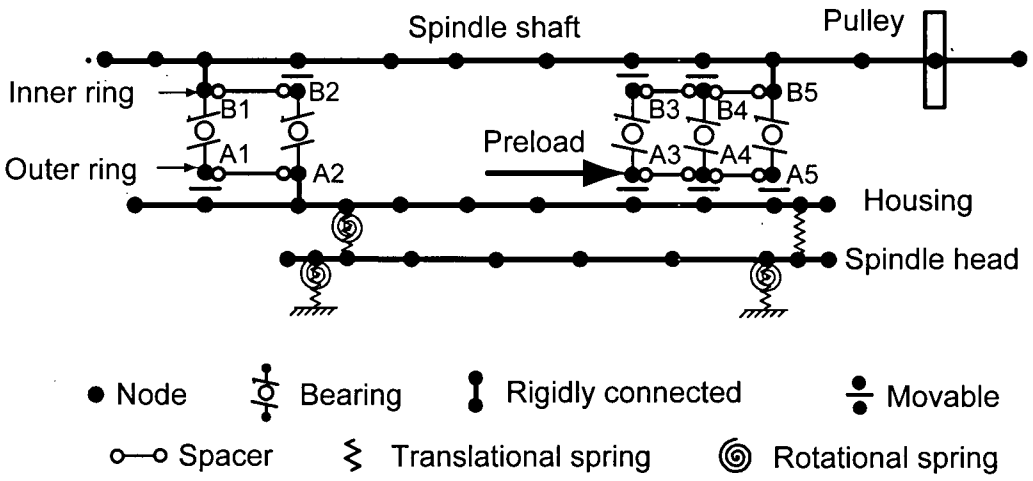

Figure 5-9: The finite element model for the spindle machine tool system

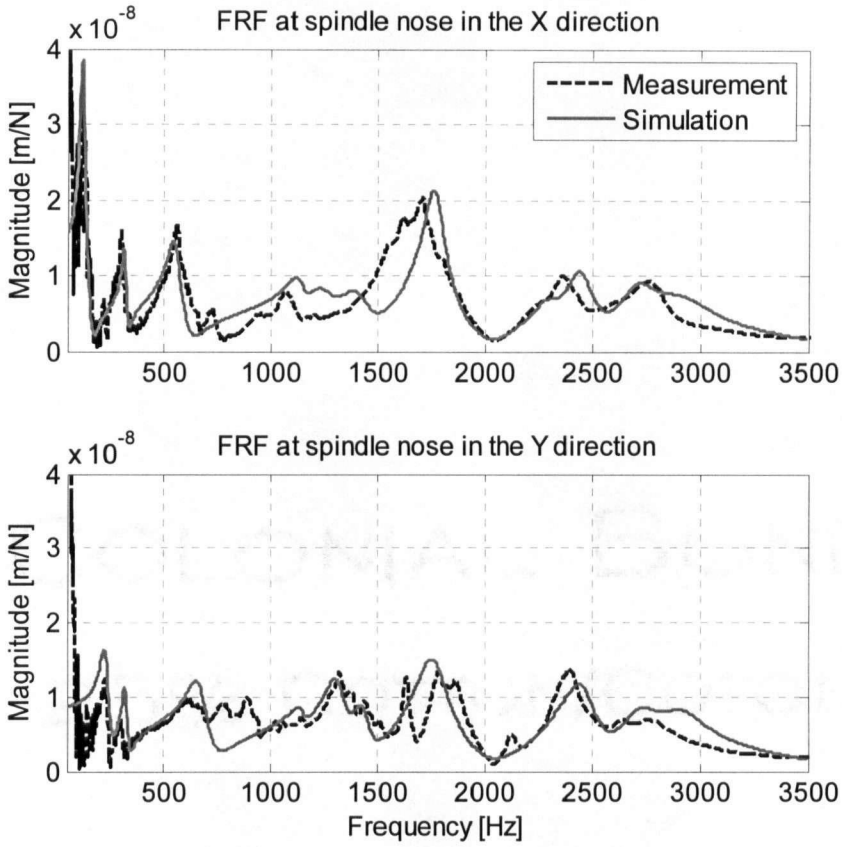

Figure 5-10: FRF at spindle nose in the X and Y directions for the spindle machine tool system

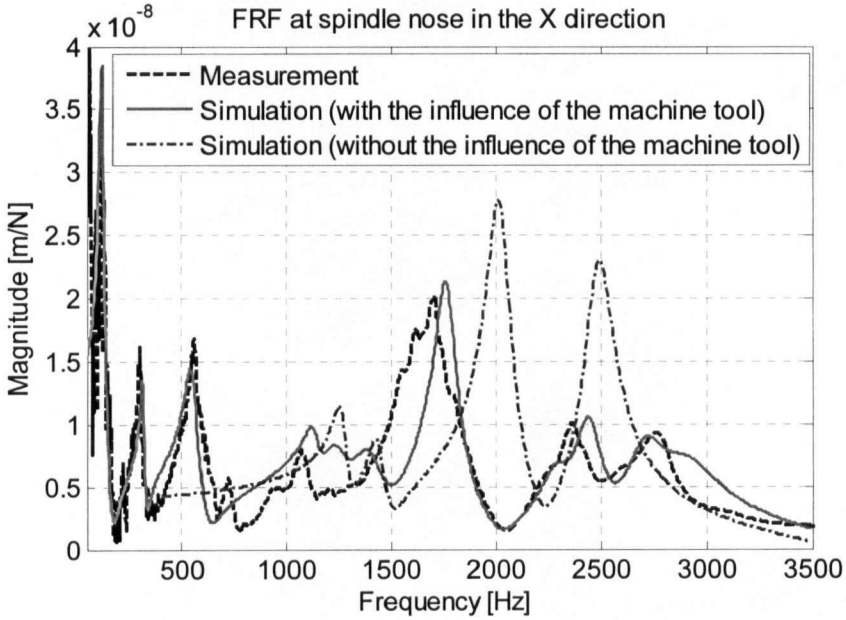

Figure 5-11: Comparison of the influence of the machine tool on spindle dynamics

5.5 Prediction of Chatter Vibration Using the Model of the Spindle Machine Tool System

5.5.1 FRF Prediction at the Tool Tip

In order to predict stability lobes in the frequency domain, the FRF at the tool tip in both the X and Y directions needs to be ascertained. Thus, the end mill and tool-holder must be modeled. In both the simulation and the experiment, the shrink-fit tool-holder CAT40 (i.e., CV40TT20M400) and an end mill with a diameter of 20 mm and a stick-out of 50 mm are used, and are assumed to connect rigidly. The tool-holder-spindle connection is claimed to be the main source of flexibility in practice. This connection is also difficult to model due to unknown contact stiffness and damping at the tool-holder joints [67]. Two scenarios are tested in this thesis: the tool-holder is rigidly connected, or it is connected via distributed springs [68] at the spindle taper. The finite element model of the entire spindle machine tool system is shown in Figure 5-12, where the tool-holder is rigidly linked to the spindle taper.

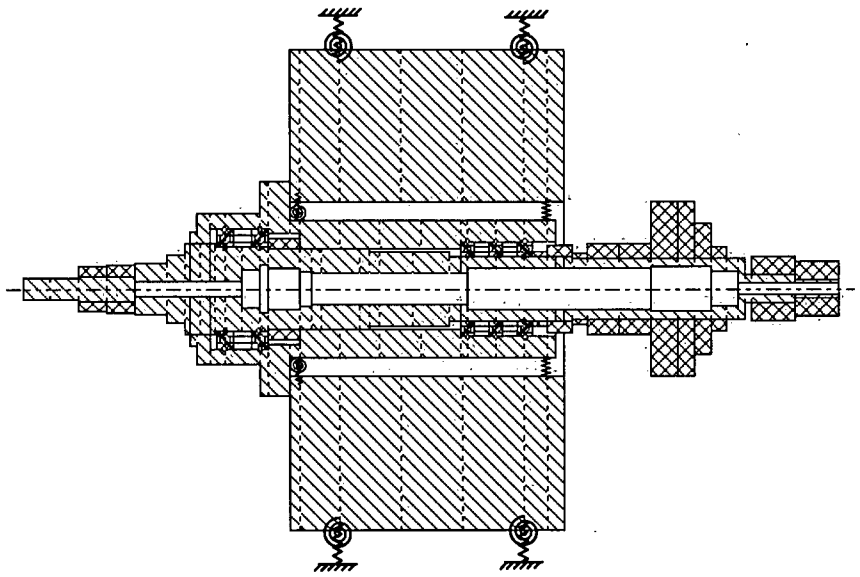

Figure 5-12: FE model presented in SpindlePro® for the spindle machine tool system

The magnitudes of FRF at the tool tip in both the X and Y directions for the rigid tool-holder-spindle connection are shown in Figure 5-13, where the bearing preload is 1200N. The simulation matches measurements very well at lower frequencies, but the errors increase at higher frequencies.

The comparison of FRF for the two interface connections is shown in Figure 5-14. The first three modes less than 500 Hz match each other. At the dominant mode of 1000Hz, both methods yield slightly smaller frequency values than the measurement, with the spring connection being worse than the rigid one. However, the added springs lead to little better results at higher frequencies; in this example, they are above 3500 Hz. The results also indicate that the rigid connection is acceptable for a shrink-fit tool-holder, which is used for the remaining analysis in this thesis.

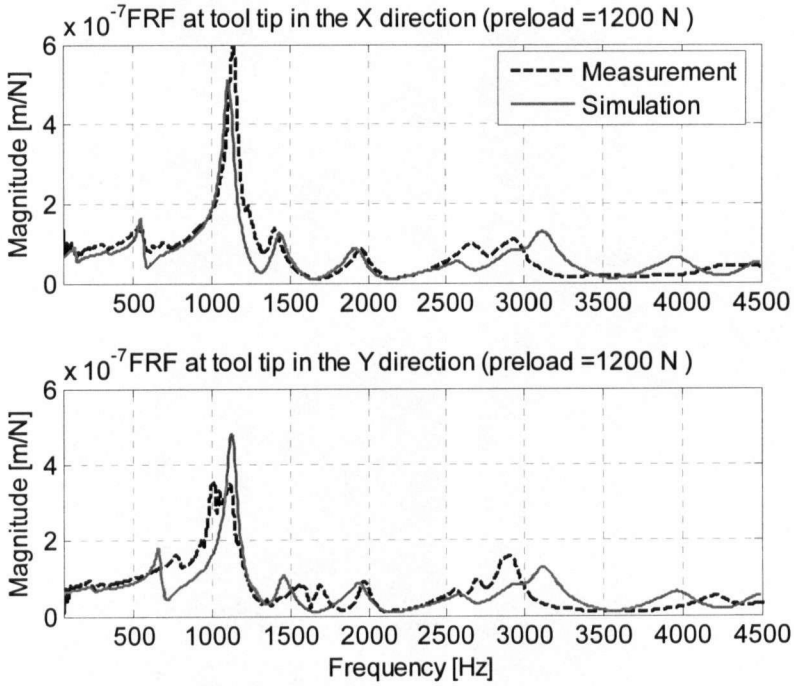

Figure 5-13: FRF at the tool tip for rigid connection of the tool-holder

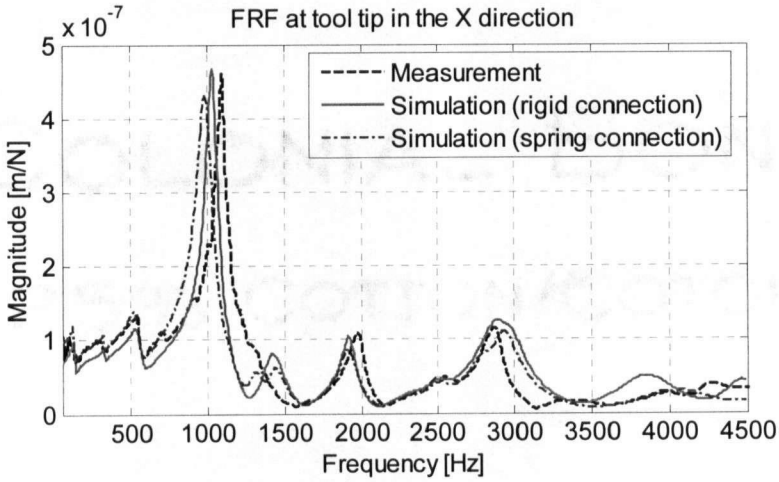

Figure 5-14: Comparison between rigid and elastic connections

5.5.2 Prediction of Stability Lobes and Chatter Test

In this test, the same shrink-fit tool-holder and four-flute end mill as described in section 5.5.1 are used. The work-piece material is Aluminium 7050. The Budak-Altintas chatter stability theory [60][61] is used to predict the stability lobes by using both simulated and measured FRF at the tool tip. The results are shown in Figure 5-15 and verified by cutting tests conducted under the six cutting conditions marked with boxes or circles in Figure 5-15.

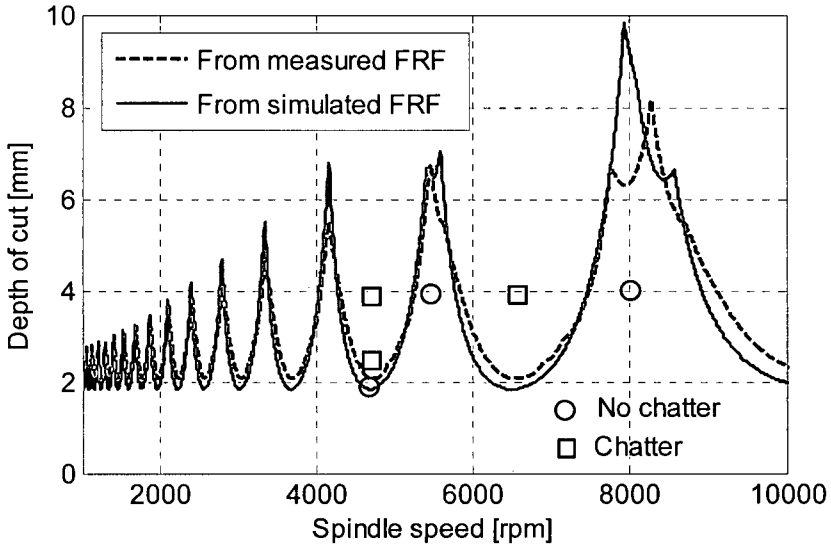

Figure 5-15: Predicted stability lobes from measured and simulated FRF

In summary, the simulated FRF can correctly predict the stability lobes, which further establishes the validity of the model for the spindle machine tool system.

5.6 Time History Response under Cutting Forces in Milling Operations

In this section, the time history of displacement responses, bearing stiffness, and bearing contact forces are simulated. The same tool-holder, tool, and work-piece are used in the test as were used in the previous tests. A spindle speed of 6000rpm is chosen because of the dynamics of the dynamometer and fixture for the displacement sensor, which is explained later. Feed rate is 0.1mm per flute. Two scenarios are considered, one without chatter vibrations in which the depth of cut is 2mm, and another with chatter where the depth of cut is 4mm. The cutting forces in X, Y and Z directions are measured by a dynamometer (Kistler 9255B) during cutting tests, and are applied on the tool tip in the simulation. The

measurement setups are shown in Figure 5-16 and Figure 5-17. Displacement in both the X and Y directions at node 2 of the tool-holder, which is 52mm away from the tip of the tool-holder, are measured.

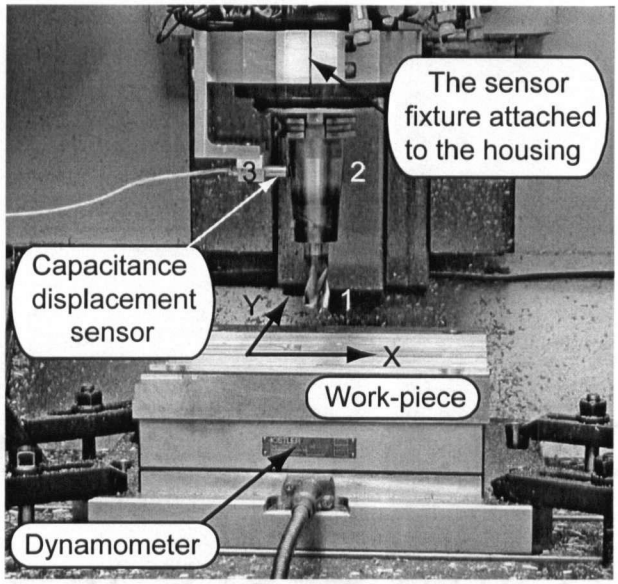

Figure 5-16: Setup for the measurement of forces and displacement (a)

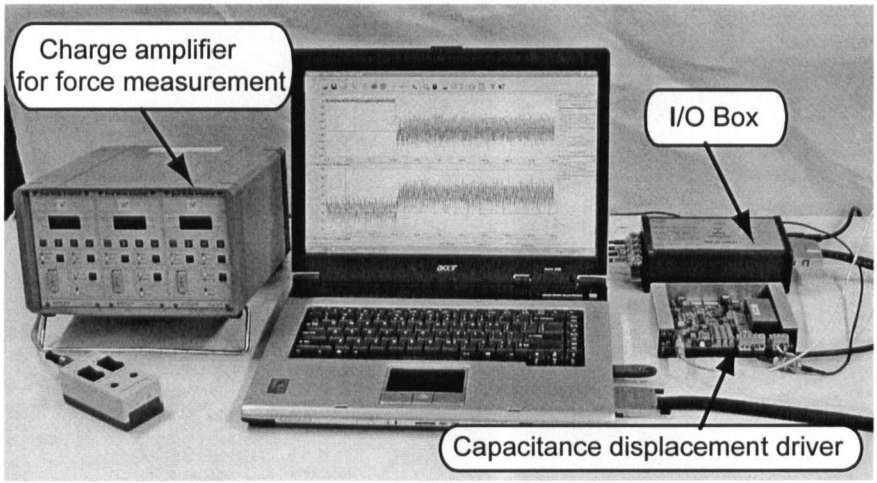

Figure 5-17: Setup for the measurement of forces and displacement (b)

5.6.1 Measurement of Cutting Forces

In order to measure the cutting forces correctly, the FRF of the dynamometer has to be determined to make sure that the frequencies of the cutting forces are within the bandwidth of the dynamometer. The measured force-to-force FRF in both the X and Y directions are

shown in Figure 5-18, which indicates that the measured forces are correct only under certain ranges of frequency. For instance, at 400 Hz, the corresponding spindle speed is 6000 rpm for 4-fluted cutters. At the harmonics of 800 Hz and 1200 Hz, the magnitudes of the FRF in the Y direction are about 1.5 and 1.3, which will amplify the cutting forces by 50% and 30%, respectively.

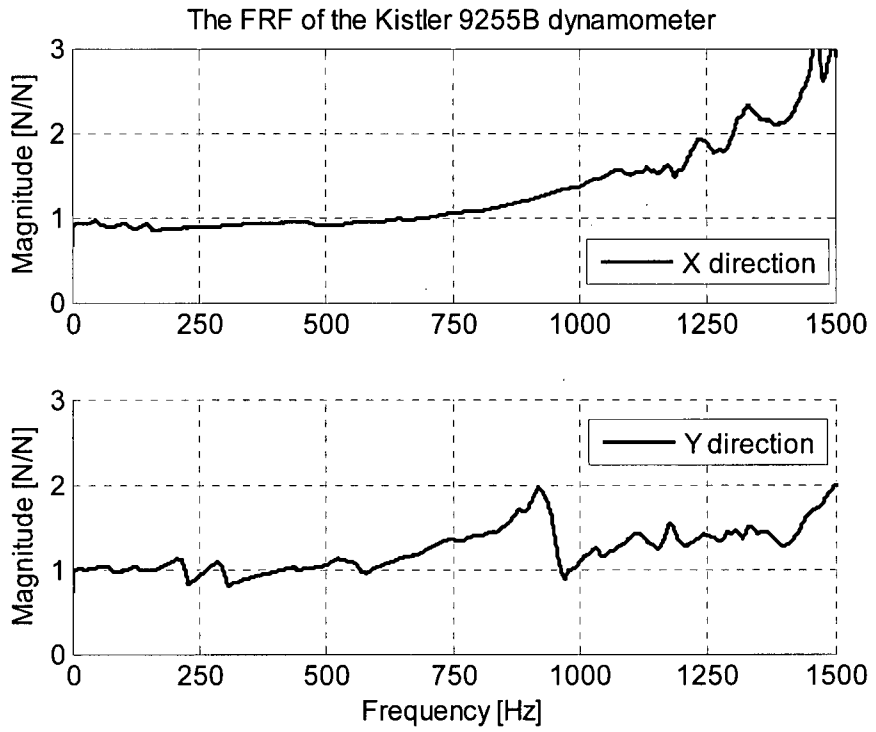

Figure 5-18: The FRF of the Kistler 9255B dynamometer

The measured cutting forces, the spectra of the forces, and the machined surfaces for both depths of cut are shown in Figure 5-19 and Figure 5-20. The depth of cut is increased by 100%, in Figure 5-20, but the cutting forces increase more than 500% due to chatter vibrations. From the spectrum of the cutting forces, the dominant frequency of the cutting forces at the depth of cut of 2mm is 400 Hz, while it is 1028 Hz at 4mm, which is the chatter frequency. The magnitude of the FRF for the dynamometer in the X direction is 30% higher than 1, and 20% higher than 1 in the Y direction. Therefore, the measured forces at the chatter frequency are still acceptable, and will be used as the input forces at the tool tip in the simulation, but reduced by 30% and 20 % in the X and Y directions, respectively.

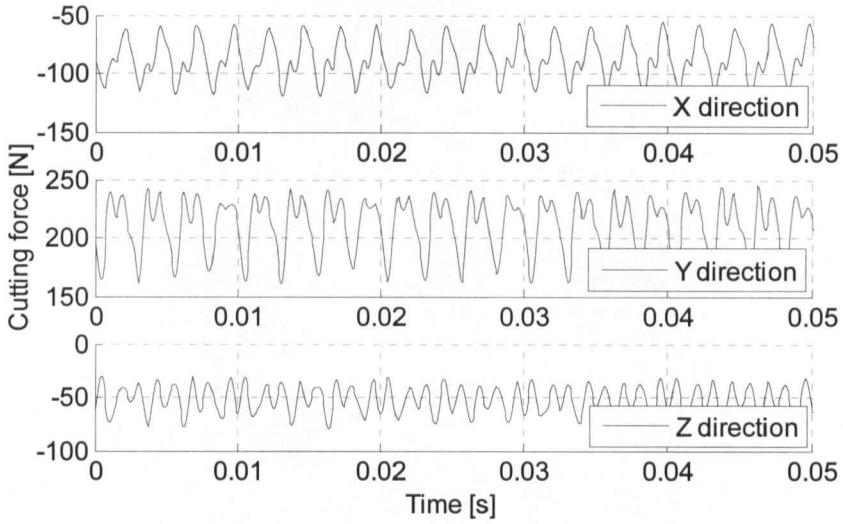

(a) The measured cutting forces in the X, Y and Z directions

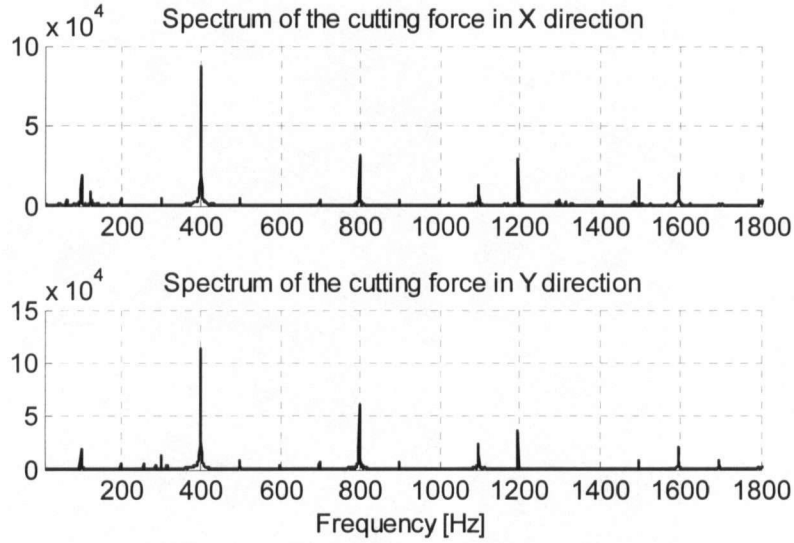

(b) The spectra of the cutting forces

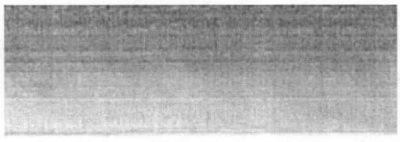

(c) Machined surface (smooth surface because of stable cutting)

Figure 5-19: The measured cutting forces, force spectrum, and machined surface (spindle speed: 6000 rpm, depth of cut: 2mm, feed rate: 0.1mm/flute, no chatter)

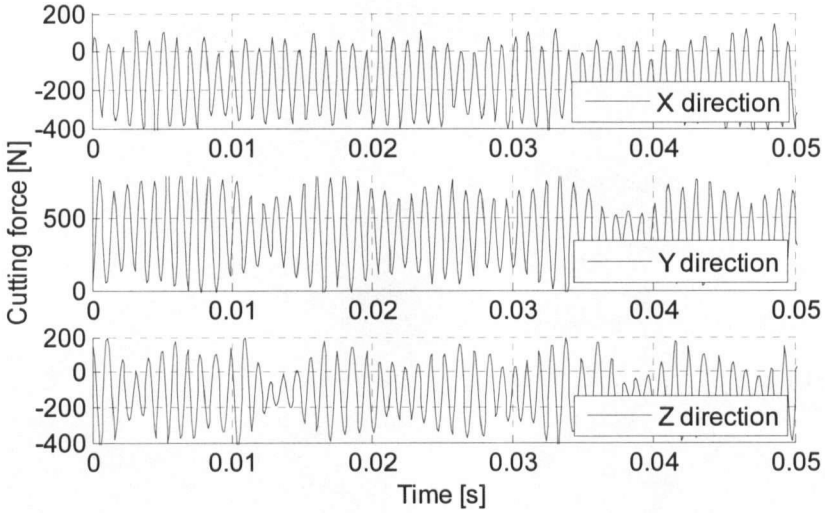

(a) The measured cutting forces in the X, Y and Z directions

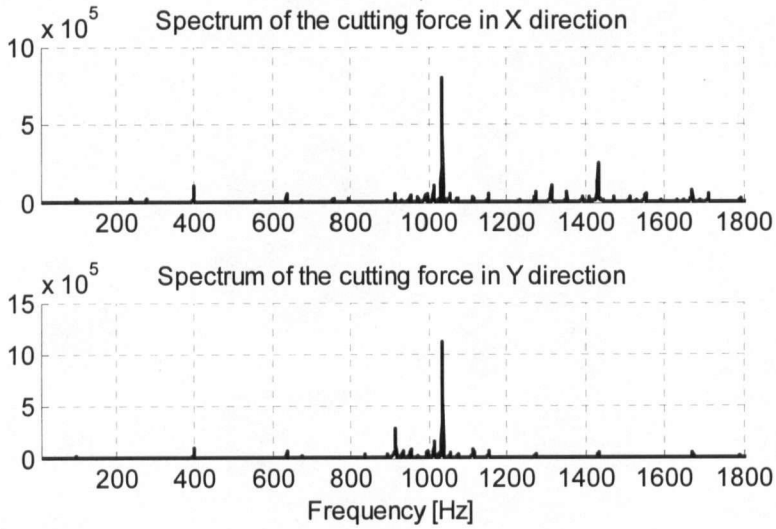

(b) The spectra of the cutting forces

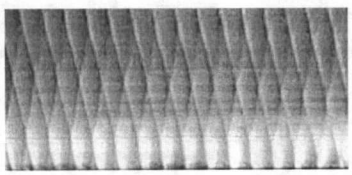

(c) Machined surface (rough surface because of chatter vibration)

Figure 5-20: The measured cutting forces, force spectrum, and machined surface (spindle speed: 6000 rpm, depth of cut: 4 mm, feed rate: 0.1mm/flute, chatter)

5.6.2 Displacement Response

Similar to the force measurement, the fixture for the displacement sensor has to be designed correctly to avoid the frequencies at which the displacements are measured. The FRF between node 1 on the tool tip and node 2 on the tool-holder are measured with a capacitance-displacement sensor, as well as an accelerometer attached to node 2 on the tool-holder. The measured FRFs are shown in Figure 5-21. Overall, the FRF measured by the accelerometer is in good agreement with that measured by the displacement sensor. However, one big mode at 550Hz is introduced by the fixture of the displacement sensor. In addition, the displacement sensor is affected by an AC power frequency of 60Hz. Figure 5-21 indicates that the matches of FRF magnitudes at frequencies of 100Hz, 200Hz, 400Hz, 800Hz, and 1028Hz are acceptable; these frequencies are involved in the cutting tests.

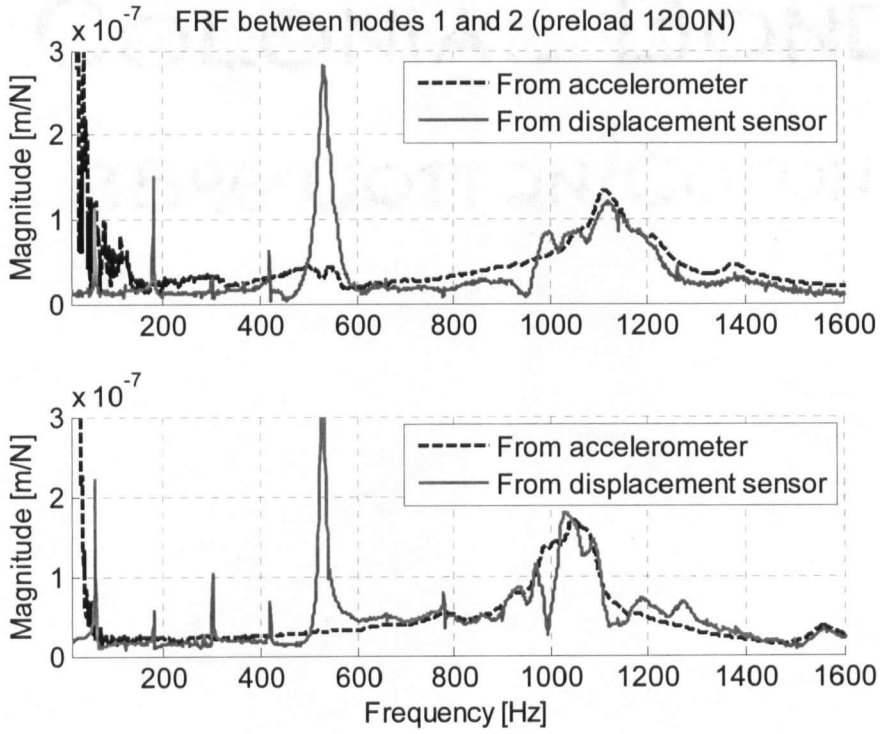

Figure 5-21: FRF between nodes 1 and 2 measured by two types of sensor

The measured and simulated displacements at node 2 on the tool-holder for both depths of cut are shown in Figure 5-22 and Figure 5-23. The maximum simulated displacements are very close to the maximum measured displacements although the distribution is a little different. As mentioned in section 5.6.1, the measured forces in the Y direction are bigger

than the real forces. Therefore, the simulated displacements are also bigger than the measured ones.

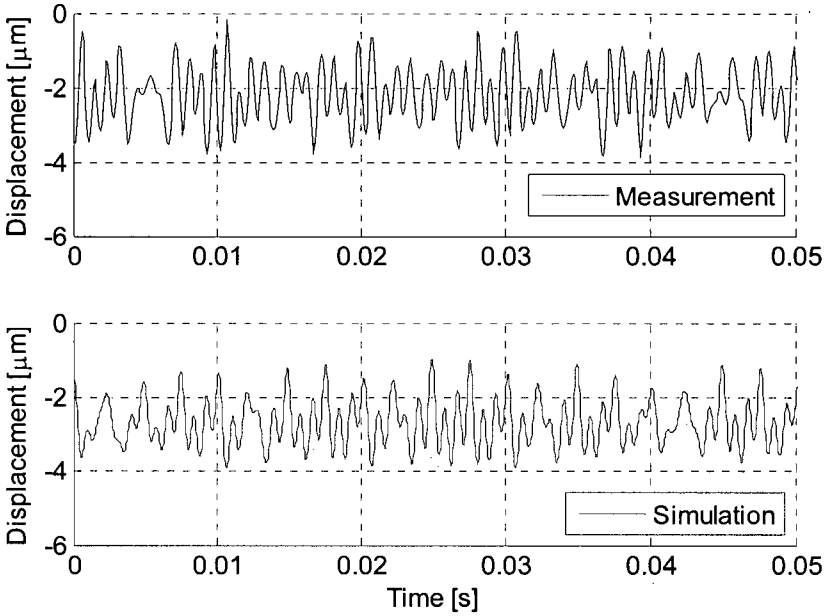

(a) Displacement at node 2 on the tool-holder in the X direction

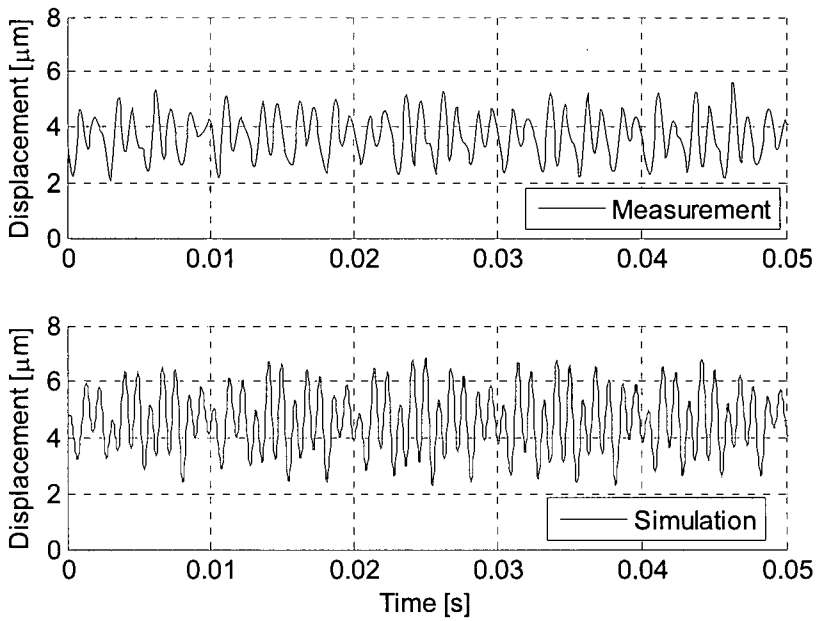

(b) Displacement at node 2 on the tool-holder in the Y direction

Figure 5-22: The measured and simulated displacements at node 2 on the tool-holder (spindle speed: 6000rpm, depth of cut: 2mm, feed rate: 0.1mm/flute, no chatter)

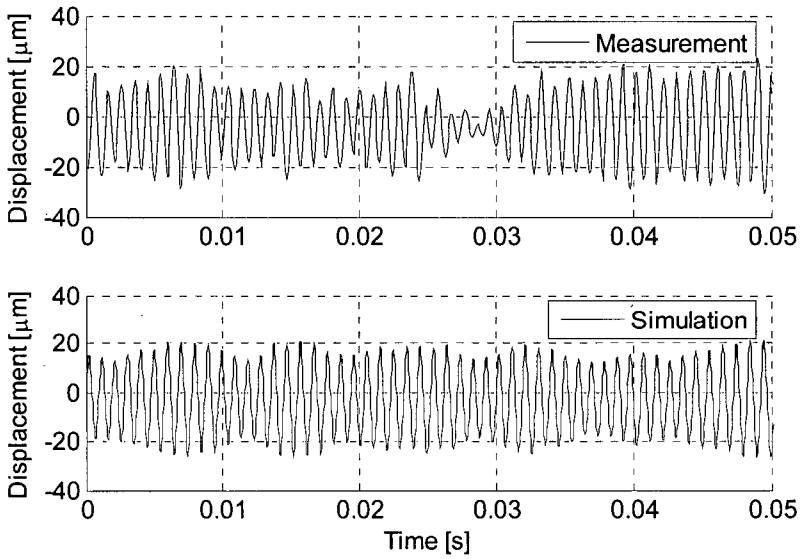

(a) Displacement at node 2 on the tool-holder in the X direction

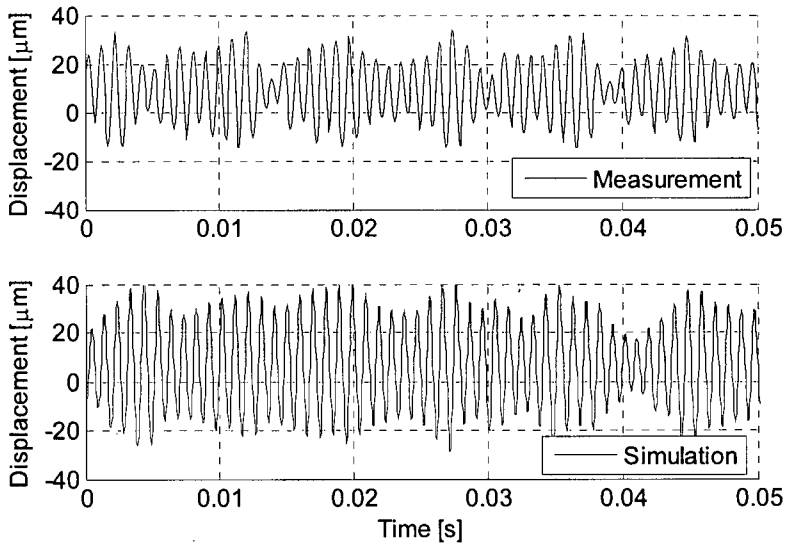

(b) Displacement at node 2 on the tool-holder in the Y direction

Figure 5-23: The measured and simulated displacements at node 2 on the tool-holder (spindle speed: 6000rpm, depth of cut: 4mm, feed rate: 0.1mm/flute, chatter)

5.6.3 Bearing Stiffness

The simulated radial stiffness of bearings No.1 and No.5 for the two cutting tests is illustrated in Figure 5-24. The stiffness of the first bearing is affected more than that of the fifth bearing by the cutting forces. With chatter, the bearing stiffness can even reach zero. All

forces are treated as dynamic forces in the simulation. The preload is applied to the bearings first, and the cutting forces are applied to the tool tip after the vibration due to the preload diminishes.

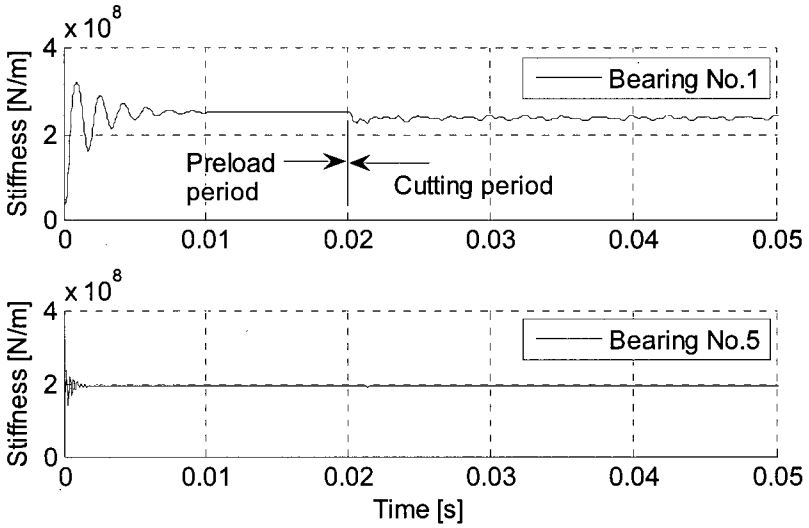

(a) Radial bearing stiffness under cutting forces (DOC=2mm, no chatter)

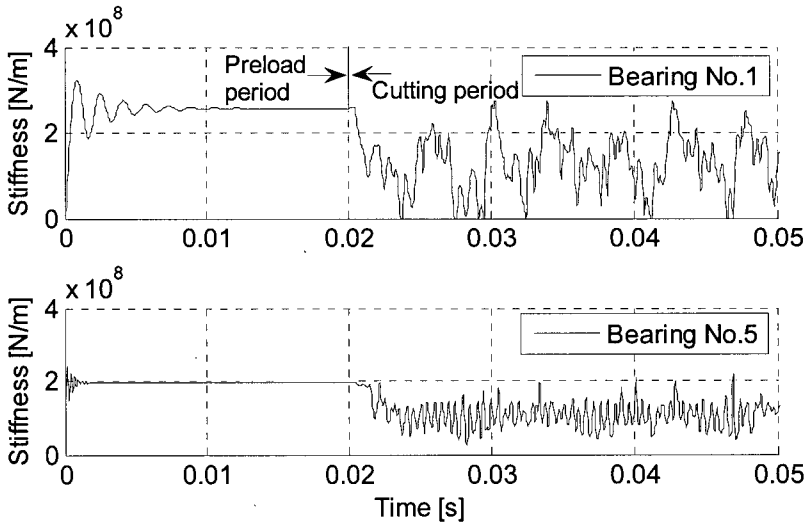

(b) Radial bearing stiffness under cutting forces (DOC=4mm, chatter)

Figure 5-24: Radial bearing stiffness under cutting forces (spindle speed: 6000rpm, feed rate: 0.1mm/flute)

5.6.4 Bearing Contact Forces

The contact forces experienced by bearings No.1 and No.5 for both cases are shown in Figure 5-25. Similar to the case of bearing stiffness, the first bearing bears higher forces than

does the fifth bearing. As mentioned before, bearing stiffness and contact forces cannot be measured directly. The correct prediction of the FRF and displacement response, however, indirectly proves the validity of their simulation, because bearing stiffness is closely related to the contact forces.

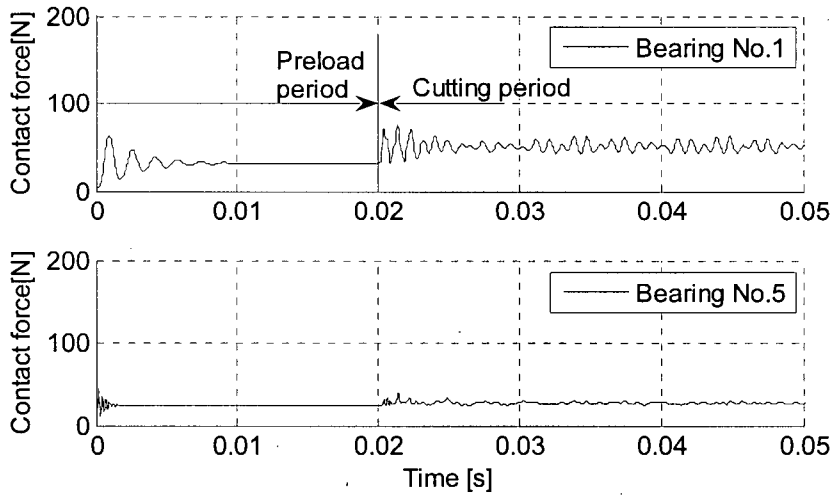

(a) Simulated bearing contact forces under cutting (DOC=2mm, no chatter)

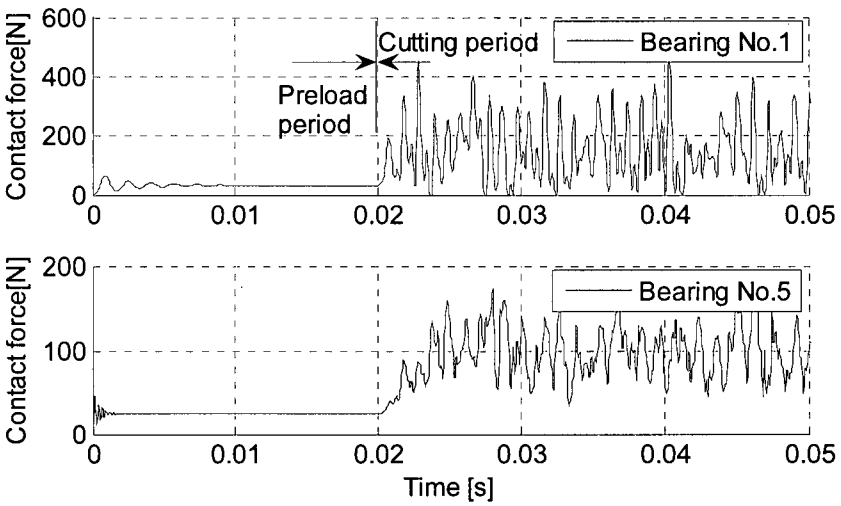

(b) Simulated bearing contact forces under cutting (DOC=4mm, chatter)

Figure 5-25: Simulated bearing contact forces under cutting (spindle speed: 6000rpm, feed rate: 0.1mm/flute)

5.7 Effects of Preload and Speed on the Dynamics of Spindle Machine Tool Systems

The setup for FRF measurement when the spindle is running is shown in Figure 5-26. The impact force is applied at the tip of the dummy tool. FRF is simulated and measured under different preloads and spindle speeds. Due to the limitation of the machine tool and the spindle, the measurement is conducted up to a spindle speed of 10,000 rpm.

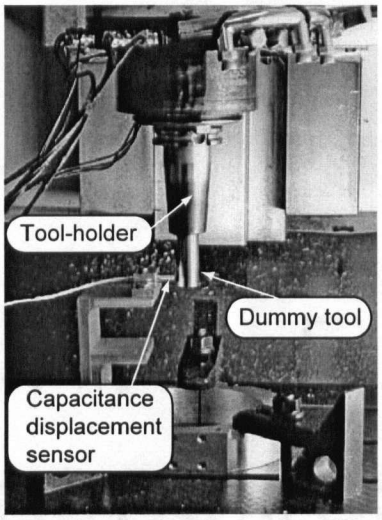

Figure 5-26: Setup for the measurement of FRF

Figure 5-27 shows the relation among radial bearing stiffness, preload, and spindle speeds for bearing No. 1. The bearing stiffness increases with increased preload, but decreases as the spindle speed increases. The speed effects are more obvious at lower preloads than at higher preloads.

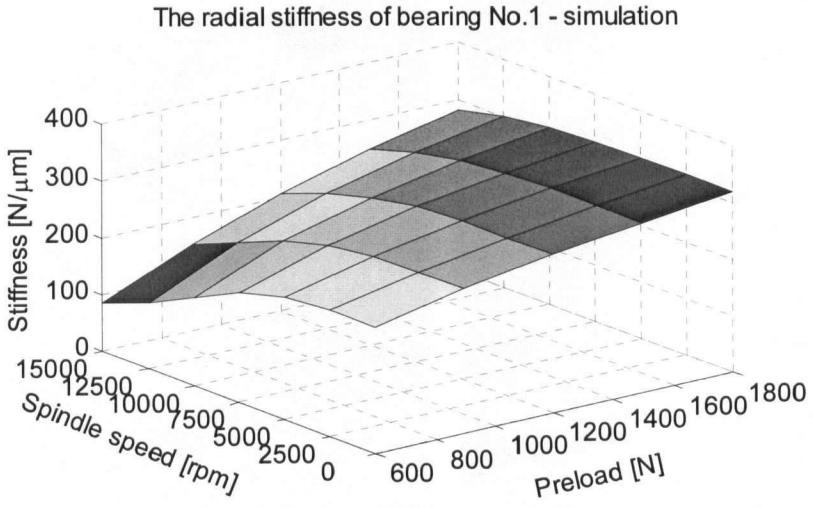

Figure 5-27: The influence of the preload and spindle speed on bearing stiffness.

In general, the natural frequencies of all modes increase with preload due to increased bearing stiffness, but decrease with spindle speed due to centrifugal forces. The first dominant natural frequency, which is about 540Hz, changes little with preload and spindle speed. A sample relationship between the speed, preload and the second dominant natural frequency is illustrated in Figure 5-28. Similar to bearing stiffness, the natural frequencies increase with increased preload, but decrease as spindle speed increases. The speed effects are more crucial at lower preloads.

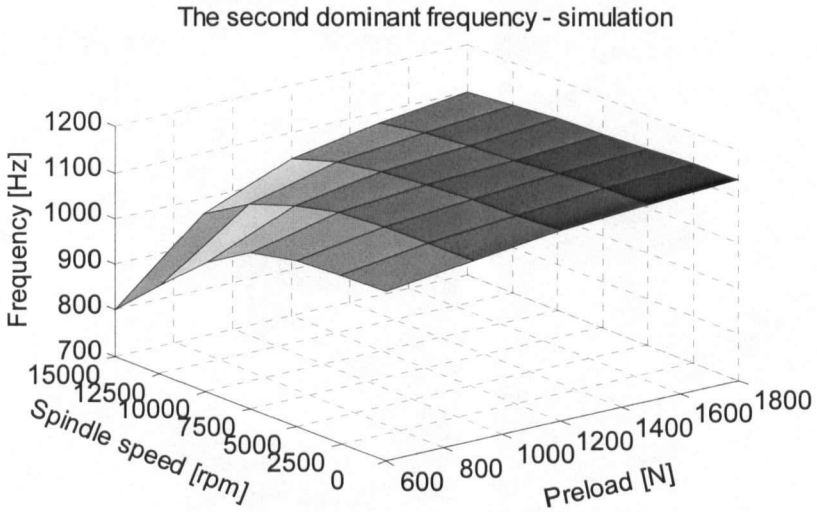

Figure 5-28: The influence of preload and speed on the second natural frequency

A comparison of the simulated and measured natural frequency of the second dominant mode under different preloads and spindle speeds is shown in Figure 5-29. Overall, the match between simulation and measurement is good.

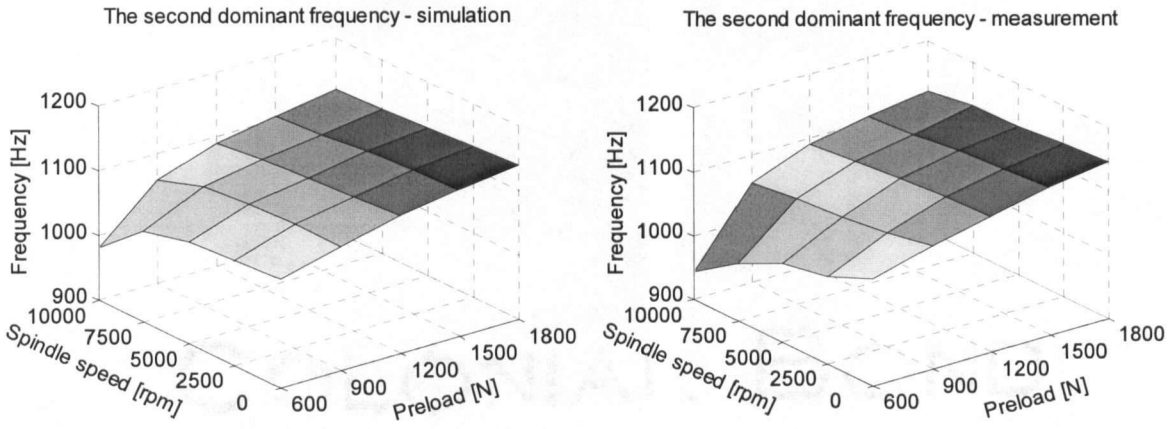

Figure 5-29: Comparison of the simulated and measured second natural frequency under different preloads and spindle speeds

In order to compare the simulation and measurement more clearly, the influence of the preload and spindle speed on the second dominant natural frequency is plotted separately in Figure 5-30 and Figure 5-31, by fixing either the spindle speed or preload. The frequency increases from 1068 Hz to 1142 Hz when preload is increased from 600 N to 1800 N. However, the frequency drops from 1140 Hz to 1090 Hz when the speed is increased from stationary to 10000 rpm. It is shown that the proposed model can correctly predict the effects of the preload and spindle speed on the dynamics of spindle machine tool systems.

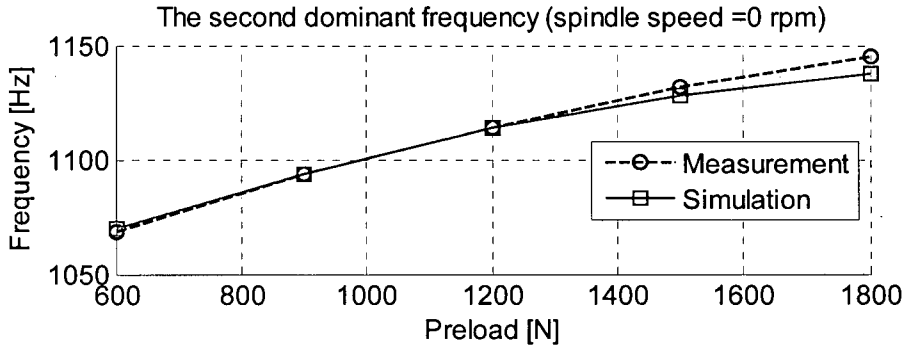

Figure 5-30: The influence of the preload on the second natural frequency

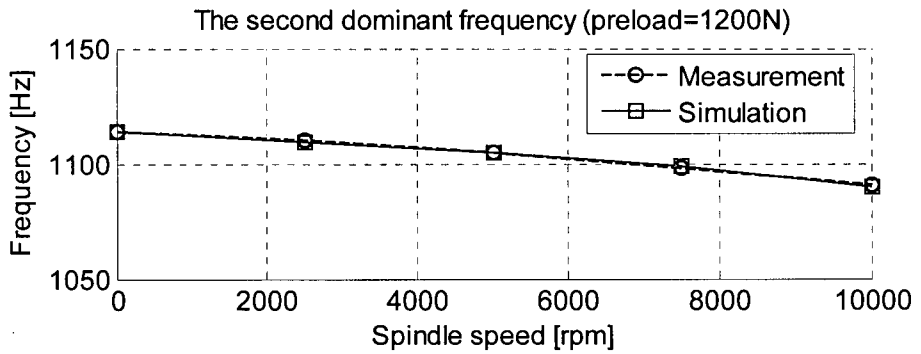

Figure 5-31: The influence of spindle speed on the second natural frequency

5.8 Effects of Preload on the Stability Lobes for Milling Operations

The preload changes the bearing stiffness, which leads to variation in the FRF and stability lobes. Figure 5-32 demonstrates the influence of preload on the stability lobes in which the measured FRF are used, and does not include speed effects. The results show that the critical depth of cut decreases with increased preload. This is because modal damping decreases with increased preload. The stability lobes shift to the right as the preload increases.

In conclusion, the preload cannot improve the critical depth of cut in stability lobes, but it can reduce the forced vibration at lower frequencies, since it increases static stiffness due to increased the bearing stiffness.

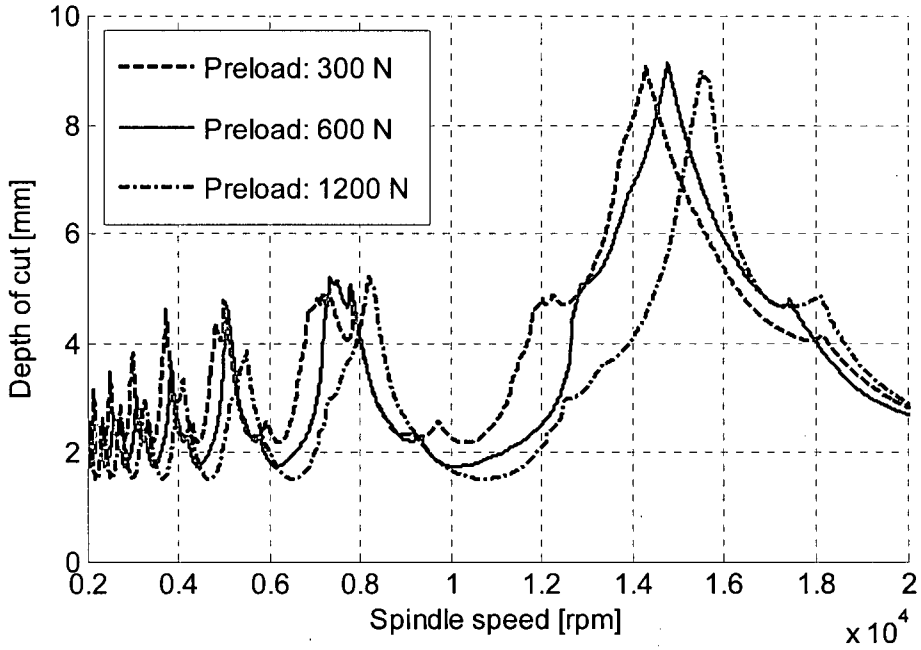

Figure 5-32: The influence of the preload on stability lobes

5.9 Effect of Spindle Speed on Stability Lobes for Milling Operations

Due to the dependency of the stability lobes on spindle speed, it is time consuming to predict them by including speed effects. At each spindle speed, the machine has a FRF at the tool tip. By using the chatter-prediction theory in the linear, frequency domain, only one depth of cut can be obtained at this speed in each calculation due to nonlinearity.

In this simulation, a preload of 1200N is used, and the spindle speed is varied from 5000 to 18000 rpm at discrete intervals. The influence of spindle speed on the stability lobes is shown in Figure 5-33. The simulated results demonstrate that spindle speed has a negligible effect on stability lobes at lower spindle speeds, and that the lobes shift to the left at higher spindle speeds. The critical depth of cut does not change much.

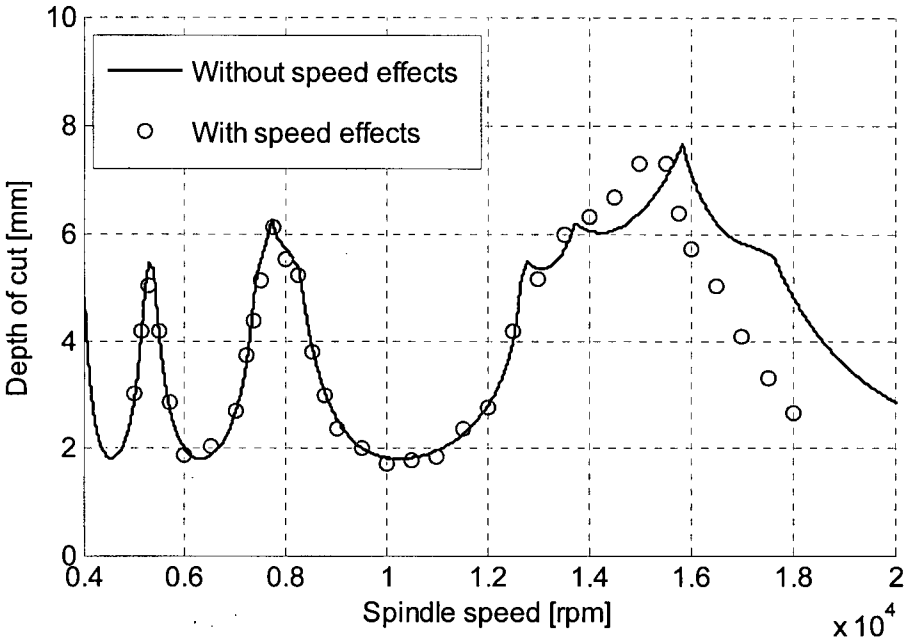

Figure 5-33: The influence of spindle speed on stability lobes

5.10 Summary

A general method is presented in this chapter for modeling the spindle machine tool system, which consists of the cutter, tool-holder, spindle shaft, bearings, housing, and the machine tool. A simplified model representing the dynamics of the whole machine tool without the spindle on it is developed by means of experimental modal analysis; this work needs to be done only once for every machine tool. The model of the whole machine-tool system is then created by coupling the spindle with the simplified model of the machine tool without the spindle. The assembly of the spindle unit and spindle head is modeled through contact springs. The proposed method is validated by performing impact hammer tests and cutting tests.

Both simulation and experiment show that the machine tool has a significant effect on spindle dynamics. In other words, the machine tool dynamics must be considered in order to simulate cutting operations. Unfortunately, this effect has hardly been studied in the past. Most papers still use a very simple model, and show excellent results from both simulation and experiment. The key issue is that they compare only natural frequencies, not frequency

response functions, which are the most important way to study the dynamics of the structures and verify the model for metal cutting. It is not hard to match one or more frequencies, even if the model is not completely accurate, because there are so many modes in the spindle system. It is impossible, however, to match the FRF if the model is not accurate, because FRF includes not only natural frequencies but also information about the mode shapes, modal damping, and dynamic stiffness.

The preload can increase bearing stiffness, leading to increased natural frequencies, which shifts the stability lobes to the right. However, higher preload usually reduces the damping, which decreases the critical depth of cut. The preload cannot efficiently improve the stability lobes, but it can enhance the static stiffness and reduce the forced vibrations. The most efficient method of increasing the critical depth of cut is to raise the damping.

Increased spindle speed causes decreased bearing stiffness, which lowers the natural frequencies. The stability lobes shift to the left due to the decreased natural frequencies. These speed effects are very obvious at higher spindle speeds and lower preloads.

The above speed effects on the dynamics of the spindle system are verified experimentally under a spindle speed of 10,000 rpm. Due to the speed limitation of the machine tool and the spindle, the effects of spindle speeds over 10,000 rpm are not verified in this thesis, are listed as a future research direction.

Chapter 6
Optimal Design of Spindles

6.1 Overview

With the rapid development of computer technology and numerical simulation techniques, finite element analysis (FEA) is widely accepted in machine design. Consider the spindle design as an example. Once the configuration of the spindle has been decided upon, the designer starts to analyze the spindle, trying to obtain a better design. "Trial and error" analysis methods are typically used until a satisfactory design is achieved. However, the designers can never know whether the design is the best suited for the targeted applications or not.

In order to apply an optimization technique to spindle design, objectives and design variables must be first identified. Many performance parameters can be selected as objectives, such as minimum weight, highest basic frequency, maximum dynamic stiffness, depth of cut, and so on. Among all of these objectives, maximum dynamic stiffness and depth of cut are directly related to chatter vibration, which is the most important issue in the machining industry since it can cause spindle failure, resulting in expensive repairs. The main objective of this thesis is to design a high dynamic stiffness or chatter-free spindle.

There are a significant number of parameters in a typical spindle design process, such as the dimensions of the spindle shaft and housing, and bearing locations. Due to the high nonlinearity of both objectives and constraints which are expressed in implicit forms, convergence is always a big issue in the optimization process. Therefore, the most effective design parameters need to be selected to reduce the number of design variables in practice. There are numerous constraints on the geometric design of spindle parts, and design dimensions are usually coupled with each other. For instance, if the diameter of the spindle shaft changes, the bore diameter of the housing also has to be modified, and consequently more parameters need to be taken into account, which might not be practical. In practice, the most independent dimensions affecting spindle dynamics the most are bearing positions and preload.

Preload is a very important factor in the design of a spindle. A reasonable preload must be provided for bearing. Higher preload can produce higher bearing stiffness, but it cannot guarantee higher dynamic stiffness of the spindle system, because damping may decrease with the preload. In this thesis, the objectives are maximum dynamic stiffness or depth of cut for chatter-free spindles. Bearing locations and bearing stiffness controlled mainly by preload are used as design variables.

6.2 Dynamic Stiffness of the Spindle

The dynamic stiffness of the spindle is defined from the frequency response function at the tool tip or spindle nose, which is described as follows.

By using the finite element method, the following linear equations for forced vibration can be obtained for the spindle system:

$$\mathbf{M}\ddot{\mathbf{x}} + \mathbf{C}\dot{\mathbf{x}} + \mathbf{K}\mathbf{x} = \mathbf{F} \tag{6.1}$$

In modal coordinates, it is expressed as

$$\overline{\mathbf{M}}\ddot{\mathbf{y}} + \overline{\mathbf{C}}\mathbf{y} + \overline{\mathbf{K}}\mathbf{y} = \overline{\mathbf{F}} \tag{6.2}$$

where $\overline{\mathbf{M}} = \mathbf{P}^{\mathrm{T}}\mathbf{M}\mathbf{P}$, $\overline{\mathbf{C}} = \mathbf{P}^{\mathrm{T}}\mathbf{C}\mathbf{P}$, and $\overline{\mathbf{K}} = \mathbf{P}^{\mathrm{T}}\mathbf{K}\mathbf{P}$ are the modal mass matrix, damping matrix, and stiffness matrix, respectively. They are m *by* m diagonal matrices; $\overline{\mathbf{F}} = \mathbf{P}^{\mathrm{T}}\mathbf{F}$ is modal force; $\mathbf{x} = \mathbf{P}\mathbf{y}$, where $\mathbf{P}$ is mode shape, which is an n *by* m matrix; n is the total number of degrees of freedom (DOF); and m is the number of modes.

Equation(6.1) is decoupled as single-degree-of-freedom systems through the modal coordinates:

$$m_i\ddot{y}_i + c_i\dot{y}_i + k_i y_i = \bar{f}_i \quad (i = 1,\ldots,m) \tag{6.3}$$

where m_i, c_i, and k_i are the diagonal elements of matrices $\overline{\mathbf{M}}$, $\overline{\mathbf{C}}$, and $\overline{\mathbf{K}}$, respectively.

The transfer function for Eq.(6.3) is

$$G_i(s) = \frac{y_i(s)}{\bar{f}_i(s)} = \frac{1/m_i}{s^2 + 2\zeta_i\omega_{n,i}s + \omega_{n,i}{}^2} \quad (i = 1,\ldots,m) \tag{6.4}$$

where $\zeta_i = \dfrac{c_i}{2m_i\omega_{n,i}}$ is the damping ratio for the i^{th} mode, $\omega_{n,i} = \sqrt{\dfrac{k_i}{m_i}}$ is the natural frequency for the i^{th} mode.

From Eq.(6.4),

$$y_i(s) = G_i(s)\bar{f}_i(s) \qquad (i = 1,...,m) \tag{6.5}$$

In matrix form, Eq.(6.5) becomes

$$\mathbf{Y}(s) = \mathbf{G}(s)\bar{\mathbf{F}}(s) \tag{6.6}$$

Due to $\mathbf{X}(s) = \mathbf{P}\mathbf{Y}(s) = \mathbf{P}\mathbf{G}(s)\bar{\mathbf{F}}(s) = \mathbf{P}\mathbf{G}(s)\mathbf{P}^{\mathrm{T}}\mathbf{F}(s)$, the transfer function for the spindle system is obtained as follows:

$$\mathbf{H}(s) = \frac{\mathbf{X}(s)}{\mathbf{F}(s)} = \mathbf{P}\mathbf{G}(s)\mathbf{P}^{\mathrm{T}} \tag{6.7}$$

Each element in the transfer function matrix $\mathbf{H}(s)$ has the form

$$h_{jk} = \frac{x_j(s)}{F_k(s)} = \sum_{i=1}^{m} P_{ji}P_{ki}G_i(s) = \sum_{i=1}^{m} \frac{u_{ji}u_{ki}}{s^2 + 2\zeta_i\omega_{n,i}s + \omega_{n,i}^2} \tag{6.8}$$

where u_{ji} is the element of the mass normalized mode shape u .

The imaginary part of FRF at the tool tip for a typical spindle is shown in Figure 6-1.

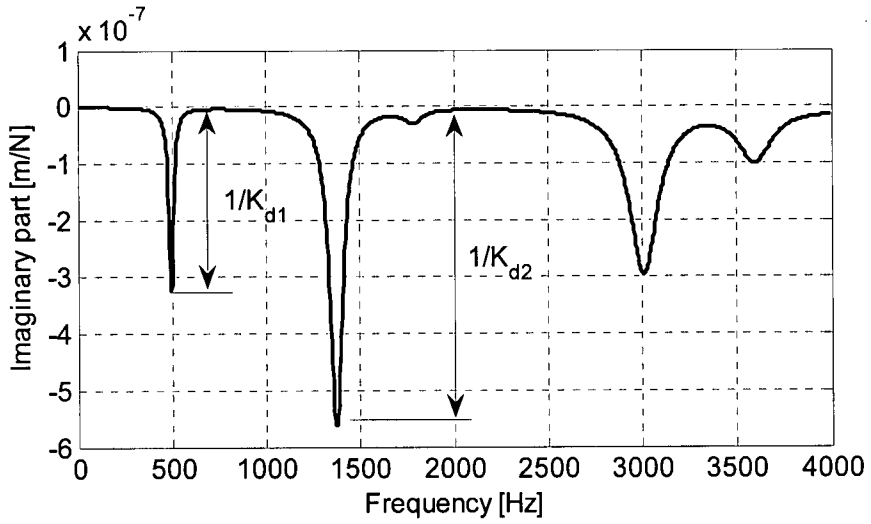

Figure 6-1: A typical FRF for a spindle

The dynamic stiffness is defined as:

$$K_{di} = \frac{1}{\left|\left(G_{imag}\right)_i\right|} \tag{6.9}$$

where G_{imag} is the imaginary part of the FRF at the tool tip or the spindle nose and i is the mode number, which means each mode has its own dynamic stiffness.

6.3 Chatter-free Spindles

Productivity is often limited because of chatter vibrations, which depend on cutting conditions and the dynamic properties at the tool tip of the spindle. The cutting conditions include the tool geometry, work-piece material, machining methods, and spindle speeds. In order to decide whether cutting is stable or unstable, the chatter stability lobe is developed. Figure 6-2 shows a typical stability lobe for milling. If the machine runs under the stability lobe curve, the cutting is stable. Otherwise, it is unstable. For example, at point B, with a lower spindle speed and a smaller depth of cut, cutting is unstable. However, at point A, with a higher spindle speed and a larger depth of cut, cutting is still stable. The productivity at cutting point A, of course, is much higher than at point B.

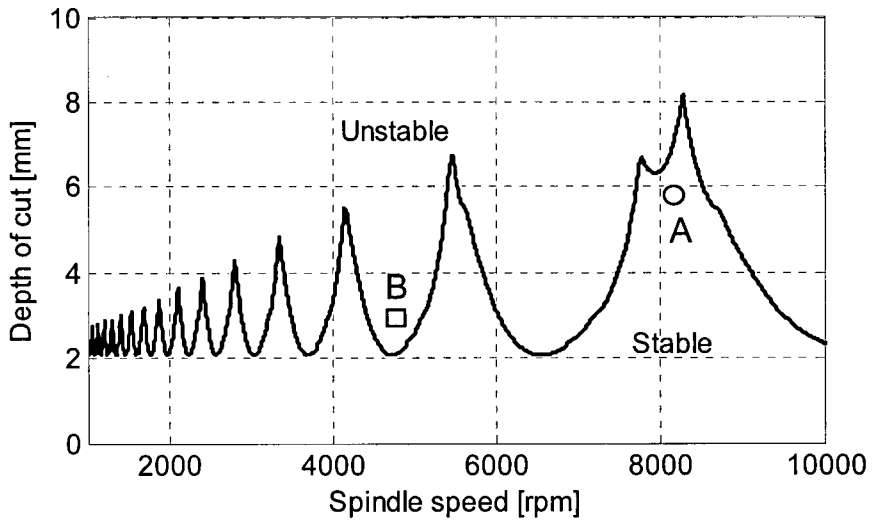

Figure 6-2: A typical stability lobe for milling

Once the cutting conditions are fixed, for example, for the special purpose spindle, the stability lobes are affected only by the dynamic properties at the tool tip. Therefore, the

dynamics of the spindle system can be tuned to avoid chatter vibrations under the desired operating conditions. Such a spindle is called a "chatter-free" spindle.

6.4 Optimization for the Maximum Depth of Cut

Since the objective function is highly non-linear, the sequential quadratic programming (SQP) method in MatLab [71] is used in this thesis. Its iterative format can be expressed as

$$\mathbf{x}_{k+1} = \mathbf{x}_k + \alpha^* \mathbf{d} \tag{6.10}$$

where k is the iteration number, $\mathbf{x}_{k+1}$ is the new design variable vector, $\mathbf{x}_k$ is the current design variable vector, $\mathbf{d}$ is a vector search direction, and α^* is the scalar quantity that defines the distance moving in direction $\mathbf{d}$. The optimization procedure is illustrated in Figure 6-3.

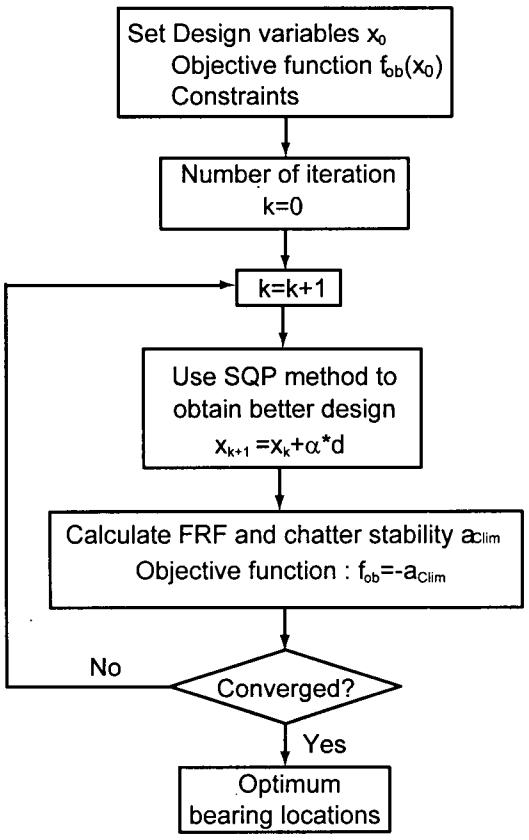

Figure 6-3: The flowchart of optimization

The cutting conditions, namely the depth of cut and the spindle speed; must be selected under the stability lobes in order to avoid chatter vibrations in metal cutting. The locations of stability pockets depend on the natural frequencies of the spindle system, while the allowable depth of cut is determined by the dynamic stiffness of each mode at the tool tip. The proposed method automatically tunes the spindle modes in such a way that chatter vibration-free pockets of stability are created at the desired spindle speed, and the depth of cut or the dynamic stiffness is maximized. Tuning of the spindle dynamics is achieved by optimizing the distribution of bearings along the spindle shaft.

When the critical depth of cut (a_{Clim}) of the stability lobes at the desired cutting spindle speed shown in Figure 6-4 is maximized, cutting is the most stable. Therefore, the objective function (f_{ob}) is defined as follows:

$$\text{Minimize: } f_{ob} = -\sum_{i=1}^{N} W_i \left(a_{Clim}\right)_i \quad (i = 1,2,...,N_t) \tag{6.11}$$

where W_i and $\left(a_{Clim}\right)_i$ are the weight and critical depth of cut for the i^{th} cutter, respectively, and N_t is the total number of cutters with different flutes.

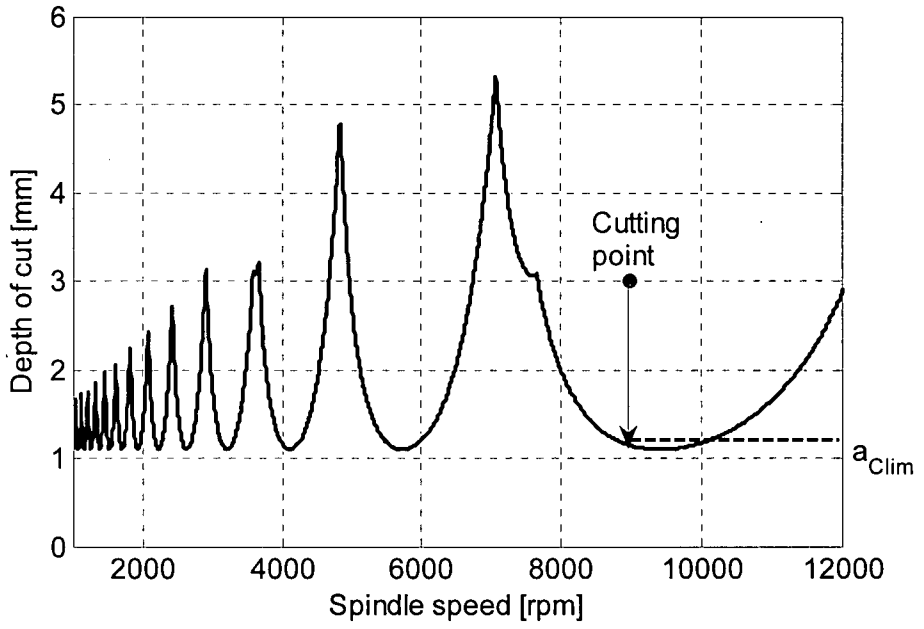

Figure 6-4: Stability lobe of milling

Critical depth of cut a_{Clim} for milling is calculated using the chatter-stability theory developed by Budak-Altintas [61][62]:

$$a_{lim} = \frac{-2\pi\Lambda_R}{N_t K_{tc}}\left(1+\left(\frac{\Lambda_I}{\Lambda_R}\right)^2\right) \tag{6.12}$$

where K_{tc} is the cutting coefficient and N_t is the number of flutes. Λ_R and Λ_I are real and imaginary values of an eigenvalue Λ, which is obtained using the FRF at the tool tip. The details of chatter-stability theory can be found in [54, 60]-[62].

6.4.1 Design Variables

The design variables used here are the bearing spans. The number of the design variables depends on the bearing arrangement and transmission type. The model of a motorized spindle with a tool is shown in Figure 6-5. The spindle has four bearings in the front and one in the rear. The tool, tool-holder, and spindle shaft are assumed to be rigidly connected, and are modeled as Timoshenko beams. The outer rings of the bearings are fixed. The six design variables $(X_1, X_2, .., X_6)$ are defined in Figure 6-6. The required cutting conditions are listed in Table 6-1.

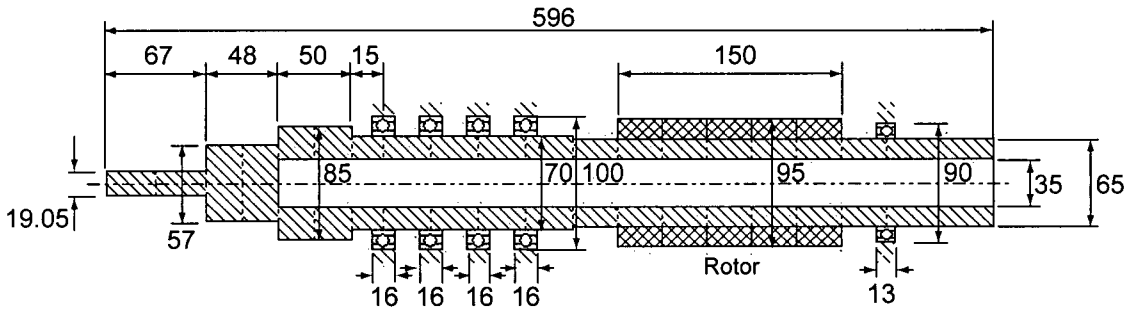

Figure 6-5: A motorized spindle

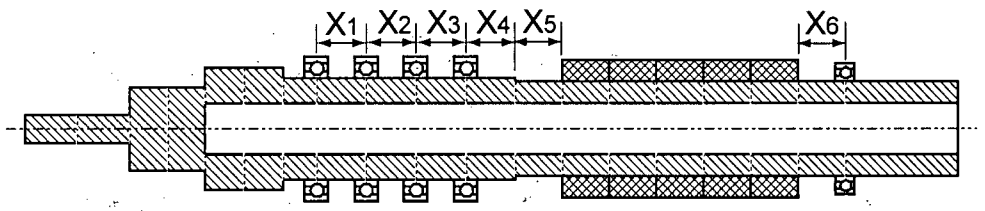

Figure 6-6: Design variables for bearing locations

Table 6-1: Required cutting parameters

Cutter diameter	19.05 [mm]
Number of flutes	4
Material to be cut	AL7075-T6
Spindle speed	9000 [rpm]
Minimum depth of cut	3 [mm]
Feed rate	0.1 [mm/flute]
Milling type	Slotting

6.4.2 Initial Conditions and Constraints

In order to avoid a local minimum value of the objective as opposed to the global minimum value of the objective, three different initial conditions are used, and the final design is chosen from the three emerging optimal solutions. The constraints for bearing locations are listed in Table 6-2.

Table 6-2: Constraints on bearing locations

X_1, X_2, X_3, X_4	≥22 [mm]
X_5	≥20 [mm]
X_6	≥10 [mm]

6.4.3 Optimal Results

The Sequential Quadratic Programming (SQP) algorithm is used to optimize the bearing locations. The gradients of the objective function f_{ob} and the Hessian matrix cannot be calculated analytically; they are obtained using a numerical differentiation and a Quasi-Newton method, respectively. The BFGS (Broyden-Fletcher-Goldfarb-Shanno) approximation technique is used to update the Hessian matrix [71].

Figure 6-7 demonstrates the chatter-stability lobes for a single four-flute cutter computed from the three initial designs and the final optimized design. The desired spindle speed is 9000 rpm, and the depth of cut is 3 mm. Cutting is not stable for all three initial designs, but

it becomes stable after optimization. The optimized spindle configuration is shown in Figure 6-8.

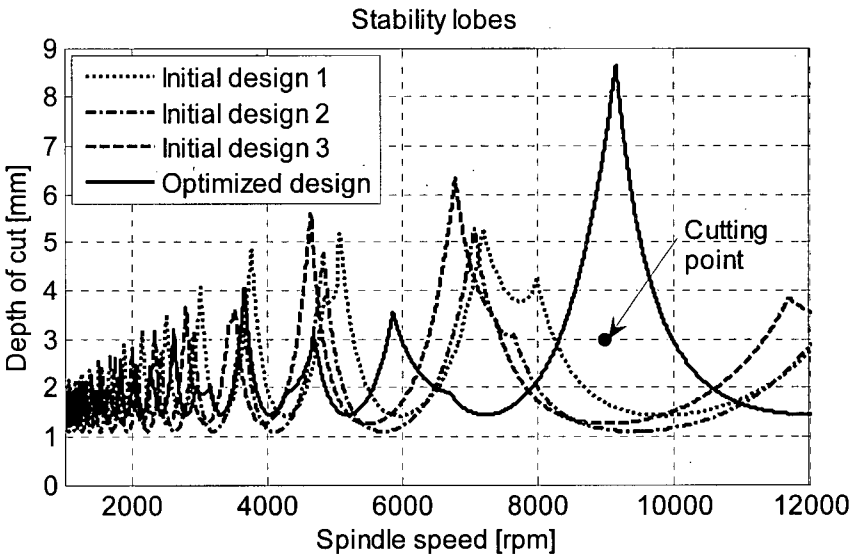

Figure 6-7: Stability lobes for initial and optimized designs with a single cutter

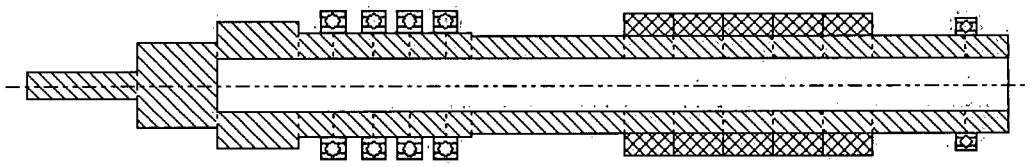

Figure 6-8: Optimized spindle model with single cutter

The proposed method is also suitable for the optimization of spindles using multiple cutters with different flutes. The same spindle and cutting conditions described above are used, but three cutters with two, three, and five flutes are applicable to the spindle. Only the first initial design is considered here.

Figure 6-9 and Figure 6-10 show the stability lobes for the original and optimized designs respectively. In the original design, cutting is not stable for the five-flute cutter, and is close to the unstable regions for two-flute and three-flute cutters. However, after optimization, there are very big margins for the two-flute and three-flute cutters, and cutting becomes stable for the five-flute cutter, although it is close to the unstable region. The optimized spindle configuration is displayed in Figure 6-11.

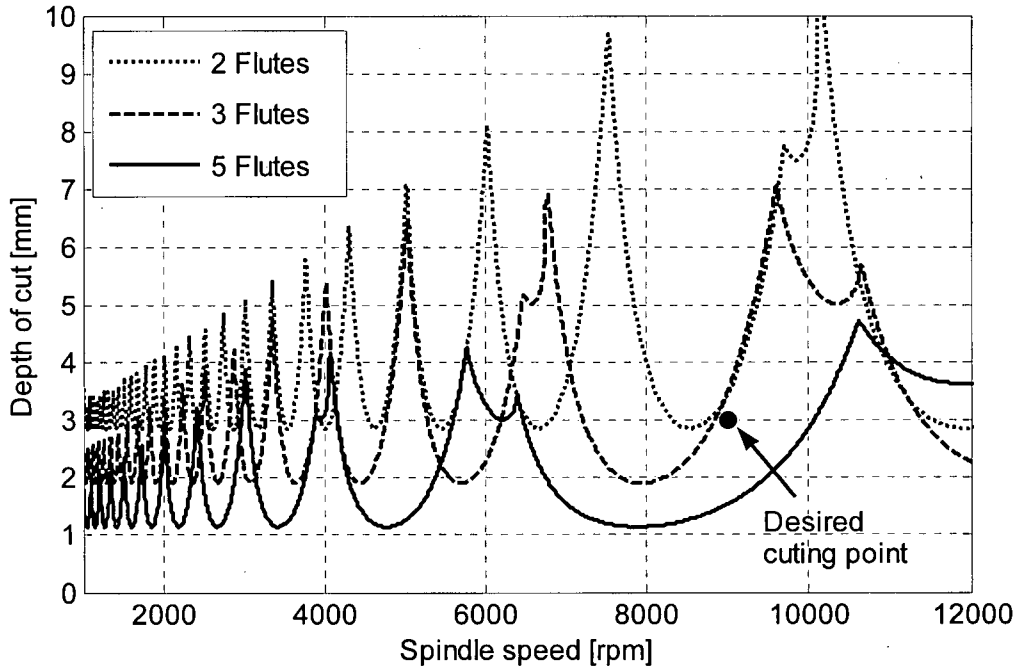

Figure 6-9: Stability lobes for the initial design with multiple cutters

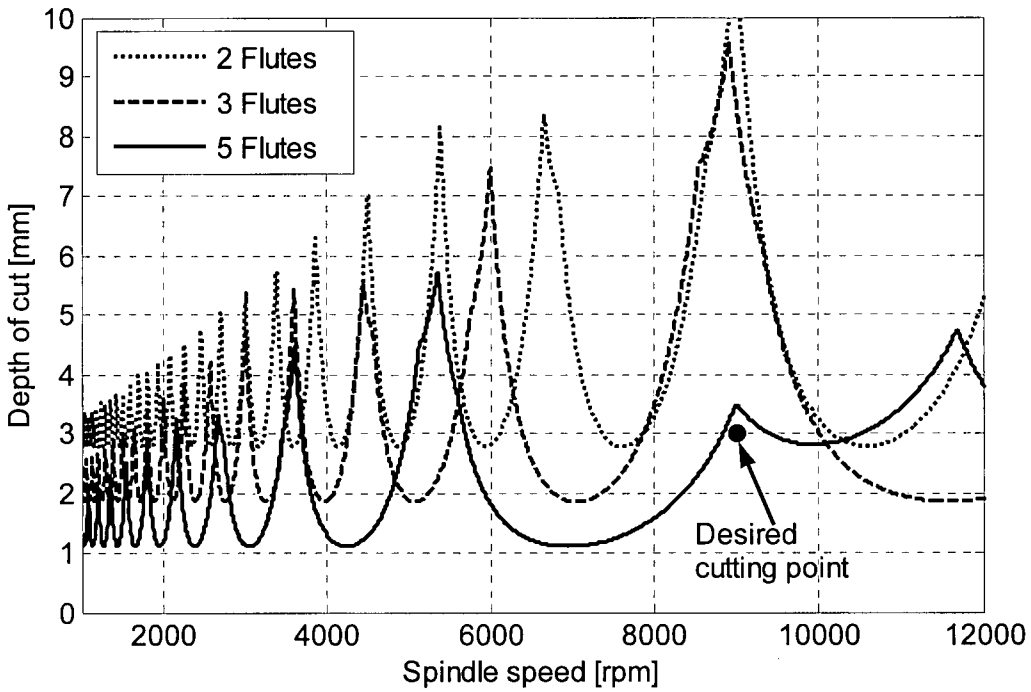

Figure 6-10: Stability lobes for the optimized design with multiple cutters

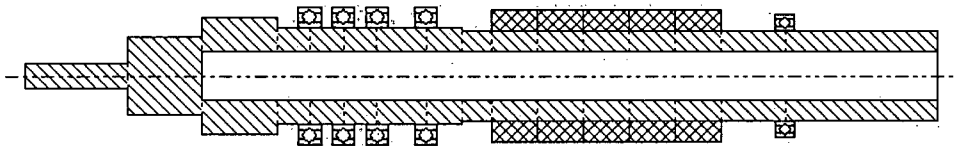

Figure 6-11: Optimized spindle model with multiple cutters

6.5 Optimization for Maximum Dynamic Stiffness of the Spindle

The same idea as was used in optimization for maximum depth of cut is applied to maximize the dynamic stiffness of the spindle system. The objective function (f_{ob}) is defined as follows:

$$\text{Minimize: } f_{ob} = -\sum_{i=1}^{N} W_i (K_d)_i \quad (i = 1,2,...,m) \tag{6.13}$$

where W_i is the weight function, $(K_d)_i$ is the dynamic stiffness for the i^{th} mode, and m is the total number of dominant modes.

A motorized spindle with a tool on it is shown in Figure 6-12. The FE model is illustrated in Figure 6-13. The bearing stiffness is provided by the manufacturer, i.e., 4.34E8 N/m for radial stiffness of the two front bearings and 3.77E8 N/m for the two rear bearings. The tool, tool-holder, and spindle shaft are assumed to be rigidly connected, and are modeled as Timoshenko beams. The outer rings of the bearings are fixed. The modal damping used in the simulation is from experiment by using least square curve fitting. The natural frequencies and dynamic stiffness from both experiment and simulation are listed in Table 6-3. The first three mode shapes are presented in Figure 6-14 to Figure 6-16. The simulated FRF is shown in Figure 6-17.

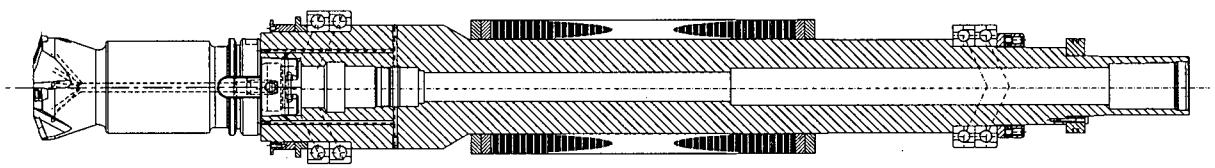

Figure 6-12: A motorized spindle with a cutter

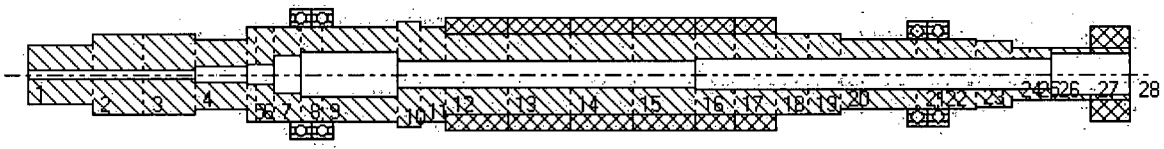

Figure 6-13: The finite element model for the motorized spindle with a cutter

Table 6-3: The natural frequencies and dynamic stiffness

Mode#	Measurement		Simulation	
	Nat. Freq. (ω_n) [Hz]	Dynamic Stiffness ($2k\zeta$) [N/μm]	Nat. Freq. (ω_n) [Hz]	Dynamic Stiffness ($2k\zeta$) [N/μm]
1 (ζ=4%)	365	4.0	360	4.3
2 (ζ=4%)	719	5.0	723	5.5

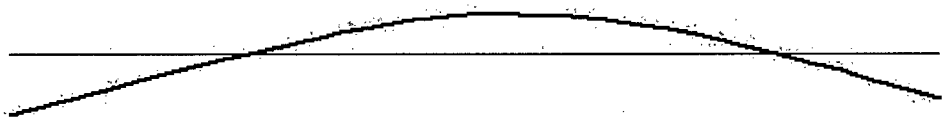

Figure 6-14: Mode #1 at 360 Hz

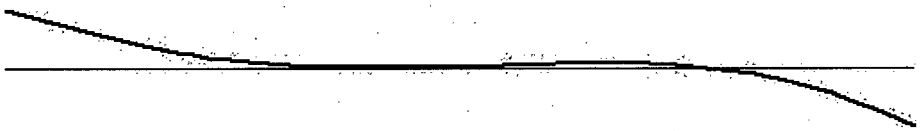

Figure 6-15: Mode #2 at 723 Hz

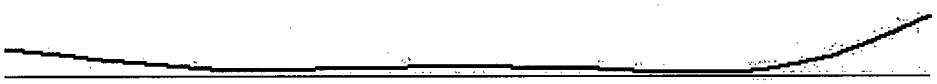

Figure 6-16: Mode #3 at 820 Hz

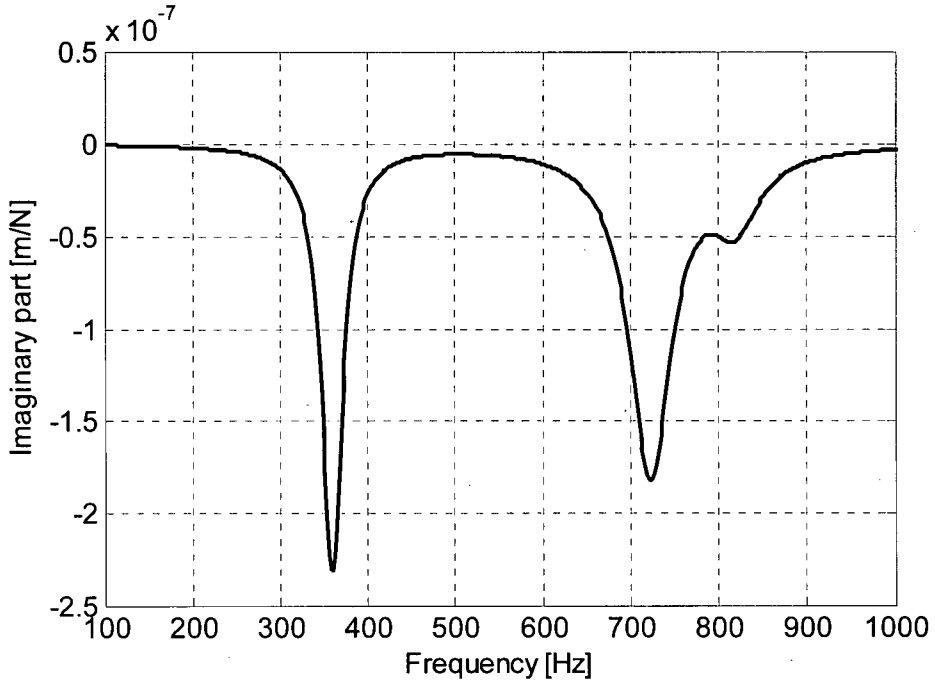

Figure 6-17: Imaginary part of FRF at the tool tip

It is clear from the mode shapes that the closer the front bearings are to the tip of the tool, the higher the dynamic stiffness at the tool tip. However, in practice the front bearings cannot be too close to the spindle nose. Therefore, three possible methods are used to obtain the maximum dynamic stiffness at the tool tip. First, one or two additional bearings can be added between the front bearings and the motor; second, the locations of the rear bearings can be optimized; third, bearing stiffness can be adjusted through preload.

In this example, the total number of bearings is kept the same. The design variables and their constraints are shown in Figure 6-18 and listed in the Table 6-4.

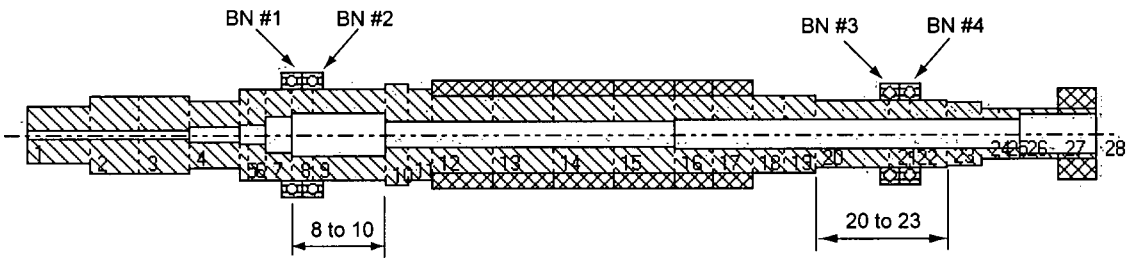

Figure 6-18: Design variables and constraints

Table 6-4: Design variables and constraints

Design Variables		Description	Constraints	
No.	Initial Values		Low limit	Upper limit
X_1	234 [mm]	Bearing No.1 (BN #1) at node 8	Node 8	Node 10
X_2	252 [mm]	Bearing No.2 (BN #2) at node 9	Node 8	Node 10
X_3	762 [mm]	Bearing No.3 (BN #3) at node 21	Node 20	Node 23
X_4	780 [mm]	Bearing No.4 (BN #4) at node 22	Node 20	Node 23
X_5	4.34E8 [N/m]	Bearing stiffness of BN #1 and BN #2	2E8 [N/m]	5E8 [N/m]
X_6	3.77E8 [N/m]	Bearing stiffness of BN #3 and BN #4	2E8 [N/m]	5E8 [N/m]

Note: Only bending vibration is considered in this example, therefore, only radial bearing stiffness is used as the design variable. There is a relationship between the axial and radial bearing stiffness.

The SQP method is used to maximize dynamic stiffness. The front bearing locations are kept the same after optimization, while the rear bearings are moved towards the motor side, as shown in Figure 6-19. The optimized design variables are listed in Table 6-5. A comparison of the natural frequencies and dynamic stiffness before and after optimization is presented in Table 6-6.

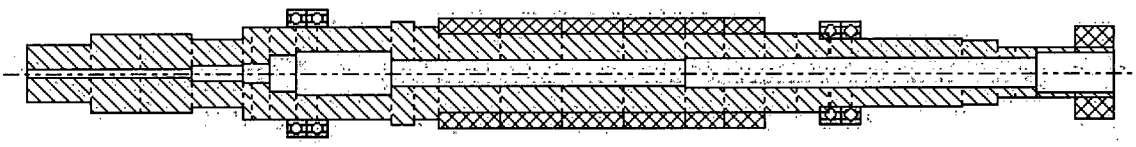

Figure 6-19: Optimized bearing locations

Table 6-5: Comparison between initial and optimized design variables

Design Variables		
No.	Initial Values	Optimized Values
X_1	234 [mm]	234 [mm]
X_2	252 [mm]	252 [mm]
X_3	762 [mm]	699 [mm]
X_4	780 [mm]	717 [mm]
X_5	4.34E8 [N/m]	4.88 E8 [N/m]
X_6	3.77E8 [N/m]	3.07 E8 [N/m]

Table 6-6: Comparison of the natural frequencies and dynamic stiffness

Mode#	Original design		Optimized design	
	Nat. Freq. (ω_n) [Hz]	Dynamic Stiffness ($2k\zeta$) [N/μm]	Nat. Freq. (ω_n) [Hz]	Dynamic Stiffness ($2k\zeta$) [N/μm]
1 (ζ=4%)	360	4.3	402	6.0
2 (ζ=4%)	723	5.5	592	9.8
2 (ζ=4%)			808	7.4

The comparison of the FRF at the tool tip before and after optimization is shown in Figure 6-20. Optimization not only makes the first natural frequency higher, but also increases the dynamic stiffness. However, an extra mode at 592Hz is introduced. The designer can decide on the final design scheme depending on the application.

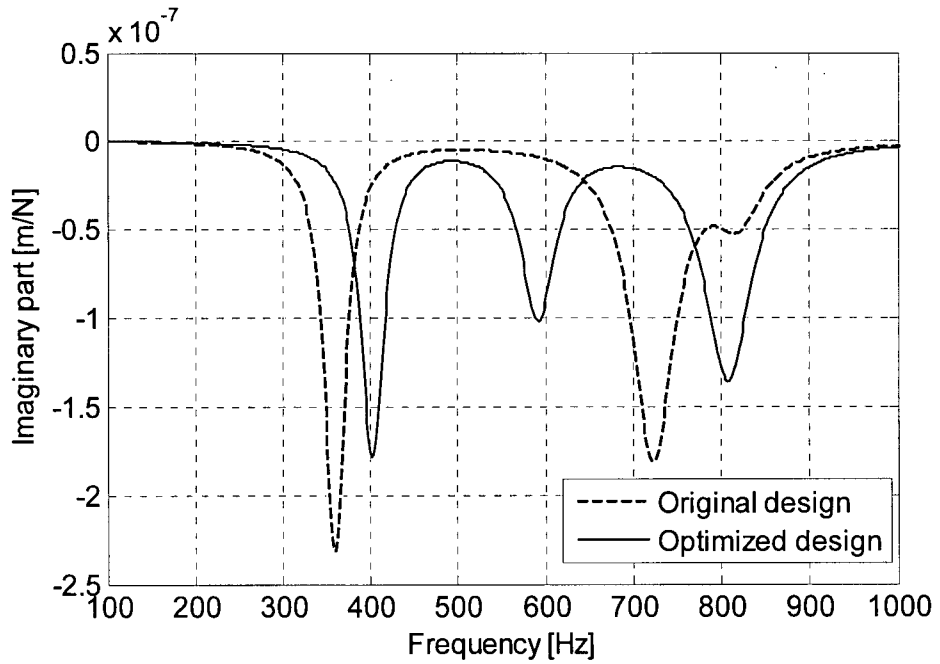

Figure 6-20: Comparison of the FRF at tool tip before and after optimization

6.6 Summary

A general optimization method for spindle design has been presented in this chapter, involving dynamics of the spindle system, cutting mechanics, and chatter-vibration theory. The objective functions can be the depth of cut or the dynamic stiffness at the tool tip. The

design variables include bearing location and bearing stiffness, which is adjusted by preload during the assembly of spindles. Weight functions are introduced for multiple flute cutters and the dynamic stiffness of multiple modes. The sequential quadratic programming (SQP) method is used for optimization, and which is achieved by automatically tuning the spindle modes in such a way that chatter vibration-free-pockets of stability lobes are created at the desired spindle speed.

Chapter 7
Conclusion

7.1 Conclusion

In this thesis, a general method has been developed for modeling the spindle-bearing system, which consists of the spindle shaft, angular contact ball bearings, and the spindle housing. The model is integrated with the machine-tool model to simulate the cutting process in a virtual environment. All of the proposed models are verified experimentally by conducting comprehensive tests on an industrial-sized spindle. These tests range from static analysis to dynamic simulation, simple boundary conditions of the free-free case to the complex conditions on the machine tool, and from frequency domain analysis conducted by performing impact tests to the time domain simulation conducted by measuring the time history of responses under impact or cutting forces.

The contributions in this thesis are summarized as follows:

(1) The equations of motion for the rotating spindle shaft and disk are modeled as Timoshenko beams, which include the axial force, centrifugal force, and gyroscopic moment. They represent the most complete mathematical model reported in the literature for describing spindle dynamics. The finite element method is used for discretizing the continuous model, establishing the finite element representation of the spindle system.

(2) A two-node nonlinear finite element with ten degrees of freedom is formulated for the angular contact ball bearing, based on Jones' complex bearing model. Jones' model includes both centrifugal forces and gyroscopic moments from the rolling balls of the bearings. This thesis expands Jones' model to include deformation of the spindle housing, which significantly affects the dynamics of the spindle system. In comparison, most research used simplified bearing models that neglect either centrifugal forces or gyroscopic moments that make the model highly nonlinear and difficult to achieve a convergent solution. The spindle housing was not included in all previous models. Spindle dynamics is therefore isolated from the machine tool, making the models valid only for very small and flexible spindle shafts.

(3) The thesis presents the first general formulation of the spindle system which integrates a nonlinear bearing model into a finite element model of the spindle shaft and housing. The proposed model is suitable for any preload mechanism, bearing arrangement, and is applicable to both low- and high-speed spindles. It is therefore a general model.

(4) Bearing stiffness is evaluated under different preloads, and verified by comparing the displacements obtained at the spindle nose from both simulation and experiment. Frequency response functions (FRF) are also simulated, and are verified by performing impact tests with the spindle suspended in the air to simulate the free-free boundary condition.

(5) The effect of machine-tool dynamics on the spindle system presented in this thesis is unique in the literature, and is achieved as follows. First, a simplified model representing the dynamics of the whole machine tool without the spindle is developed by means of experimental modal analysis. Then the model of the whole machine-tool system is created by coupling the spindle with the simplified model of the machine. The proposed method is validated by performing impact hammer tests and cutting experiments. Experimental results show that the dynamics of the machine-tool structure and spindle machine tool assembly joints have a significant effect on predicting the dynamic response of the machine-tool spindles. However, previous research did not include this effect; natural frequencies were experimentally proven, but not the frequency response functions. The performance of the spindle is not measured with the natural frequencies, but with the accurate prediction of the FRF of the spindle, which contain mode shapes and the dynamic stiffness of each mode. Dynamic stiffness is used to assess how deep the material can be cut without chatter, and the mode shapes are essential for optimal design of the shaft and bearing locations.

(6) A numerical model of the spindle machine-tool system is developed. This is the first study in literature that simulates the virtual cutting performance of the spindle system, with the influence of the machine-tool structure, bearing preload, speed effects, and the cutting process incorporated. The static and dynamic deflections along the cutter and spindle shaft, as well as contact forces on the bearings, are predicted with simulated cutting forces before physically building and testing the spindles. The simulated

displacement responses at the tool-holder compare favorably well against experimental measurements conducted on the machine. The predicted stability lobes for milling operations are proven by chatter tests. The experimentally proven virtual testing of the spindle during cutting requires accurate modeling of the spindle, bearings, and machine-tool mounting dynamics, and is an original contribution to the literature.

(7) It is shown that the preload can increase bearing stiffness, which leads to increased natural frequencies. Therefore, the stability lobes shift to the right. However, higher preload usually reduces the damping, which decreases the critical depth of cut. The preload cannot efficiently improve the stability lobes but it can enhance static stiffness and reduce forced vibration. The most efficient method of increasing the critical depth of cut is to add damping to the spindle system.

(8) The thesis demonstrates that increased spindle speed leads to reduced bearing stiffness, which lowers the natural frequencies and causes the stability lobes to shift to the left (i.e., lower speed). The speed effects are very obvious at higher spindle speeds and lower preloads.

(9) The tool-holder interface with the spindle shaft is claimed to be the main source of vibration in machining. However, this influence depends on the types of tool-holder used. Both simulated and experimental results show that the shrink-fit tool-holder interface has a negligible effect on the dynamics of the spindle system, and that the rigid connection between the shrink-fit tool-holder and the spindle shaft can be used in modeling spindle systems.

(10) The dynamic stiffness of spindle systems and the chatter-free depth of cut are introduced in this thesis as optimal design objectives. The number of teeth on the cutter and the influence of the work-piece material properties are considered in optimization of the bearing locations. The proposed approach and model has not been previously reported in the literature except in the author's research [52].

The methods developed in this thesis are for general application purposes, and can be used in both research and industrial design. They are also applicable to general rotating shafts used in turbines, electrical generators, and automotive applications.

7.2 Future Research Directions

Due to speed limitations of the spindle and machine tool, spindle effects are not experimentally verified at above 10,000 rpm in this thesis. Therefore, the first thing to do in future research is to experiment with higher speed machines.

The Timoshenko beam theory is used in this thesis to model both the spindle shaft and spindle housing. This approach is valid for most cases. However, when the preload is very small, even reaching zero in some cases, the model is no longer accurate. The reason is that the deflection of the beam has no effect on axial deformation in beam theory. In practice, when the spindle is deformed under cutting forces, it also shows deformation in the axial direction. The axial deformation at bearing locations will cause the bearing to be preloaded. This is why spindles without preload can still work in practical applications, but are not recommended. In order to solve this problem, 3D solid element has to be used in modeling the spindle system; however, the simulation times will increase significantly.

The thermal effect is an issue in spindle design. Thermal expansion changes the dimensions of the spindle structures, the bearing stiffness, and the dynamics of the spindle. However, experiments demonstrate that the thermal effect on the dynamics of the spindle system is negligible if the spindle is cooled properly, which is the case with most high-speed spindles. However, it is still important to model thermal effects in order to design more optimal cooling strategies for spindles.

In this thesis, the model of the machine tool without the spindle on it is modeled by experimental modal analysis. In the design stage, a digital model of the machine is needed in order to simulate the cutting process in a virtual environment. Therefore, modeling of the whole machine tool and testing its performance in a virtual environment is another direction for future research.

References

[1] Altintas, Y., Weck, M., 2004, "Chatter stability of metal cutting and grinding", Annals of CIRP, vol. 53/2, pp. 619-642.

[2] Taha, M. M. A., and Crookall, J. R., 1977, "Rolling bearing for machine tools comparative evaluation by a new experimental technique and finite element analysis," Int. J. Mach. Tool Des. Res., Vol.17, pp.179-190.

[3] The Barden Co, 2000, "BARDEN/FAG CRONIDUR® 30 Hybrid Spindle Bearings," Precision Bulletin, No.18

[4] Palmgren, A., 1959, Ball and Roller Bearing Engineering, Burkbank.

[5] Jones,A.B., 1960, "A general theory for elastically constrained ball and radial roller bearings under arbitrary load and speed conditions," AMSE Journal of Basic Engineering, pp.309-320.

[6] DeMul,J.M., Vree,J.M., and Mass,D.A., 1989, "equilibrium and association load distribution in ball and roller bearings loaded in five degrees of freedom while neglecting friction, part 1: general theory and application to ball bearings," ASME J. Tribology,Vol.111, pp.142-148.

[7] Filiz,I.H., and Gorur,G.,1994, "Analysis of preloaded bearings under combined axial and radial loading," International Journal of Machine Tools and Manufacture. Vol.34, n1, pp.1-11.

[8] Lim,T.C., and Singh,R., 1992, "Vibration transmission through rolling element bearings, Part IV. Statistical energy analysis," Journal of Sound and Vibration. Vol.153, n1, pp.37-50.

[9] Ryan,S.G., 1997, "modeling of rolling element bearing mechanics-computer program updates," Marshall Space Flight Center, NASA technical memorandum 108532.

[10] Houpert, L., 1997, "A uniform analytical approach for ball and roller bearings calculations," ASME J. Tribol. Vol.119, pp.851-858.

[11] Hernot, X., Sartor, M. and Guillot, J., 2000, "Calculation of the stiffness matrix of angular contact ball bearings by using the analytical approach, " Journal of Mechanical Design, Transactions of the ASME.Vol.122, n1, pp.83-90.

[12] Harris,T.A., Rolling Bearing Analysis, 4th ed., John-Wiley, 2001

[13] Walford, T.L.H., and Stone, B.J., 1980, "The measurement of the radial stiffness of rolling element bearing under oscillation condition," Journal of Mechanical Engineering Science, Vol.22, n4, pp.175-181.

[14] Walford,T.L.H., and Stone,B.J.,1983, "The sources of damping in rolling element bearing under oscillation condition," Proc. Instn. Mech. Engrs., Vol.197, pp.225-232.

[15] Tiwari,R., and Vyas,N.S., 1995, "Estimation of non-linear stiffness parameters of rolling element bearings from random response of rotor-bearing systems," Journal of Sound and Vibration, Vol.187, n2, pp.229-239.

[16] Marsh,E.R., and Yantek,D.S., 1997, "Experimental measurement of precision bearing dynamic stiffness," Journal of Sound and Vibration, Vol.202, n1, pp.55-66.

[17] Kraus, J., Blech, J.J., and Braun, S.G., 1987, "In situ determination of rolling bearing stiffness and damping by modal analysis," ASME J. Vibration and Acoustics, Vol.109, pp.235-240.

[18] Wang, K.W., Shin, Y.C., and Chen, C.H., 1991, "On the natural frequencies of high-speed spindles with angular contact bearings," Proc. Instn. Mech. Engrs. Vol.205, pp.147-154.

[19] Shin, Y.C., 1992, "Bearing nonlinearity and stability analysis in high speed machining," ASME Journal of Engineering for Industry, pp.23-30.

[20] Gibson, A.O., 1999, "Modeling and estimation of thermally induced bearing loads in machine tool spindles," Ph.D. thesis, The University of Michigan.

[21] Bollinger, J.G., and Geiger, G., 1964, "Analysis of the static and dynamic behavior of lathe spindles," Int. J. Mach. Tool Des. Res., Vol.3, pp.193-209.

[22] Yang Shuzhi, 1981, "A study of the static stiffness of machine tool spindles," Int. J. Mach. Tool Des. Res., Vol.21,n1, pp.23-40.

[23] Wardle, F.P., Lacey, S.J., and Poon, S.Y., 1983, "Dynamic and static characteristics of a wide spread range machine tool spindle," Precision Engineering, Vol.1, n3, pp.175-183.

[24] Aini, R., Rahnejat, H., and Gohar, R., 1990, "A five degrees of freedom analysis of vibrations in precision spindles," Int. J. Mach. Tools Manufact. Vol.30, n1, pp.1-18.

[25] Aini, R., Rahnejat, H. and Gohar, R., 1995, "Experimental investigation into bearing-induced spindle vibration," Proceedings of the Institution of Mechanical Engineers, Part C: Journal of Mechanical Engineering Science. Vol.209, n2, pp.107-114.

[26] Brandon, J. A., and Shareef, K.J.H., 1991, "On the validity of several common assumptions in the design of machine tool spindle-bearing systems," Int-J-Mach-Tools-Manufacture, Vol.31, n2, pp.235-248.

[27] Al-Shareef, K. J. H., and Brandon, J.A., 1990, "On the effects of variations in the design parameters on the dynamic performance of machine tool spindle-bearing systems," Int-J-Mach-Tools-Manuf, v30, n3, pp.431-445.

[28] El-Marhomy, A. A., 1999, "Dynamics and stability of elastic shaft-bearing systems with nonlinear bearing parameters," Heat and Mass Transfer, Vol.35, pp.334-344.

[29] Ruhl, R. L., and Booker, J.F., 1972, "A finite element model for distributed parameter turborotor systems," ASME Journal of Engineering for Industry, Feb., pp.128-132.

[30] Nelson, H. D., and McVaugh J.M., 1976, "The dynamics of rotor-bearing systems using finite elements," ASME J. Mech.Des. May, Vol.93, n2, pp.593-600.

[31] Nelson, H.D., 1980, "A finite rotating shaft element using Timoshenko beam theory," ASME J. Mech.Des. Vol.102, n4, pp.793-803.

[32] Ozguven, H., and Ozkan, L.Z., 1984, "Whirl speeds and unbalance response of multi-bearing rotors using finite elements," ASME Journal of Vibrations, Acoustics, Stress and Reliability in Design, Vol.106, n1, pp.72-79.

[33] Reddy, V.R., and Sharan, A.M., 1985, "Design of machine tool spindles based on transient analysis," ASME Journal of Mechanism, Transmissions, and Automation in Design, Vol.107, pp.346-352.

[34] Reddy, V.R., and Sharan, A.M., 1987, "Finite element modeled design of lathe spindles: the static and dynamic analysis," ASME Journal of Vibrations, Acoustics, Stress and Reliability in Design, Vol.109, n4, pp.407-415.

[35] Wang, W.R., and Chang, C.N., 1994, "Dyanmic analysis and design of a machine tool spindle-bearing system," ASME Journal of Vibration and Acoustics. Vol.116, n3, pp.280-285.

[36] Genta, G., 1996, "A harmonic finite element for the analysis of flexural, torsional and axial rotor-dynamic behavior of discs." Journal of Sound and Vibration, Vol.196, n1, pp.19-43.

[37] Choi, J.K., and Lee, D.G., 1997, "Characteristics of a spindle bearing system with a gear located on the bearing span," Int. J. Mach. Tools Manufact. Vol.37,n2, pp.171-181.

[38] Bordatchev, E.V., Orbana, P.E., and Rehorn, A., 2001, "Experimental analysis and modeling of the dynamic performance of machine tool spindle-bearing systems," Proceedings of SPIE, The International Society for Optical Engineering. Vol.4191, pp.92-103.

[39] Kang Y., Chang Y.P., Tsai J.W. et al, 2001, "Integrated "CAE" strategies for the design of machine tool spindle-bearing systems," Finite Elements in Analysis and Design. Vol.37, n6-7, pp.485-511.

[40] Chen, C.H., 1992, "An integrated approach toward the modeling and dynamic analysis of high-speed spindles", PhD thesis, The Pennsylvania State University.

[41] Chen, C.H., Wang, K.W., and Shin, Y.C., 1994, "An integrated approach toward the dynamic analysis of high-speed spindles, Part I: system model; Part II: dynamics under moving end load," Int. J. Vib. Acoust. Vol.116, n4, pp.506-522.

[42] Jorgensen, B.R. and Shin, Y.C., 1998, "Dynamics of spindle-bearing systems at high speeds including cutting load effects," Journal of Manufacturing Science and Engineering, Transactions of the ASME. Vol.120, n2, pp.387-394.

[43] Bossmanns, B., Tu, J.F., and Kamman, J., 1999, "Thermal model for high speed motorized spindles", International J. Mach. Tools Manuf., Vol.39, p 1345-1366.

[44] Lin, Chi-Wei, Tu, J.F., and Kamman, J., 2003, "An integrated thermo-mechanical dynamic model to characterize motorized machine tool spindles during very high speed rotation", International J. Mach. Tools Manuf., Vol.43, pp.1035-1050.

[45] Li, H. and Shin, Y. C., 2004 "Integrated dynamic thermo-mechanical modeling of high speed spindles, part 1: Model development" J. Manuf. Sci. and Eng., Transactions of the ASME, Vol.126, pp.148-158.

[46] Li, H. and Shin, Y. C., 2004 "Integrated dynamic thermo-mechanical modeling of high speed spindles, part 2: Solution Procedure and Validations" J. Manuf. Sci. and Eng., Transactions of the ASME, Vol.126, pp.159-168.

[47] Cao, Y. and Altintas, Y. 2004, "A general method for the modeling of spindle-bearing systems," J., Mech. Des., Transactions of the ASME, Vol.126, pp.1089-1104.

[48] Altintas, Y., Cao, Y., 2005, "Virtual design and optimization of machine tool spindles," Annals of CIRP, Vol.54/1, pp.379-382.

[49] Taylor S., Khoo B.T., Walton D., 1990, "Microcomputer optimization of machine tool spindle stiffness", International Journal of Machine Tool& Manufacturing, Vol.30, No.1, pp.151-159.

[50] Lee D., Choi D., 2000, "Reduced weight design of a flexible rotor with ball bearing stiffness chracteristics varying with rotational speed and load", Journal of Vibratiob and Acoustics, Transactions of ASME, Vol.122, No. 3, pp.203-208.

[51] Osamu, M. 2003, Expert Spindle Design System, M.A.Sc. Thesis, the University of British Columbia.

[52] Maeda, O., Cao, Y., and Altintas Y. 2005, "Expert spindle design system," International J. Mach. Tools Manuf., Vol.45, pp.537-548.

[53] Altintas, Y., 2000, Manufacturing Automation: Metal Cutting Mechanics, Machine Tool Vibrations, and CNC Design, Cambridge University Press.

[54] Tobias, S. A., 1965, Machine Tool Vibration, John Wiley, New York.

[55] Tlusty, J., and Polacek, M., 1963, "The stability of machine tools against self-excited vibrations in machining", International Research in Production Engineering, ASME, pp.465-474.

[56] Merritt, H. E., 1965, "Theory of self-excited machine tool chatter", ASME Journal of Engineering for Industry, Vol.87, pp.447-454.

[57] Opitz, H., and Bernardi, F., 1970, "Investigation and calculation of the chatter behavior of lathes and milling machines", Annals of CIRP, Vol.18, pp.335-343.

[58] Minis, I., Yanushevsky, T., 1993, "A new theoretical approach for the prediction of machine tool chatter in milling", ASME Journal of Engineering for Industry, Vol.115, pp.1-8.

[59] Altintas, Y., Budak E., 1995, "analytical prediction of stability lobes in milling", Annals of CIRP, 44/1:357-362.

[60] Budak, E., and Altintas, Y., 1998, "Analytical prediction of chatter stability in milling -Part I: general formulation", Journal of Dynamic Systems, Measurement, and Control, Transactions of the ASME, Vol.120, pp.22-30.

[61] Budak, E., and Altintas, Y., 1998, "Analytical prediction of chatter stability in milling - Part II: application of the general formulation to common milling systems", Journal of Dynamic Systems, Measurement, and Control, Transactions of the ASME, Vol.120, pp.31-36.

[62] Brewe, D. E., and Hamrock B. J., 1977, "Simplified solution for elliptical-contact deformation between two elastic solids." ASME J. Lub. Technology. Vol.99, pp.485-487.

[63] Greenwood J. A., 1997, "Analysis of elliptical Hertzian contacts." Tribology International. Vol. 30, No.3, pp.235-237.

[64] Muhlner Edmund, 1998, Integrated Analysis of Ball Bearings and Structures, Fortschr.-Ber. VDI Reihe 1 Nr. 295. Dusseldorf:VDI Verlag.

[65] Zeillinger, R. 1995, Analysis of Angular Contact Ball Bearings with BEACON, informal SKF-report, Steyr, September 1995.

[66] SpindlePro®, Manufacturing Automation Laboratory, The University of British Columbia.

[67] Rivin, E., 2000, "Tooling Structure - Interface between Cutting Edge and Machine Tool", Annals of CIRP, vol. vol.49/2, pp. 591-643.

[68] Namazi, M. 2005, Mechanics and Dynamics of Tool-Holder Spindle Interface, M.A.Sc. Thesis, the University of British Columbia.

[69] Shames, I. H., and Dym, C. L., 1985, Energy and Finite Element Methods in Structural Mechanics, Washington: Hemisphere Pub. Corp.

[70] Bathe, K. J., 1996, Finite Element Procedures, Prentice Hall.

[71] MatLab 7.0, The MathWorks, Inc.

Appendix A

Finite Element Formulation for Beam Equations (3.22)

For Eq.(3.22), the homogeneous form of the static equations of equilibrium for an unstressed uniform Timoshenko beam becomes:

$$\begin{aligned}
&EA\frac{\partial^2 u}{\partial x^2}=0\\
&\frac{\partial}{\partial x}k_s AG\left(\frac{\partial v}{\partial x}-\theta_z\right)=0\\
&\frac{\partial}{\partial x}k_s AG\left(\frac{\partial w}{\partial x}+\theta_y\right)=0\\
&-EI\frac{\partial^2\theta_y}{\partial x^2}+k_s AG\left(\frac{\partial w}{\partial x}+\theta_y\right)=0\\
&-EI\frac{\partial^2\theta_z}{\partial x^2}-k_s AG\left(\frac{\partial v}{\partial x}-\theta_z\right)=0
\end{aligned} \tag{A.1}$$

A.1 Weak Form of Integration

Multiply equations (3.22) by weighted functions W_1, W_2, W_3, W_4 *and* W_5, respectively, and integrate over the beam element length:

$$\begin{aligned}
&\int_0^L W_1\left\{\rho A\frac{d^2u}{dt^2}-EA\frac{\partial^2 u}{\partial x^2}-q_x\right\}dx=0\\
&\int_0^L W_2\left\{\rho A\frac{d^2v}{dt^2}-\frac{\partial}{\partial x}\left[k_s AG\left(\frac{\partial v}{\partial x}-\theta_z\right)-P_a\frac{\partial v}{\partial x}\right]-q_y-\Omega^2\rho Av\right\}dx=0\\
&\int_0^L W_3\left\{\rho A\frac{d^2w}{dt^2}-\frac{\partial}{\partial x}\left[k_s AG\left(\frac{\partial w}{\partial x}-\theta_y\right)-P_a\frac{\partial w}{\partial x}\right]-q_z-\Omega^2\rho Aw\right\}dx=0\\
&\int_0^L W_4\left\{\rho I\frac{d^2\theta_y}{dt^2}+\Omega\rho J\frac{d\theta_z}{dt}-EI\frac{\partial^2\theta_y}{\partial x^2}+k_s AG\left(\frac{\partial w}{\partial x}+\theta_y\right)-m_y\right\}dx=0\\
&\int_0^L W_5\left\{\rho I\frac{d^2\theta_z}{dt^2}-\Omega\rho J\frac{d\theta_y}{dt}-EI\frac{\partial^2\theta_z}{\partial x^2}-k_s AG\left(\frac{\partial v}{\partial x}-\theta_z\right)-m_z\right\}dx=0
\end{aligned} \tag{A.2}$$

Integrating some terms in equations (A.2) once by parts, we obtain the weak integration form for equation (3.22) as follows:

$$\int_0^L W_1 \rho A \frac{d^2u}{dt^2} dx + \int_0^L \frac{\partial W_1}{\partial x} EA \frac{\partial u}{\partial x} dx - \int_0^L W_1 q_x dx - F_{xi} W_1(0) - F_{xj} W_1(L) = 0$$

$$\int_0^L W_2 \rho A \frac{d^2v}{dt^2} dx + \int_0^L \frac{\partial W_2}{\partial x} \left[k_s AG \left(\frac{\partial v}{\partial x} - \theta_z \right) + P_a \frac{\partial v}{\partial x} \right] dx - \int_0^L W_2 q_y dx$$
$$- \int_0^L \Omega^2 \rho A v dx - F_{yi} W_2(0) - F_{yj} W_2(L) = 0$$

$$\int_0^L W_3 \rho A \frac{d^2w}{dt^2} dx + \int_0^L \frac{\partial W_3}{\partial x} \left[k_s AG \left(\frac{\partial w}{\partial x} + \theta_y \right) + P_a \frac{\partial w}{\partial x} \right] dx - \int_0^L W_3 q_z dx$$
$$- \int_0^L \Omega^2 \rho A w dx - F_{zi} W_3(0) - F_{zj} W_3(L) = 0 \qquad \text{(A.3)}$$

$$\int_0^L W_4 \rho I \frac{d^2\theta_y}{dt^2} dx + \int_0^L W_4 \Omega \rho J \frac{d\theta_z}{dt} dx + \int_0^L \frac{\partial W_4}{\partial x} EI \frac{\partial \theta_y}{\partial x} dx + \int_0^L W_4 k_s AG \left(\frac{\partial w}{\partial x} + \theta_y \right) dx$$
$$- \int_0^L W_4 m_y dx - M_{yi} W_4(0) - M_{yj} W_4(L) = 0$$

$$\int_0^L W_5 \rho I \frac{d^2\theta_z}{dt^2} dx - \int_0^L W_5 \Omega \rho J \frac{d\theta_y}{dt} dx + \int_0^L \frac{\partial W_5}{\partial x} EI \frac{\partial \theta_z}{\partial x} dx + \int_0^L W_5 k_s AG \left(\frac{\partial v}{\partial x} - \theta_z \right) dx$$
$$- \int_0^L W_5 m_z dx - M_{zi} W_5(0) - M_{zj} W_5(L) = 0$$

where

$$F_{xi} = -\left[EA \frac{\partial u}{\partial x} \right]_{x=0}; \qquad F_{xj} = \left[EA \frac{\partial u}{\partial x} \right]_{x=L}$$

$$F_{yi} = -\left[k_s AG \left(\frac{\partial v}{\partial x} - \theta_z \right) + P \frac{\partial v}{\partial x} \right]_{x=0}; \qquad F_{yj} = \left[k_s AG \left(\frac{\partial v}{\partial x} - \theta_z \right) + P_a \frac{\partial v}{\partial x} \right]_{x=L}$$

$$F_{zi} = -\left[k_s AG \left(\frac{\partial w}{\partial x} + \theta_y \right) + P \frac{\partial w}{\partial x} \right]_{x=0}; \qquad F_{zj} = \left[k_s AG \left(\frac{\partial w}{\partial x} + \theta_y \right) + P_a \frac{\partial w}{\partial x} \right]_{x=L}$$

$$M_{yi} = -\left[EI \frac{\partial \theta_y}{\partial x} \right]_{x=0}; \qquad M_{yj} = \left[EI \frac{\partial \theta_y}{\partial x} \right]_{x=L}$$

$$M_{zi} = -\left[EI \frac{\partial \theta_z}{\partial x} \right]_{x=0}; \qquad M_{zj} = \left[EI \frac{\partial \theta_z}{\partial x} \right]_{x=L}$$

are called force boundary conditions.

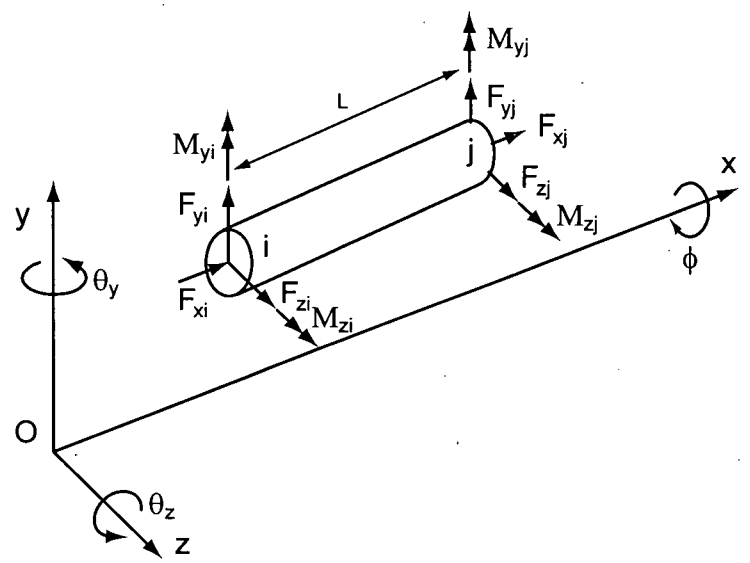

Figure A.1: Force boundary conditions for the beam element

A.2 Shape Functions

Assume the solutions for equations (A.3) as:

$$u = a_0 + a_1 x$$

$$v = b_0 + b_1 x + b_2 x^2 + b_3 x^3$$

$$w = c_0 + c_1 x + c_2 x^2 + c_3 x^3 \qquad \text{(A.4)}$$

$$\theta_y = d_0 + d_1 x + d_2 x^2$$

$$\theta_z = e_0 + e_1 x + e_2 x^2$$

The displacements u, v, w, θ_y *and* θ_z are expressed in terms of element nodal displacements $u_i, v_i, w_i, \theta_{yi}, \theta_{zi}$ and $u_j, v_j, w_j, \theta_{yj}, \theta_{zj}$. There are 16 unknowns in equations (A.4), which should satisfy both homogeneous equations (A.1) and element boundary conditions. After the constants in Eq.(A.4) are obtained, the equations (A.4) can be rewritten as follows:

$$\begin{bmatrix} u & v & w & \theta_y & \theta_z \end{bmatrix}^T = [N]\{q\} \qquad \text{(A.5)}$$

where $[N]$ is a matrix formed by shape functions, and $\{q\}$ is nodal displacement.

$$[N]=\begin{bmatrix}[N_u]\\ [N_v]\\ [N_w]\\ [N_{\theta y}]\\ [N_{\theta z}]\end{bmatrix}=\begin{bmatrix} N_{u1} & 0 & 0 & 0 & 0 & N_{u1} & 0 & 0 & 0 & 0\\ 0 & N_{t1} & 0 & 0 & N_{t2} & 0 & N_{t3} & 0 & 0 & N_{t4}\\ 0 & 0 & N_{t1} & -N_{t2} & 0 & 0 & 0 & N_{t3} & -N_{t4} & 0\\ 0 & 0 & -N_{\theta 1} & N_{\theta 2} & 0 & 0 & 0 & -N_{\theta 3} & N_{\theta 4} & 0\\ 0 & N_{\theta 1} & 0 & 0 & N_{\theta 2} & 0 & N_{\theta 2} & 0 & 0 & N_{\theta 3}\end{bmatrix}$$

$$\{q\}=\begin{bmatrix}u_i & v_i & w_i & \theta_{yi} & \theta_{zi} & u_j & v_j & w_j & \theta_{yj} & \theta_{zj}\end{bmatrix}^T$$

Shape functions are defined as:

$$N_{t1}=\frac{1}{1+\Phi}\left[2s^3-3s^2-\Phi s+(1+\Phi)\right];\qquad N_{\theta 1}=\frac{6}{(1+\Phi)L}\left(s^2-s\right)$$

$$N_{t2}=\frac{L}{1+\Phi}\left[s^3-\left(2+\frac{\Phi}{2}\right)s^2+\left(1+\frac{\Phi}{2}\right)s\right];\qquad N_{\theta 2}=\frac{1}{1+\Phi}\left[3s^2-(4+\Phi)s+(1+\Phi)\right]$$

$$N_{t3}=-\frac{1}{1+\Phi}\left[2s^3-3s^2-\Phi s\right];\qquad N_{\theta 3}=-\frac{6}{(1+\Phi)L}\left(s^2-s\right)$$

$$N_{t4}=\frac{L}{1+\Phi}\left[s^3-\left(1-\frac{\Phi}{2}\right)s^2-\frac{\Phi}{2}s\right];\qquad N_{\theta 4}=\frac{1}{1+\Phi}\left[3s^2-(2-\Phi)s\right]$$

where $\Phi=\dfrac{12EI}{k_s AGL^2}$, $s=\dfrac{x}{L}$

A.3 Finite Element Equations

Set weighted functions as

$$\begin{Bmatrix}W_1\\ W_2\\ W_3\\ W_4\\ W_5\end{Bmatrix}=\begin{Bmatrix}[N_u]^T\\ [N_v]^T\\ [N_w]^T\\ [N_{\theta y}]^T\\ [N_{\theta z}]^T\end{Bmatrix} \tag{A.6}$$

From equations (A.5) and (A.6), the following equations can be obtained:

$$\begin{bmatrix}\frac{\partial u}{\partial x} & \frac{\partial v}{\partial x} & \frac{\partial w}{\partial x} & \frac{\partial \theta_y}{\partial x} & \frac{\partial \theta_z}{\partial x}\end{bmatrix}^T=\left[\frac{\partial N}{\partial x}\right]\{q\}=[N']\{q\}$$

$$\begin{bmatrix}\frac{du}{dt} & \frac{dv}{dt} & \frac{dw}{dt} & \frac{d\theta_y}{dt} & \frac{d\theta_z}{dt}\end{bmatrix}^T=[N]\{\dot{q}\}$$

$$\left[\frac{d^2u}{dt^2}\quad\frac{d^2v}{dt^2}\quad\frac{d^2w}{dt^2}\quad\frac{d^2\theta_y}{dt^2}\quad\frac{d^2\theta_z}{dt^2}\right]^T=[N]\{\ddot{q}\}$$

$$\left[\frac{\partial W_1}{\partial x}\quad\frac{\partial W_2}{\partial x}\quad\frac{\partial W_3}{\partial x}\quad\frac{\partial W_4}{\partial x}\quad\frac{\partial W_5}{\partial x}\right]^T=\left[\left[\frac{\partial N_u}{\partial x}\right]^T\quad\left[\frac{\partial N_v}{\partial x}\right]^T\quad\left[\frac{\partial N_w}{\partial x}\right]^T\quad\left[\frac{\partial N_{\theta y}}{\partial x}\right]^T\quad\left[\frac{\partial N_{\theta z}}{\partial x}\right]^T\right]^T$$

$$=\left[\left[N_u'\right]^T\quad\left[N_v'\right]^T\quad\left[N_w'\right]^T\quad\left[N_{\theta y}'\right]^T\quad\left[N_{\theta z}'\right]^T\right]^T$$

Substitute the above equations into equations (A.3), and the discrete finite element equations are as follows:

$$[M]\{\ddot{q}\}-\Omega[G]\{\dot{q}\}+\left([K]+[K]_A-\Omega^2[M]_C\right)\{q\}=\{F\} \tag{A.7}$$

where $[M]$ is mass matrix, $[G]$ is gyroscopic matrix, $[K]$ is stiffness matrix, $[K]_A$ is stiffness matrix due to axial force, and $\{F\}$ is force including distributed and concentrated forces. These values can be found from the following formulae:

$$[M]=[M]_T+[M]_R=\int_0^L[N]^T\begin{bmatrix}\rho A&0&0&0&0\\0&\rho A&0&0&0\\0&0&\rho A&0&0\\0&0&0&\rho I&0\\0&0&0&0&\rho I\end{bmatrix}[N]dz$$

$$[G]=\int_0^L[N]^T\begin{bmatrix}0&0&0&0&0\\0&0&0&0&0\\0&0&0&0&0\\0&0&0&0&-\rho J\\0&0&0&\rho J&0\end{bmatrix}[N]dz$$

$$[K]=\int_0^L\begin{bmatrix}\left[N_u'\right]^T\\\left[N_v'\right]^T-\left[N_{\theta z}\right]^T\\\left[N_w'\right]^T+\left[N_{\theta y}\right]^T\\\left[N_{\theta y}'\right]^T\\\left[N_{\theta z}'\right]^T\end{bmatrix}^T\begin{bmatrix}EA&0&0&0&0\\0&k_sAG&0&0&0\\0&0&k_sAG&0&0\\0&0&0&EI&0\\0&0&0&0&EI\end{bmatrix}\begin{bmatrix}\left[N_u'\right]\\\left[N_v'\right]-\left[N_{\theta z}\right]\\\left[N_w'\right]+\left[N_{\theta y}\right]\\\left[N_{\theta y}'\right]\\\left[N_{\theta z}'\right]\end{bmatrix}dx$$

$$[K]_A = \int_0^L [N']^T \begin{bmatrix} 0 & 0 & 0 & 0 & 0 \\ 0 & P & 0 & 0 & 0 \\ 0 & 0 & P & 0 & 0 \\ 0 & 0 & 0 & 0 & 0 \\ 0 & 0 & 0 & 0 & 0 \end{bmatrix} [N'] dz ; \qquad [M]_C = \int_0^L [N]^T \begin{bmatrix} 0 & 0 & 0 & 0 & 0 \\ 0 & \rho A & 0 & 0 & 0 \\ 0 & 0 & \rho A & 0 & 0 \\ 0 & 0 & 0 & 0 & 0 \\ 0 & 0 & 0 & 0 & 0 \end{bmatrix} [N] dz$$

$$\{F\} = \{F\}_D + \{F\}_C$$

$$\{F\}_D = \int_0^L [N]^T \begin{bmatrix} q_x \\ q_y \\ q_z \\ m_y \\ m_z \end{bmatrix} dz$$

A.4 Finite Element Matrices

$[M^b] = [M]_T + [M]_R$, where $[M]_T$ is the translational mass matrix and $[M]_R$ is the rotational mass matrix.

$$[M]_T = \frac{\rho AL}{420(1+\Phi)^2} \begin{bmatrix} m_{a1} & & & & & & & & & \\ 0 & m_1 & & & & S & & & & \\ 0 & 0 & m_1 & & & & Y & & & \\ 0 & 0 & -m_2 & m_5 & & & & M & & \\ 0 & m_2 & 0 & 0 & m_5 & & & & & \\ m_{a2} & 0 & 0 & 0 & 0 & m_{a1} & & & & \\ 0 & m_3 & 0 & 0 & -m_4 & 0 & m_1 & & & \\ 0 & 0 & m_3 & m_4 & 0 & 0 & 0 & m_1 & & \\ 0 & 0 & -m_4 & m_6 & 0 & 0 & 0 & m_2 & m_5 & \\ 0 & m_4 & 0 & 0 & m_6 & 0 & -m_2 & 0 & 0 & m_5 \end{bmatrix}$$

$$[M]_R = \frac{\rho I}{30(1+\Phi)^2 L}\begin{bmatrix} 0 & & & & & & & & & \\ 0 & 36 & & & & S & & & & \\ 0 & 0 & 36 & & & & Y & & & \\ 0 & 0 & -m_7 & m_8 & & & & M & & \\ 0 & m_7 & 0 & 0 & m_8 & & & & & \\ 0 & 0 & 0 & 0 & 0 & 0 & & & & \\ 0 & -36 & 0 & 0 & -m_7 & 0 & 36 & & & \\ 0 & 0 & -36 & m_7 & 0 & 0 & 0 & 36 & & \\ 0 & 0 & -m_7 & m_9 & 0 & 0 & 0 & m_7 & m_8 & \\ 0 & m_7 & 0 & 0 & m_9 & 0 & -m_7 & 0 & 0 & m_8 \end{bmatrix}$$

$m_1 = 156 + 294\Phi + 140\Phi^2$; $m_2 = (22 + 38.5\Phi + 17.5\Phi^2)L$; $m_3 = 54 + 126\Phi + 70\Phi^2$;

$m_4 = -(13 + 31.5\Phi + 17.5\Phi^2)L$; $m_5 = (4 + 7\Phi + 3.5\Phi^2)L^2$; $m_6 = -(3 + 7\Phi + 3.5\Phi^2)L^2$;

$m_{a1} = 140(1+\Phi)^2$; $m_{a2} = 70(1+\Phi)^2$; $\Phi = \dfrac{12EI}{k_s AGL^2}$

$m_7 = (3 - 15\Phi)L$; $m_8 = (4 + 5\Phi + 10\Phi^2)L^2$; $m_9 = (-1 - 5\Phi + 5\Phi^2)L^2$

The mass matrix $[M^b]_C$ used for computing the centrifugal force is

$$[M]_C = \frac{\rho AL}{420(1+\Phi)^2}\begin{bmatrix} 0 & & & & & & & & & \\ 0 & m_1 & & & & S & & & & \\ 0 & 0 & m_1 & & & & Y & & & \\ 0 & 0 & -m_2 & m_5 & & & & M & & \\ 0 & m_2 & 0 & 0 & m_5 & & & & & \\ 0 & 0 & 0 & 0 & 0 & 0 & & & & \\ 0 & m_3 & 0 & 0 & -m_4 & 0 & m_1 & & & \\ 0 & 0 & m_3 & m_4 & 0 & 0 & 0 & m_1 & & \\ 0 & 0 & -m_4 & m_6 & 0 & 0 & 0 & m_2 & m_5 & \\ 0 & m_4 & 0 & 0 & m_6 & 0 & -m_2 & 0 & 0 & m_5 \end{bmatrix}$$

The gyroscopic matrix $[G^b]$ is

$$[G^b]=\frac{\rho J}{30(1+\Phi)^2 L}\begin{bmatrix}
0 & & & & & & & & & \\
0 & 0 & & & & SKEW & & & & \\
0 & 36 & 0 & & & & S & & & \\
0 & -m_7 & 0 & 0 & & & & Y & & \\
0 & 0 & -m_7 & m_8 & 0 & & & & M & \\
0 & 0 & 0 & 0 & 0 & 0 & & & & \\
0 & 0 & 36 & -m_7 & 0 & 0 & 0 & & & \\
0 & -36 & 0 & 0 & -m_7 & 0 & 36 & 0 & & \\
0 & -m_7 & 0 & 0 & -m_9 & 0 & m_7 & 0 & 0 & \\
0 & 0 & -m_7 & m_9 & 0 & 0 & 0 & m_7 & m_8 & 0
\end{bmatrix}$$

The stiffness matrix $[K^b]$ is

$$[K^b]=\frac{EI}{(1+\Phi)L^3}\begin{bmatrix}
k_1 & & & & & & & & & \\
0 & 12 & & & & S & & & & \\
0 & 0 & 12 & & & & Y & & & \\
0 & 0 & -6L & k_2 & & & & M & & \\
0 & 6L & 0 & 0 & k_2 & & & & & \\
-k_1 & 0 & 0 & 0 & 0 & k_1 & & & & \\
0 & -12 & 0 & 0 & -6L & 0 & 12 & & & \\
0 & 0 & -12 & 6L & 0 & 0 & 0 & 12 & & \\
0 & 0 & -6L & k_3 & 0 & 0 & 0 & 6L & k_2 & \\
0 & 6L & 0 & 0 & k_3 & 0 & -6L & 0 & 0 & k_2
\end{bmatrix}$$

$k_1 = A(1+\Phi)L^2/I$; $k_2 = (4+\Phi)L^2$; $k_3 = (2-\Phi)L^2$

The stiffness matrix $[K^b]_P$ due to axial load is

$$[K^b]_P = \frac{P_a}{30(1+\Phi)L}\begin{bmatrix} 0 & & & & & & & & & \\ 0 & k_4 & & & & S & & & & \\ 0 & 0 & k_4 & & & & Y & & & \\ 0 & 0 & -3L & k_5 & & & & M & & \\ 0 & 3L & 0 & 0 & k_5 & & & & & \\ 0 & 0 & 0 & 0 & 0 & 0 & & & & \\ 0 & -k_4 & 0 & 0 & -3L & 0 & k_4 & & & \\ 0 & 0 & -k_4 & 3L & 0 & 0 & 0 & k_4 & & \\ 0 & 0 & -3L & k_6 & 0 & 0 & 0 & 3L & k_5 & \\ 0 & 3L & 0 & 0 & k_6 & 0 & -3L & 0 & 0 & k_5 \end{bmatrix}$$

$$k_4 = 36 + 60\Phi + 30\Phi^2;\ k_5 = \left(4 + 5\Phi + 2.5\Phi^2\right)L^2;\ k_6 = -\left(1 + 5\Phi + 2.5\Phi^2\right)L^2$$

The total load $\{F^b\}$ on the beam consists of the distributed forces on each element $\{F^b\}_D$

$$\{F^b\}_D = \begin{Bmatrix} \frac{1}{2}q_x L \\ \frac{1}{2}q_y L - \frac{m_z}{1+\Phi} \\ \frac{1}{2}q_z L + \frac{m_y}{1+\Phi} \\ -\frac{1}{12}q_z L^2 + \frac{\Phi m_y L}{2(1+\Phi)} \\ \frac{1}{12}q_y L^2 + \frac{\Phi m_z L}{2(1+\Phi)} \\ \frac{1}{2}q_x L \\ \frac{1}{2}q_y L + \frac{m_z}{1+\Phi} \\ \frac{1}{2}q_z L - \frac{m_y}{1+\Phi} \\ \frac{1}{12}q_z L^2 + \frac{\Phi m_y L}{2(1+\Phi)} \\ -\frac{1}{12}q_y L^2 + \frac{\Phi m_z L}{2(1+\Phi)} \end{Bmatrix}$$

and the concentrated load at each end of the element $\{F^b\}_C$:

$$\{F^b\}_C = \begin{bmatrix} F_{xi} & F_{yi} & F_{zi} & M_{xi} & M_{yi} & F_{xj} & F_{yj} & F_{zj} & M_{xj} & M_{yj} \end{bmatrix}^T$$

Appendix B

Coefficients for Equations (3.38)

The derivatives of errors with respect to variables $U_k, V_k, \delta_{ok}, \delta_{ik}$ are obtained from Eq.(3.38):

$$a_{11} = \frac{\partial \varepsilon_1}{\partial U_k} = -2(U_{ik} - U_k),\ a_{12} = \frac{\partial \varepsilon_1}{\partial V_k} = -2(V_{ik} - V_k),\ a_{13} = \frac{\partial \varepsilon_1}{\partial \delta_{ok}} = 0,\ a_{14} = \frac{\partial \varepsilon_1}{\partial \delta_{ik}} = -2\Delta_{ik}$$

$$a_{21} = \frac{\partial \varepsilon_2}{\partial U_k} = 2U_k,\ a_{22} = \frac{\partial \varepsilon_2}{\partial V_k} = 2V_k,\ a_{23} = \frac{\partial \varepsilon_2}{\partial \delta_{ok}} = -2\Delta_{ok},\ a_{24} = \frac{\partial \varepsilon_2}{\partial \delta_{ik}} = 0$$

$$a_{31} = \frac{\partial \varepsilon_3}{\partial U_k} = -\frac{M_{gk}}{D}\left(\frac{1}{\Delta_{ok}} + \frac{1}{\Delta_{ik}}\right),\ a_{32} = \frac{\partial \varepsilon_3}{\partial V_k} = \frac{Q_{ok}}{\Delta_{ok}} + \frac{Q_{ik}}{\Delta_{ik}},$$

$$a_{33} = \frac{\partial \varepsilon_3}{\partial \delta_{ok}} = \frac{3}{2} K_o \delta_{ok}^{1/2} \cos\theta_{ok} - Q_{ok} \frac{V_k}{\Delta_{ok}^2} + \frac{M_{gk}}{D} \frac{U_k}{\Delta_{ok}^2}$$

$$a_{34} = \frac{\partial \varepsilon_3}{\partial \delta_{ik}} = -\left(\frac{3}{2} K_i \delta_{ik}^{1/2} \cos\theta_{ik} - Q_{ik} \frac{V_{ik} - V_k}{\Delta_{ik}^2} + \frac{M_{gk}}{D} \frac{U_{ik} - U_k}{\Delta_{ik}^2}\right)$$

$$a_{41} = \frac{\partial \varepsilon_4}{\partial U_k} = \frac{Q_{ok}}{\Delta_{ok}} + \frac{Q_{ik}}{\Delta_{ik}},\ a_{42} = \frac{\partial \varepsilon_4}{\partial V_k} = \frac{M_{gk}}{D}\left(\frac{1}{\Delta_{ok}} + \frac{1}{\Delta_{ik}}\right),$$

$$a_{43} = \frac{\partial \varepsilon_4}{\partial \delta_{ok}} = \frac{3}{2} K_o \delta_{ok}^{1/2} \sin\theta_{ok} - Q_{ok} \frac{U_k}{\Delta_{ok}^2} - \frac{M_{gk}}{D} \frac{V_k}{\Delta_{ok}^2}$$

$$a_{44} = \frac{\partial \varepsilon_4}{\partial \delta_{ik}} = -\left(\frac{3}{2} K_i \delta_{ik}^{1/2} \sin\theta_{ik} - Q_{ik} \frac{U_{ik} - U_k}{\Delta_{ik}^2} - \frac{M_{gk}}{D} \frac{V_{ik} - V_k}{\Delta_{ik}^2}\right)$$

Appendix C

Stiffness Matrix of Bearings

The derivatives of forces about the displacements are obtained from Eq.(39):

For brevity, let $\delta^{i} = \left(\delta_x^i, \delta_y^i, \delta_z^i, \gamma_y^i, \gamma_z^i\right)$

$$\frac{\partial F_{xi}}{\partial \delta^i} = \sum_{k=1}^{N}\left(\frac{\partial Q_{ik}}{\partial \delta^i}\sin\theta_{ik} + Q_{ik}\frac{\partial(\sin\theta_{ik})}{\partial \delta^i} + \frac{\cos\theta_{ik}}{D}\frac{\partial M_{gk}}{\partial \delta^i} + \frac{M_{gk}}{D}\frac{\partial(\cos\theta_{ik})}{\partial \delta^i}\right)$$

$$\frac{\partial F_{yi}}{\partial \delta^i} = \sum_{k=1}^{N}\left(\frac{\partial Q_{ik}}{\partial \delta^i}\cos\theta_{ik} + Q_{ik}\frac{\partial(\cos\theta_{ik})}{\partial \delta^i} - \frac{\sin\theta_{ik}}{D}\frac{\partial M_{gk}}{\partial \delta^i} - \frac{M_{gk}}{D}\frac{\partial(\sin\theta_{ik})}{\partial \delta^i}\right)\cos\varphi_k$$

$$\frac{\partial F_{zi}}{\partial \delta^i} = \sum_{k=1}^{N}\left(\frac{\partial Q_{ik}}{\partial \delta^i}\cos\theta_{ik} + Q_{ik}\frac{\partial(\cos\theta_{ik})}{\partial \delta^i} - \frac{\sin\theta_{ik}}{D}\frac{\partial M_{gk}}{\partial \delta^i} - \frac{M_{gk}}{D}\frac{\partial(\sin\theta_{ik})}{\partial \delta^i}\right)\sin\varphi_k$$

$$\frac{\partial M_{yi}}{\partial \delta^i} = \sum_{k=1}^{N}\left[r_{ic}\left(\frac{\partial Q_{ik}}{\partial \delta^i}\sin\theta_{ik} + Q_{ik}\frac{\partial(\sin\theta_{ik})}{\partial \delta^i} + \frac{\cos\theta_{ik}}{D}\frac{\partial M_{gk}}{\partial \delta^i} + \frac{M_{gk}}{D}\frac{\partial(\cos\theta_{ik})}{\partial \delta^i}\right) - f_i\frac{\partial M_{gk}}{\partial \delta^i}\right]\sin\varphi_k$$

$$\frac{\partial M_{zi}}{\partial \delta^i} = -\sum_{k=1}^{N}\left[r_{ic}\left(\frac{\partial Q_{ik}}{\partial \delta^i}\sin\theta_{ik} + Q_{ik}\frac{\partial(\sin\theta_{ik})}{\partial \delta^i} + \frac{\cos\theta_{ik}}{D}\frac{\partial M_{gk}}{\partial \delta^i} + \frac{M_{gk}}{D}\frac{\partial(\cos\theta_{ik})}{\partial \delta^i}\right) - f_i\frac{\partial M_{gk}}{\partial \delta^i}\right]\cos\varphi_k$$

where

$$\frac{\partial Q_{ik}}{\partial \delta^i} = \frac{3}{2}K_i\delta_{ik}^{1/2}\frac{\partial \delta_{ik}}{\partial \delta^i},\quad \frac{\partial(\sin\theta_{ik})}{\partial \delta^i} = \frac{\left(\frac{\partial U_{ik}}{\partial \delta^i} - \frac{\partial U_k}{\partial \delta^i}\right)\Delta_{ik} - (U_{ik} - U_k)\frac{\partial \delta_{ik}}{\partial \delta^i}}{\Delta_{ik}^2}$$

$$\frac{\partial(\cos\theta_{ik})}{\partial \delta^i} = \frac{\left(\frac{\partial V_{ik}}{\partial \delta^i} - \frac{\partial V_k}{\partial \delta^i}\right)\Delta_{ik} - (V_{ik} - V_k)\frac{\partial \delta_{ik}}{\partial \delta^i}}{\Delta_{ik}^2}$$

$$\frac{\partial U_{ik}}{\partial \delta_x^i} = 1,\ \frac{\partial U_{ik}}{\partial \delta_y^i} = 0,\ \frac{\partial U_{ik}}{\partial \delta_z^i} = 0,\ \frac{\partial U_{ik}}{\partial \gamma_y^i} = r_{ic}\sin\varphi_k,\ \frac{\partial U_{ik}}{\partial \gamma_z^i} = -r_{ic}\cos\varphi_k$$

$$\frac{\partial V_{ik}}{\partial \delta_x^i} = 0,\ \frac{\partial V_{ik}}{\partial \delta_y^i} = \cos\varphi_k,\ \frac{\partial V_{ik}}{\partial \delta_z^i} = \sin\varphi_k,\ \frac{\partial V_{ik}}{\partial \gamma_y^i} = 0,\ \frac{\partial V_{ik}}{\partial \gamma_z^i} = 0$$

By differentiating Eq.(35) and (36) with respect to δ^i, we obtain

$$\begin{Bmatrix} \frac{\partial U_k}{\partial \delta^i} \\ \frac{\partial V_k}{\partial \delta^i} \\ \frac{\partial \delta_{ok}}{\partial \delta^i} \\ \frac{\partial \delta_{ik}}{\partial \delta^i} \end{Bmatrix} = [b_{ij}]^{-1} \begin{Bmatrix} (U_{ik}-U_k)\frac{\partial U_{ik}}{\partial \delta^i} + (V_{ik}-V_k)\frac{\partial V_{ik}}{\partial \delta^i} \\ 0 \\ \frac{Q_{ik}}{\Delta_{ik}}\frac{\partial V_{ik}}{\partial \delta^i} - \frac{M_{gk}}{D}\frac{1}{\Delta_{ik}}\frac{\partial U_{ik}}{\partial \delta^i} \\ \frac{Q_{ik}}{\Delta_{ik}}\frac{\partial U_{ik}}{\partial \delta^i} + \frac{M_{gk}}{D}\frac{1}{\Delta_{ik}}\frac{\partial V_{ik}}{\partial \delta^i} \end{Bmatrix}$$

where $b_{11} = U_{ik} - U_k$; $b_{12} = V_{ik} - V_k$; $b_{13} = 0$; $b_{14} = \Delta_{ik}$; $b_{21} = U_k$; $b_{22} = V_k$; $b_{23} = -\Delta_{ok}$; $b_{24} = 0$; $b_{ij} = a_{ij}$ $(i = 3,4; j = 1,2,3,4)$ (a_{ij} are from appendix B)

$$\frac{\partial M_{gk}}{\partial \delta} = J\Omega^2 \left[\frac{\partial \left(\frac{\Omega_B}{\Omega}\right)_k}{\partial \delta} \left(\frac{\Omega_E}{\Omega}\right)_k \tan\alpha_k + \left(\frac{\Omega_B}{\Omega}\right)_k \frac{\partial \left(\frac{\Omega_E}{\Omega}\right)_k}{\partial \delta} \tan\alpha_k + \left(\frac{\Omega_B}{\Omega}\right)_k \left(\frac{\Omega_E}{\Omega}\right)_k \frac{\partial(\tan\alpha_k)}{\partial \delta} \right]$$

$$\left(\frac{\Omega_B}{\Omega}\right)_k = \frac{-1}{\lambda\left(\frac{\cos\theta_{ok} + \tan\alpha_k \sin\theta_{ok}}{1+\lambda\cos\theta_{ok}} + \frac{\cos\theta_{ik} + \tan\alpha_k \sin\theta_{ik}}{1-\lambda\cos\theta_{ik}}\right)} = -\frac{1}{\lambda}\frac{1}{A+B}$$

$$A = \frac{\cos\theta_{ok} + \tan\alpha_k \sin\theta_{ok}}{1+\lambda\cos\theta_{ok}}, \quad B = \frac{\cos\theta_{ik} + \tan\alpha_k \sin\theta_{ik}}{1-\lambda\cos\theta_{ik}}$$

$$\frac{\partial \left(\frac{\Omega_B}{\Omega}\right)_k}{\partial \delta} = \frac{1}{\lambda}\frac{\frac{\partial A}{\partial \delta} + \frac{\partial B}{\partial \delta}}{(A+B)^2}$$

$$\frac{\partial A}{\partial \delta} = \frac{\left[\frac{\partial(\tan\alpha_k)}{\partial \delta}\sin\theta_{ok} + \tan\alpha_k \frac{\partial(\sin\theta_{ok})}{\partial \delta}\right](1+\lambda\cos\theta_{ok}) + (1-\lambda\tan\alpha_k \sin\theta_{ok})\frac{\partial(\cos\theta_{ok})}{\partial \delta}}{(1+\lambda\cos\theta_{ok})^2}$$

$$\frac{\partial B}{\partial \delta} = \frac{\left[\frac{\partial(\tan\alpha_k)}{\partial \delta}\sin\theta_{ik} + \tan\alpha_k \frac{\partial(\sin\theta_{ik})}{\partial \delta}\right](1-\lambda\cos\theta_{ik}) + (1+\lambda\tan\alpha_k \sin\theta_{ik})\frac{\partial(\cos\theta_{ik})}{\partial \delta}}{(1-\lambda\cos\theta_{ik})^2}$$

For inner ring control,

$$\frac{\partial(\tan\alpha_k)}{\partial\delta}=\frac{\frac{\partial(\sin\theta_{ik})}{\partial\delta}(\cos\theta_{ik}-\lambda)-\sin\theta_{ik}\frac{\partial(\cos\theta_{ik})}{\partial\delta}}{(\cos\theta_{ik}-\lambda)^2}$$

$$\frac{\partial\left(\frac{\Omega_E}{\Omega}\right)_k}{\partial\delta}=\frac{(1+\lambda\cos\theta_{ok})\frac{\partial[\cos(\theta_{ik}-\theta_{ok})]}{\partial\delta}-\lambda\frac{\partial(\cos\theta_{ok})}{\partial\delta}[1+\cos(\theta_{ik}-\theta_{ok})]}{[1+\cos(\theta_{ik}-\theta_{ok})]^2}$$

For outer ring control,

$$\frac{\partial(\tan\alpha_k)}{\partial\delta}=\frac{\frac{\partial(\sin\theta_{ok})}{\partial\delta}(\cos\theta_{ok}+\lambda)-\sin\theta_{ok}\frac{\partial(\cos\theta_{ok})}{\partial\delta}}{(\cos\theta_{ok}+\lambda)^2}$$

$$\frac{\partial\left(\frac{\Omega_E}{\Omega}\right)_k}{\partial\delta}=-\frac{(1-\lambda\cos\theta_{ik})\frac{\partial[\cos(\theta_{ik}-\theta_{ok})]}{\partial\delta}+\lambda\frac{\partial(\cos\theta_{ik})}{\partial\delta}[1+\cos(\theta_{ik}-\theta_{ok})]}{[1+\cos(\theta_{ik}-\theta_{ok})]^2}$$

$$\frac{\partial[\cos(\theta_{ik}-\theta_{ok})]}{\partial\delta}=\frac{\partial(\cos\theta_{ik})}{\partial\delta}\cos\theta_{ok}+\cos\theta_{ik}\frac{\partial(\cos\theta_{ok})}{\partial\delta}+\frac{\partial(\sin\theta_{ik})}{\partial\delta}\sin\theta_{ok}+\sin\theta_{ik}\frac{\partial(\sin\theta_{ok})}{\partial\delta}$$

In matrix form,

$$\left[K_{II}^T\right]=\left[K_I^T\right]=\begin{bmatrix}\frac{\partial F_{xi}}{\partial\delta_x^i} & \frac{\partial F_{xi}}{\partial\delta_y^i} & \frac{\partial F_{xi}}{\partial\delta_z^i} & \frac{\partial F_{xi}}{\partial\gamma_y^i} & \frac{\partial F_{xi}}{\partial\gamma_z^i}\\ \frac{\partial F_{yi}}{\partial\delta_x^i} & \frac{\partial F_{yi}}{\partial\delta_y^i} & \frac{\partial F_{yi}}{\partial\delta_z^i} & \frac{\partial F_{yi}}{\partial\gamma_y^i} & \frac{\partial F_{yi}}{\partial\gamma_z^i}\\ \frac{\partial F_{zi}}{\partial\delta_x^i} & \frac{\partial F_{zi}}{\partial\delta_y^i} & \frac{\partial F_{zi}}{\partial\delta_z^i} & \frac{\partial F_{zi}}{\partial\gamma_y^i} & \frac{\partial F_{zi}}{\partial\gamma_z^i}\\ \frac{\partial M_{yi}}{\partial\delta_x^i} & \frac{\partial M_{yi}}{\partial\delta_y^i} & \frac{\partial M_{yi}}{\partial\delta_z^i} & \frac{\partial M_{yi}}{\partial\gamma_y^i} & \frac{\partial M_{yi}}{\partial\gamma_z^i}\\ \frac{\partial M_{zi}}{\partial\delta_x^i} & \frac{\partial M_{zi}}{\partial\delta_y^i} & \frac{\partial M_{zi}}{\partial\delta_z^i} & \frac{\partial M_{zi}}{\partial\gamma_y^i} & \frac{\partial M_{zi}}{\partial\gamma_z^i}\end{bmatrix}=\begin{bmatrix}k_{11} & & S & & \\ k_{21} & k_{22} & & Y & \\ k_{31} & k_{32} & k_{33} & & M\\ k_{41} & k_{42} & k_{43} & k_{44} & \\ k_{51} & k_{52} & k_{53} & k_{54} & k_{55}\end{bmatrix}$$

Similarly, the following matrixes can be obtained from Eq.(39) and Eq.(40):

$$\left[K_{OO}^{T}\right]=\begin{bmatrix} \frac{\partial F_{xo}}{\partial \delta_x^o} & \frac{\partial F_{xo}}{\partial \delta_y^o} & \frac{\partial F_{xo}}{\partial \delta_z^o} & \frac{\partial F_{xo}}{\partial \gamma_y^o} & \frac{\partial F_{xo}}{\partial \gamma_z^o} \\ \frac{\partial F_{yo}}{\partial \delta_x^o} & \frac{\partial F_{yo}}{\partial \delta_y^o} & \frac{\partial F_{yo}}{\partial \delta_z^o} & \frac{\partial F_{yo}}{\partial \gamma_y^o} & \frac{\partial F_{yo}}{\partial \gamma_z^o} \\ \frac{\partial F_{zo}}{\partial \delta_x^o} & \frac{\partial F_{zo}}{\partial \delta_y^o} & \frac{\partial F_{zo}}{\partial \delta_z^o} & \frac{\partial F_{zo}}{\partial \gamma_y^o} & \frac{\partial F_{zo}}{\partial \gamma_z^o} \\ \frac{\partial M_{yo}}{\partial \delta_x^o} & \frac{\partial M_{yo}}{\partial \delta_y^o} & \frac{\partial M_{yo}}{\partial \delta_z^o} & \frac{\partial M_{yo}}{\partial \gamma_y^o} & \frac{\partial M_{yo}}{\partial \gamma_z^o} \\ \frac{\partial M_{zo}}{\partial \delta_x^o} & \frac{\partial M_{zo}}{\partial \delta_y^o} & \frac{\partial M_{zo}}{\partial \delta_z^o} & \frac{\partial M_{zo}}{\partial \gamma_y^o} & \frac{\partial M_{zo}}{\partial \gamma_z^o} \end{bmatrix}=\left[K_{\mathrm{O}}^{T}\right];$$

$$\left[K_{IO}^{T}\right]=\begin{bmatrix} \frac{\partial F_{xi}}{\partial \delta_x^o} & \frac{\partial F_{xi}}{\partial \delta_y^o} & \frac{\partial F_{xi}}{\partial \delta_z^o} & \frac{\partial F_{xi}}{\partial \gamma_y^o} & \frac{\partial F_{xi}}{\partial \gamma_z^o} \\ \frac{\partial F_{yi}}{\partial \delta_x^o} & \frac{\partial F_{yi}}{\partial \delta_y^o} & \frac{\partial F_{yi}}{\partial \delta_z^o} & \frac{\partial F_{yi}}{\partial \gamma_y^o} & \frac{\partial F_{yi}}{\partial \gamma_z^o} \\ \frac{\partial F_{zi}}{\partial \delta_x^o} & \frac{\partial F_{zi}}{\partial \delta_y^o} & \frac{\partial F_{zi}}{\partial \delta_z^o} & \frac{\partial F_{zi}}{\partial \gamma_y^o} & \frac{\partial F_{zi}}{\partial \gamma_z^o} \\ \frac{\partial M_{yi}}{\partial \delta_x^o} & \frac{\partial M_{yi}}{\partial \delta_y^o} & \frac{\partial M_{yi}}{\partial \delta_z^o} & \frac{\partial M_{yi}}{\partial \gamma_y^o} & \frac{\partial M_{yi}}{\partial \gamma_z^o} \\ \frac{\partial M_{zi}}{\partial \delta_x^o} & \frac{\partial M_{zi}}{\partial \delta_y^o} & \frac{\partial M_{zi}}{\partial \delta_z^o} & \frac{\partial M_{zi}}{\partial \gamma_y^o} & \frac{\partial M_{zi}}{\partial \gamma_z^o} \end{bmatrix}=-\left[K_{I}^{T}\right]$$

$$\left[K_{OI}^{T}\right]=\begin{bmatrix} \frac{\partial F_{xo}}{\partial \delta_x^i} & \frac{\partial F_{xo}}{\partial \delta_y^i} & \frac{\partial F_{xo}}{\partial \delta_z^i} & \frac{\partial F_{xo}}{\partial \gamma_y^i} & \frac{\partial F_{xo}}{\partial \gamma_z^i} \\ \frac{\partial F_{yo}}{\partial \delta_x^i} & \frac{\partial F_{yo}}{\partial \delta_y^i} & \frac{\partial F_{yo}}{\partial \delta_z^i} & \frac{\partial F_{yo}}{\partial \gamma_y^i} & \frac{\partial F_{yo}}{\partial \gamma_z^i} \\ \frac{\partial F_{zo}}{\partial \delta_x^i} & \frac{\partial F_{zo}}{\partial \delta_y^i} & \frac{\partial F_{zo}}{\partial \delta_z^i} & \frac{\partial F_{zo}}{\partial \gamma_y^i} & \frac{\partial F_{zo}}{\partial \gamma_z^i} \\ \frac{\partial M_{yo}}{\partial \delta_x^i} & \frac{\partial M_{yo}}{\partial \delta_y^i} & \frac{\partial M_{yo}}{\partial \delta_z^i} & \frac{\partial M_{yo}}{\partial \gamma_y^i} & \frac{\partial M_{yo}}{\partial \gamma_z^i} \\ \frac{\partial M_{zo}}{\partial \delta_x^i} & \frac{\partial M_{zo}}{\partial \delta_y^i} & \frac{\partial M_{zo}}{\partial \delta_z^i} & \frac{\partial M_{zo}}{\partial \gamma_y^i} & \frac{\partial M_{zo}}{\partial \gamma_z^i} \end{bmatrix}=-\left[K_{O}^{T}\right]$$

Finally, the tangential stiffness matrix of the bearing can be obtained as follows:

$$\left[K_{B}^{T}\right]=\begin{bmatrix} K_{II}^{T} & K_{IO}^{T} \\ K_{IO}^{T} & K_{OO}^{T} \end{bmatrix}=\begin{bmatrix} K_{I}^{T} & -K_{I}^{T} \\ -K_{O}^{T} & K_{O}^{T} \end{bmatrix}$$